Investigation of Incremental Sheet Forming (ISF) using Advanced Numerical and Analytical Approaches

by

Jaekwang Shin

A dissertation submitted in partial fulfillment
of the requirements for the degree of
Doctor of Philosophy
(Mechanical Engineering)
at the University of Michigan
2021

Doctoral Committee:

        Professor Mihaela Banu, Co-Chair
        Professor Alan Taub, Co-Chair
        Professor Jian Cao, Northwestern University
        Professor S. Jack Hu
        Professor Michael Thouless

Jaekwang Shin

jkshin@umich.edu

ORCID iD: 0000-0002-1964-3730

Acknowledgments

I would like to express my sincere thanks to my advisors, Professor Mihaela Banu and Professor Alan I. Taub. Professor Banu provided me with the opportunity to pursue a career in the Ph.D. program in the field of manufacturing when I was fresh in my first year as a Master's student in Mechanical Engineering, for which I am eternally grateful. She is a great advisor who motivated me to develop my abilities and conduct research in an interdisciplinary manner, grow my ability to tackle challenges and develop solutions. Not only was she an excellent mentor in engineering but also a great teacher in life. Her advice has been precious in making critical decisions in my life, both academically and personally.

I am also grateful to Prof. Alan I. Taub. He has been very supportive of the research and provided great insights and advice that helped me make breakthroughs in my research. I found his advice and discussion extremely valuable, and I appreciate that he always made himself available when I needed his advice despite his busy schedule. He brought a unique perspective to the table, providing insight from the academic and industry sides, which helped me broaden my perspective. I am grateful for his effort providing me with excellent opportunities to develop myself both in academia and in life. Without him, I would not have been successful in the Ph.D. program.

I would like to express my appreciation to my committee members, Professor Jack S. Hu, Professor Michael Thouless, and Professor Jian Cao, for spending their valuable time to provide me with their expert opinion and precious feedback on my dissertation. This research was funded

I would like to extend my gratitude to all of the incremental forming team, Ankush Bansal, Randy Cheng, Maya Nath, Erika Salem, and Kevin Wilt. As fellow students in the Ph.D. program, Ankush, Randy, and Maya were partners in the adventure to understand the incremental forming process. They were always the first to provide meaningful feedback on any results and ideas that I came up with. Their work complemented my research in various ways, and I have enjoyed being in their presence. Erika and Kevin were the students who started the incremental forming project with me and helped me build the foundation of the understanding and research that I have accomplished.

I would like to acknowledge the Hu Lab members. They created a unique research-friendly environment which helped me advance my thoughts and get valuable feedback. I would especially like to thank Dr. Taehwa Lee, who was always there to listen to me and provide meaningful feedback. He was an excellent colleague and a friend, and without him, I would not have enjoyed the life in Michigan as I have had. I would like to thank Dr. Haseung Chung, Dr. Theodor Freiheit, Dr. Baicun Wang, Dr. Chanbai Tan, Dr.Ying Luo, Lei Sun, Weiling Wen, and Lynn Cook for their support and feedback that I have received during my Ph.D. program.

Finally, I would like to thank my parents, Dr. Hyung Seop Shin and Dr. Jung Hee Lee, for supporting me both financially and emotionally through my Ph.D. program. I am proud to be their son and to have followed in their footsteps and completed the Ph.D. program. I love them so much.

Table of Contents

List of Tables

<h1 style="text-align:center">List of Figures</h1>

ABSTRACT

The incremental sheet forming process (ISF) is a suitable candidate for manufacturing lightweight components while achieving cost-effectiveness for low volume production. The critical difference that incremental forming presents compared to the conventional sheet metal forming process is that it does not require dedicated equipment such as a press and specific dies for each shape of the part. The equipment is replaced by a robust setup on a CNC milling machine or a robot in incremental forming. This setup includes a finger-type tool mounted on the head of the CNC or the robot and a clamping system to hold the initial blank. The process is called single point incremental forming (SPIF). For parts with complex geometries, it uses two point incremental forming (TPIF), where the setup includes a back die to support forming the three-dimensional shape. Despite their robustness and low-cost manufacturing, ISF processes are facing challenges in their large-scale adoption because of a lack of understanding of the material-tool interaction and, consequently, lack of possibilities to optimize the process for zero errors. In ISF, the tool-material interaction has a nonlinear relationship dependent on a series of process parameters and local contact conditions, enabling enhanced formability compared with conventional processes. There are currently limited analytical models and finite element models that allow extraction of the relationships between process parameters and material response and prediction of the formed geometry and the defects. However, limited experimental results for complex geometries are an obstacle in the validation of these models. Thus, ISF is still using trial and errors to find the right process parameters to form parts within the given design tolerance. Hence, any attempts to eliminate the trial and error associated with the forming process contribute

significantly to the cost reduction related to manufacturing the part by reducing the amount of material, tooling, and workforce required in the process.

Advancement of numerical modeling, such as multiscale modeling approaches, is a current solution for understanding the forming mechanism of ISF and gives answers to the material defects found during the forming process. Understanding how the instabilities are formed makes it possible to predict what combination of process parameters leads to such conditions and minimize their occurrence. Once the mechanism of incrementally forming is understood is possible to build reduced-order models capable of accurately predicting the geometry and thickness with significantly less computational cost comparing with finite element models.

In this dissertation, three research topics are addressed:

(1) *Understanding the forming mechanism in SPIF/TPIF by using a multi-scale finite element model of incremental forming*: macroscale at the level of part dimensions (millimeter to meter) and microscale at the level of thickness dimension (microns to millimeter). Macroscale model provides global geometry of the part, and microscale model represents a representative volume of this part where intimate interaction between tool and material is studied with the scope of finding the origin of thinning and bulging - two defects which are challenging the advancement of ISF in large production and not yet understood. The hypothesis is that this thinning is produced by material movement, and a material defects produces bulging. The multi-scale model is used to demonstrate this hypothesis and provide guidelines for optimizing the process parameters to reduce the two defects.

(2) *Predicting geometry, bulge, and thinning using novel and cost-effective analytical methods*. Two analytical models are developed to predict the geometric distribution for SPIF/TPIF process based on understanding the material movement found in the wall and its

contributions to the bulge formation. The process parameters such as tool radius, tool shape, sheet thickness, wall angle, etc., are taken into account, and the surface profile of the formed surface is predicted. Consequently, based on material conservation, the amount of material movement is calculated, and based on the weighted superpositioning method, the bulge profile of the undeformed region is predicted.

This dissertation provides a new understanding of the mechanism of instabilities found during the incremental forming process. It utilizes them to provide models capable of giving accurate predictions without numerical simulations with expensive computations. A set of recommendations for the range of process parameters is shown to increase the manufacturing process's precision.

Chapter 1 Introduction

1.1. Motivation

Lightweighting of the components has been a critical issue in the automotive and aerospace industry. The weight of the component directly correlates to the fuel efficiency and cost of operation. In many cases, lightweighting has been achieved by substituting the much heavier steel alloys with aluminum alloys which require a lower forming force to manufacture than steel alloys; however, the cost of the material can be more expensive for aluminum alloys. That is why optimizing the forming processes for achieving a reduced cost of the lightweight solution is a target of the automotive industry. To meet this target, almost 90% of the automotive body is manufactured using conventional forming technologies such as stamping and hydroforming process, which are known to be suitable for high volume production. However, in the aerospace industry or automotive prototyping, which is characterized by a low volume production, these processes are not suitable for achieving lower costs of the components. Conventional forming processes such as stamping and hydroforming require dedicated dies and presses, which lead to higher costs if they are not used for high volume production [1]. This effect is due to the proportion of the fixed cost being much larger and the number of parts not large enough to spread the fixed cost.

Incremental forming is an alternative for the conventional forming technologies for being applied to low volume production because (a) it does not require a dedicated die and press, (b) it enables variability in designing complex shapes, and (c) it requires lower forming forces than conventional processes. Based on the published reports, the cost analysis shows that the

1

incremental forming process is the most cost-efficient when applied to less than 1000 parts per year production [2]. While the economic aspect and the capabilities to make the incremental forming are attractive as an alternative agile manufacturing process, incremental forming still presents some challenges for achieving the geometric accuracy obtained in conventional processes [3]. The forming defects that occur during forming lead to geometric deviation from the original part design because of thinning or bulging and sometimes lead to failure. These deviations lead to a loss of precision in manufacturing, which is key to achieving production quality and repeatability. Many researchers have tried to understand incremental forming capabilities and their potential for achieving high precision by considering analytical and finite element models.

In recent years, advancement in numerical modeling has allowed engineers to predict various aspects of the forming process with satisfactory accuracy. These predictions have permitted a more accurate design of a manufacturing process for a target part and lowered the number of iterations required to achieve precision in manufacturing. The finite element models (FEM) of incremental forming processes have played a key role in understanding the material properties and geometry of the formed part by capturing the deformation that occurs during the process [4]. However, there have been challenges for accurate prediction for the models due to non-linear material behavior with non-linear strain path found in ISF [5]. For models to have accurate results, various optimization and calibration of the input parameters have to occur throughout each stage of the modeling process [6]. Calibration of the material model and the numerical parameters can be time-consuming and iterative with a high computational cost.

In this respect, analytical models can be an efficient alternative to FEMs by providing results with less computational cost and calibration. However, the hurdle with analytical models is that it requires understanding the fundamental relationship quantitatively. Thus, this dissertation

focuses on understanding the material behavior and defects occurring during the incremental forming by utilizing newly developed FEMs and the associated experimental validations and, further, deriving qualitative relationships between different classes of parameters such as process, material, numerical and performance parameters. Based on the derived relations between these parameters, an analytical model is proposed to predict formed geometry, including thinning and bulge. The analytical model is validated against experimental tests and measurements.

1.2. Summary of the literature review and the state of the art

A detailed literature review will be presented in Chapter 2. A summary of the literature review is provided here.

Incremental forming is a sheet metal forming process that uses a finger type tool that incrementally forms the metal sheet clamped in a rigid frame. While this definition allows the incremental forming to achieve dieless forming, many variations have been developed to complement the shortcomings of the process, such as errors between the target geometry and the actual geometry of the formed part and springback. Thus, the most common incremental forming schemes are presented as follows.

- Single point incremental forming (SPIF) is a dieless forming scheme where the sheet is clamped between two frames which contour the metal sheet. Two point incremental forming (TPIF) is a SPIF process with a back die that replaces one part of the frame. The role of the die is to provide support for the forming tool to induce compression states in the metal sheet.

- Double sided incremental forming (DSIF) is and SPIF using two tools that act on both sides of the metal sheet. This scheme is cost-efficient compared with the TPIF process, but at the same time, it requires additional algorithms to compensate for the stiffness of the forming process. The critical feature that incremental forming exhibits compared to conventional forming is that the

final part is manufacture by accumulating increments of deformation. This deformation mechanism brings about interesting observations such as higher formability and low forming force than conventional forming.

While the incremental forming process fits into the category of agile forming, there have been challenges in achieving precision in part geometry. Therefore, the forming community has tried to achieve optimal precision in the formed part while reducing trial and error. Studies show that the process parameters such as tool size, step down size, geometry parameters such as sheet thickness, and wall angle of the part directly influence the deformation occurring under the tool. A key parameter related to the metal sheet is its formability. There have been experimental studies investigating the influence of the process parameters on the formability in incremental forming, showing that the tool path influences the formability limits.

To quantitatively predicting forming results using different process and material parameters to analytical models offer a fast response with acceptable errors for informing the designing process. There are two categories of analytical models: (a) focused on predicting the geometry and thickness and (b) focused on predicting stress states and forming forces. The prediction of the geometry and thickness depends on the sine law, where the cosine of the wall angle is used to calculate the final thickness at a given section based on volume conservation and incompressibility.

However, analytical modeling, which only considers sine law, has a limitation in giving accurate quantitative prediction, which is needed in the design process. Thus, finite element models of the incremental forming process are investigated to predict the overall aspect of the forming process. Much research was conducted to optimize the modeling technique to understand how different finite element formulations can affect the prediction outcome. While some models

4

successfully provided predictions of the forming process with accuracy, it comes at the cost of expensive computation since the length of the tool path in incremental forming is generally very lengthy. Also, localized deformation only occurs in the vicinity of the tool. It creates difficulties in successfully modeling the material's behavior and hard to directly correlate the process parameters and material deformation. Thus, a new approach is needed to connect the process parameters and the material deformation, which undergoes complex strain paths and behaves differently from the sine law's predictions.

1.3. Proposed research

In incremental forming, there is a difference between the target design geometry, and an actual geometry is obtained after forming. Reducing the differences between them is the objective of the optimization of the process parameters. The smaller the differences are, the higher precision of the process is obtained. For example, in aerospace applications, an acceptable error is <5%, while in automotive prototyping, the accepted error is <10%. Achieving precision in the forming process includes various assessments related to the process setup and whether a part can be manufactured using the incremental forming process to the finer details. An analytical model with high fidelity of results is an important tool for this assessment. However, the complexity of the relationship between the process, material, and performance in incremental forming requires a physics-informed analytical algorithm, which currently does not exists. This study proposes a mew physics-informed algorithm to predict the formed geometry, including thinning and bulge. This algorithm will be developed based on the fundamental understanding of the tool-material dynamics during forming through phenomenological relationships used in a finite element model. Based on the understandings, the analytical model is developed with the principal benefit of having

a lower computation cost than finite element models but at a high confidence level of predicting the formed part's geometry.

The following tasks are proposed to accomplish the proposed research:

1) Develop a meso-macro finite element model that is capable of revealing material behavior during forming. This meso-macro model is based on a macroscale finite element model (part size) coupled with a meso-scale model (thickness size).

2) Investigate the macro- and meso-scale behavior of the material to connect the deformation mechanism with the occurrence of the defects in the material to explain phenomena such as thinning, bulging, and twisting.

3) Formulate an analytical model to predict the thickness and geometry based on the connection between the process parameter and the resultant deformation.-.

An overview of the proposed approach is shown in Figure 1.1.
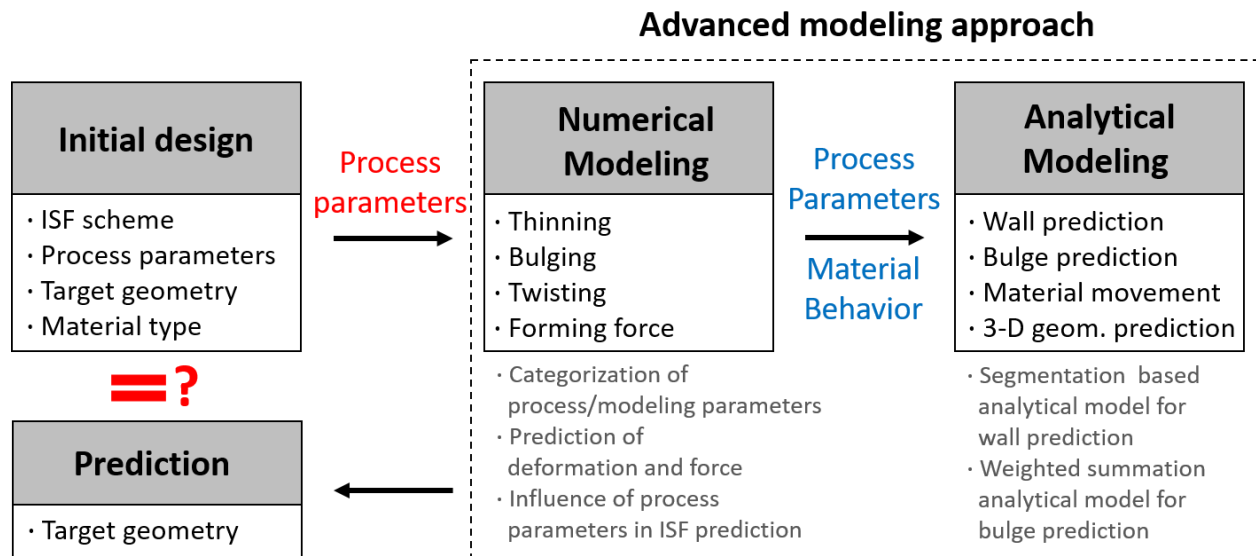
Figure 1.1 An overview of the approach of the proposed study

Based on this global view of the proposed study, three tasks are proposed and detailed as follows. In task 1, a finite element model will be developed, calibrated, and validated against the

experimental results. The goal of the task is to have a validated model where the numerically calculated deformation is reflective of the actual process. Based on the simulations' results, guidelines for selecting experimental and model process parameters will be given, which results in optimal forming results and predictions. The developed models will be utilized in the following task to explain the relationship between process parameters and the resultant deformation that is observed during the investigation of the defective phenomena.

In task 2, the model developed in task 1 is used to understand the various material instabilities that occur during the forming process. Understanding the mechanisms of the instabilities contribute to understanding the source of the deviation of the forming result. Thus, process parameters can be chosen to minimize its effect or take advantage of it during the designing process.

Finally, for task 3, based on the understanding of the defect phenomena mechanism, a correlation is made between the process parameter and the resultant deformation. Two analytical models are developed. The first model predicts the deformation in the region where the tool directly contacts the sheet. The second model predicts the deformation in the region where the tool is not in direct contact with the sheet, mainly the bulge region. The analytical models' goal is to predict forming results without using numerical calculations such as finite element models.

1.4. Expected contributions

The proposed research will impact not only furthering scientific understanding of the mechanism of incremental forming but also providing a practical contribution in designing a part and its actual forming operations. The development and usage of the advanced model approach for predicting incremental forming result will provide the following intellectual insights:

1) Understanding the formation of the thinning for high wall angled part leads to uneven distribution of wall thickness.

2) Understanding the formation of the bulge defect which can lead to an inaccurate geometry and unwanted compressive residual stresses.

3) Understanding of the formation of the twisting which can lead to changes in material property and detrimental exterior surfaces.

4) Developing relationships between the process parameter and the resulting deformation and its contribution to the occurrence of the defects.

5) Developing two novel analytical models that combined can predict the full 3-D geometry of the part without the need for numerical calculation.

1.5. Organization of the proposal

The proposal is organized as follows. Chapter 2 contains a detailed review of the published literature to provide the state-of-the-art in incremental sheet forming, analytical modeling, numerical modeling, and different material defects found in incremental forming. Chapter 3 explains the process parameters and the development of the finite element model and its various aspects contributing to the model's accuracy. In Chapter 4, various material behavior and defective phenomena found during the incremental forming are analyzed to understand the mechanism. In Chapter 5, two analytical models are presented developed based on the previous chapters' knowledge, capable of giving accurate predictions of the geometry and thickness. Combined, it provides a full 3-D prediction of the geometry and thickness. Finally, Chapter 6 summarizes the work and presents future directions.

Chapter 2 Literature Review

This section reviews the published literature related to the proposed research. The literature in the following research topics are reviewed: 1) forming mechanisms in incremental forming of sheet metals (ISF) with particularities for TPIF processes, 2) analytical and finite element modeling of SPIF and TPIF, and 3) defect prediction found during TPIF.

2.1. Formability and forming mechanisms

ISF is known to enable higher formability of the formed material compared to the conventional sheet forming process. The traditional method of characterizing formability, which uses the forming limit diagram (FLD), cannot predict the actual forming limit of the parts formed in ISF [7-9]. This limitation of the prediction of formability in ISF is because the deformations occurring during ISF did not satisfy the assumptions of the conventional FLD as presented in Emmens et al. [10], which are the following: 1) linear strain path, 2) biaxial deformation of the material, and 3) plain strain conditions. However, from the findings presented in Emmens et al., it is clear that the strain values achieved in ISF are higher than that of the part formed with the conventional process. To understand the reason for achieving higher strains in ISF without failure of the material is needed a more in-depth analysis of the ISF mechanisms. ,

The most basic method of formulating formability in ISF is the use of the wall angle of the part to be formed as the limiting factor. Young and Jeswiet [11] tested various fixed wall angles and found that the wall thickness becomes unstable, and the thinning band occurs when the wall angle gets close to maximum wall angle, which was also confirmed by Salem et al. [12]. Hussain

and Gao [13, 14] did similar work with a funnel with varying wall angles. They found that the maximum wall angle achieved in the funnel was lower than that of a cone that has a fixed wall angle. Thus, it was proposed that the largest value of wall angle for a given material be used as an indication of formability for that material when using the SPIF setup. This use of maximum wall angle allows quantification of formability for a given material. However, this definition of formability fails to include the understanding of the forming mechanism in its interpretation.

Several mechanisms have been proposed to explain the higher formability observed in ISF. These include the contribution of through-thickness shear component, contact stress/membrane stretching, bending with tension, and localized deformation resulting in suppression/localization of necking. Jackson and Allwood [15] proposed that the stretching and shear in the longitudinal direction, and shear parallel to tool motion, is the deformation mechanism in ISF. They also suggested that ISF's enhanced formability is due to the existence of the through-thickness shear [16].

Another theory for higher formability is the contact stress created due to the interaction between the tool and the sheet. The contact stress, which is mainly compressive stress, has been observed by a few [17, 18]. Silva et al. [19] presented an analytical model based on membrane analysis that incorporated the experimental observations. The equations proposed by Silva calculated the stress components induced during the contact between the sheet and tool. The work concluded that the higher formability was due to the stress in the circumferential direction being much lower for ISF than that of the conventional forming processes. This stress state induces biaxial stretching, which results in a higher strain and slows the accumulation of damage.

Several different modes of deformation coexisting during forming have been considered a stabilizing mechanism during ISF enhancing the formability. It has been widely observed that

various modes of deformation contribute to strain development during ISF. Based on the studies indicate that bending with tension can increase the formability of the material [20, 21], some have suggested that this is one of the reasons for enhanced formability found in ISF [22, 23]. Maqbool et al. [24] calculated the energy dissipated by each mode of deformation by using FEM. They found that all three modes of deformation, stretching, bending, and through-thickness shear, contribute to deformation during incremental forming. Based on the energy analysis, which determines each mode's contribution, it was concluded that increasing the contribution of bending and through-thickness shear would enhance formability.

In conclusion, in ISF, localized deformation induced by the tool is much smaller than the all-at-once deformations applied in conventional processes. Accumulation of small increments of deformation toward a large deformation of the part is possible due to suppression and localization of necking by compressive loadings through-thickness, reducing the tension in the material. This supposition was confirmed by some researchers, where they have found experimental evidence [25]. Seong et al. [26] experimentally proved that at least one portion of the sheet is in compression, which contributed to the deformation without necking, a finding also confirmed by Malhotra et al. [27]. Thus, while the damage accumulation in ISF can be faster than conventional forming due to shear and bending, its effect is localized and contained in that local region. As the tool moves, the next region experiences similar material deformation. The overall higher strain can be achieved since the strain can extend into the necking region. The studies concluded that the forming mechanisms in ISF are complex and dynamically act on the material so that large deformation is achieved in the formed part without failure.

2.2. Analytical models for ISF

Analytical modeling of the process provides valuable information by quantitatively expressing the underlying relationship. It helps understand the fundamentals of the process and develop efficient predictive models that can be more insightful than the finite element models.

The most known analytical model that was developed for the ISF process is the sine law [28, 29]. The sine law has been widely used to predict thickness in incremental forming based on volume conservation and geometry projection. The sine law originates from its application on spin forming. The approach is based on the projection of the blank onto the mandrel surface, which predicts the shear deformation occurring during the process. By knowing the initial thickness and the wall angle of the part, the following relationship as given in Equation (2.1) between deformed thickness t, original undeformed thickness t_0, and wall angle α can be derived.

$$t = t_0 \sin(90° - \alpha) = t_0 \cos \alpha \tag{2.1}$$

The sine law can be further expanded to the 3-D version, where the thickness is expressed as the ratio of the deformed area to the original area. The 3-D sine law given in Equation (2.2) which is described as

$$t = t_0 \frac{A_0}{A} \tag{2.2}$$

where t and t_0 denote the deformed and undeformed thickness while A and A_0 denote the deformed and undeformed areas, respectively. Bambach et al. [30] utilized this equation to predict the thickness of pyramids. Kim and Yang [31] used the above equation for developing thickness prediction for the ellipsoidal cup and clover cup for a double-pass ISF. The sine law provides the first-order prediction of the thickness distribution, enabling the designer to roughly select sheet thickness to fit the target geometry's thickness criterion. While these predictions require a minimal computational cost, they could lack accuracy for a complicated geometry.

Many works laid the groundwork on the analytical model development by providing stress and strain observations. The incremental forming is known to exhibit a complex mode of deformation. Jackson and Allwood [15] have provided extensive experimental data that through-thickness shear occurs during both the SPIF and the TPIF process. He et al. [32] investigated the strain components generated during the SPIF process. They found that tangential strain is small compared to the radial strain making the SPIF process for simple cone a nearly plane strain condition. Flores et al. [6] also measured both radial and tangential strain and found that tangential strain is significantly lower than radial strain. This observation was confirmed by FEA analysis using a variety of combinations of constitutive material models, leading to the conclusion that simple cone parts exhibit plane strain conditions on the wall section.

Based on these works, analytical models based on the stress-strain relationship have been created to understand the deformation mechanism during incremental forming. Fang et al. [33] created an analytical model based on the plane strain deformation, which considered the material hardening and bending effect. This model was found to be valid for axisymmetric parts with large wall curvature. Silva et al. [19] used membrane analysis based on plane strain conditions to express the stress components in the symmetric part analytically and to explain the forming mechanism of ISF. Chang et al. [34] developed an analytical force prediction model for the SPIF and the multi-pass incremental sheet forming (MPISF). He considered the contact area beneath the tool and applied the membrane analysis proposed by Silva. These works on axisymmetric parts such as simple cones have provided evidence that material deformation in the walls can be approximated to plane strain conditions. However, Bambach [30] has shown that pyramids with small corners exhibit lower principle strains, which leads to biaxial stretching where plane strain assumption could be misleading. Ai et al. [35] suggested an analytical model based on both plane-strain and

equibiaxial stretching conditions. The model considered both the sheet bending and material strain hardening to explain the fracture during the ISF process.

2.3. Finite element modeling of ISF

2.3.1. Constitutive material models for ISF

The simplest combination of yield function and hardening law regarding the number of the material parameters that need to be identified is anisotropic hardening law and von Mises yield criteria. As shown in the work of Li et al. [36], Swift type hardening law and von Mises yield criteria are used to model a truncated cone with the wall angle of 60° with the step down of 0.5mm for the aluminum alloy 7075-O. The equations for Swift law and von Mises yield criteria are given below in Equation (2.3) and Equation (2.4)

$$\sigma = K(\varepsilon_0 + \varepsilon)^n \tag{2.3}$$

$$\sigma_{Mises} = \frac{1}{2}\left[\left(\sigma_{11} - \sigma_{22}\right)^2 + \left(\sigma_{22} - \sigma_{33}\right)^2 + \left(\sigma_{33} - \sigma_{11}\right)^2 + 6(\sigma_{12}^2 + \sigma_{23}^2 + \sigma_{31}^2) \right] \tag{2.4}$$

where K is the plastic coefficient and n the hardening exponent in the Swift law. Li was successful in predicting strains and forming forces using a solid element with LS-Dyna FEM software. Robert et al. [37] also successfully used the combination of swift type hardening law and von Mises yield criteria but with ABAQUS FEM software. It was found that the errors acceptable while witnessing a reduction in the computational cost.

Flores et al. [6] highlighted the importance of material parameter identification by showing its impact on prediction. A biaxial tensile testing machine was utilized to obtain the coefficients of the yield function for Hill (1948) shown in Equation (2.5) and Hosford (1979) shown in Equation (2.6), which are defined as

$$F_{Hill}(\bar{\sigma}) = \frac{1}{2}\left[(H+G)\sigma_{11}^2 + (H+F)\sigma_{22}^2 - 2H\sigma_{11}\sigma_{22} + 2N\sigma_{12}^2\right] - R_0^2 = 0 \qquad (2.5)$$

$$F_{Hosford}(\bar{\sigma}) = H\left|\sigma_{11}-\sigma_{22}\right|^a + G\left|\sigma_{11}\right|^a + F\left|\sigma_{22}\right|^a - R_0^a = 0 \qquad (2.6)$$

Where $\bar{\sigma}$, H, G, F, N are the material parameters for in-plane stress state and R_0 the initial yield stress. For Hosford yield criterion, which is non-quadratic, $a = 6$ for suitable for Body-Centered Cubic (BCC) materials, and Face-Centered Cubic (FCC) materials are used where for ISF modeling. The parameters of the Hosford criterion are identified based on the Lankford coefficients. It was shown that the material model has an impact on the accuracy of the FEM model significantly. In the case of SPIF, the mixed hardening model resulted in improved numerical prediction [38]. The effect material testing method for identifying the material parameters, the effect of the type of element, and the effect of constitutive law on the force prediction accuracy was investigated. The work studied the impact of two yield functions, isotropic von Mises yield locus and Hill48 (1948) quadratic yield function with four different hardening laws; isotropic Swift hardening law, isotropic Voce hardening law, kinematic Armstrong-Fredericks law, and kinematic Ziegler law. For low angled parts, shell element using both isotropic and mixed material model was able to capture forces accurately. For high angled parts, saturating hardening law and mixed hardening laws resulted in higher accuracy. The highest accuracy was reached with brick elements with a fine mesh with a material model of isotropic von Mises yield function with mixed isotropic-kinematic hardening model of Voce-Ziegler. Eyckens et al. [39] and Bambach et al. [40] compared the effect of isotropic yield criteria and anisotropic yield criteria combined with isotropic hardening and kinematic hardening. The result of the simulation was validated against experimental measurement obtained using Digital Image Correlation (DIC). A good correlation between surface strains and process parameters was gained except for the strain components directly under the tool. This deviation was explained with through-thickness shear. Yue et al. [41]

went further by investigating the influence of the yield surface distortion induced by the ISF process nonlinear loading path and showed that yield surface distortion could influence the plastic strain distribution and ductile damage.

The effect of the yield functions on the forming forces was examined by Esmaeilpour et al. [42]. In his study, the Yld 2004 -18p Barlat yield function [43] was compared with the conventional isotropic von Mises yield function and Hill 1948 anisotropic yield function. The Barlat Yld 2004-18 is shown in Equation (2.7)

$$
\begin{aligned}
\varphi = \varphi(\overline{S}', \overline{S}'') = {} & \left| \tilde{S}_1' - \tilde{S}_1'' \right|^a + \left| \tilde{S}_1' - \tilde{S}_2'' \right|^a + \left| \tilde{S}_1' - \tilde{S}_3'' \right|^a + \left| \tilde{S}_2' - \tilde{S}_1'' \right|^a \\
{} & + \left| \tilde{S}_2' - \tilde{S}_2'' \right|^a + \left| \tilde{S}_2' - \tilde{S}_3'' \right|^a + \left| \tilde{S}_3' - \tilde{S}_1'' \right|^a + \left| \tilde{S}_3' - \tilde{S}_2'' \right|^a + \left| \tilde{S}_3' - \tilde{S}_3'' \right|^a = 4\overline{\sigma}^a
\end{aligned}
\tag{2.7}
$$

where a=6 and a=8 are selected for BCC and FCC materials, respectively. The $\overline{\sigma}$ is the flow stress, $\tilde{S}_i'$ and $\tilde{S}_j''$ are principal values of the tensors $\tilde{s}'$ and $\tilde{s}''$ which are defined by the two linear transformations on the stress deviator *s*. Material characterization tests are conducted to calculate the 18 parameters of the yield function. The dynamic/explicit models in ABAQUS FEM software were used to run the material models. The forming force, thickness, strain, and stress components were compared, respectively. It was seen that the thickness distribution and strain distribution showed closely matching data, while triaxiality and lode parameters showed a matching trend with small differences. The out-of-plane components were chosen as the same values as ones in the in-plane direction in Esmaeilpour et al. [42]. However, in the successive work in Esmaeilpour et al. [44], the crystal plasticity FEM approach was used to calculate the out-of-plane components. These coefficients have proven to be hard to calculate experimentally for sheet metals since they are too thin in the thickness direction to conduct material experiments. The out-of-plane coefficients were calculated using the representative volume element (RVE) and CPFEM

approach. The result shows that Barlat 2004 -18p predicted lower forming forces for all three components of the force; however, the computational time increased by utilizing Barlat 2004-18p.

It can be concluded that the different combinations of material models can result in varying levels of accuracy. The more complicated the material model is, it takes extensive experimental work to identify the material coefficient required for the model. However, it does not necessarily guarantee an increase in accuracy and can lead to long computational time. Depending on the material and the target geometry, a different material model with different combinations has to be selected to suit the user's needs for accuracy and computational time.

2.3.2. Selection of numerical parameters

Numerical parameters have an essential role in finite element modeling, impacting the precision of calculations, convergence, and computation time. The integration scheme, contact formulation, and boundary condition are the most important among the numerical parameters. The integration scheme is the method of solving the finite element differential equation to obtain an approximate solution. There are two schemes, the explicit integration scheme, and the implicit integration scheme. Each method has its advantages and disadvantages. The implicit scheme utilizes the Newton-Raphson method to integrate the static equilibrium equation. This method allows unconditional stability and better accuracy while requiring a considerable computational cost due to the iterations. The explicit scheme uses the forward Euler method to calculate the dynamic equilibrium equation. This method is conditionally stable and can lead to significant errors if increment error is not kept small. For quasi-static problems that the ISF process falls into, both implicit and explicit schemes can be used. Generally, the explicit method is advantageous in simulating incremental forming due to its capabilities to adjust time increments using numerical manipulations such as mass scaling, reducing the computational cost significantly. It can be seen

that some have turned to the implicit scheme [6, 38, 45-48], and others have utilized explicit schemes [36, 37, 39, 41, 42, 44, 49-51]. The accuracy and computational cost vary greatly between the different works. This difference may be due to the differences in the integration scheme and other factors such as material model and element type.

The element formulation plays an important role in achieving high accuracy in prediction. Due to the high level of nonlinearity and localized deformation occurring during the incremental forming process, the difference in the element formulation results in different computation time and accuracy. Bambach et al. [40] investigated the influence of the different types of elements and the various combinations of basic constitutive models on accuracy and computation time. It was shown that reduced integrated solid elements with hourglass control proved to have the best overall performance when comparing the accuracy and computational cost.

Many works have investigated the use of shell elements for modeling the deformation behavior of the ISF process [46, 47]. The formulation of shell elements coincides well with the forming mechanism theory that the in-plane deformation dominates the ISF process. This same approach was also observed in the membrane analysis proposed by Silva et al. [19]. However, the use of solid elements has been explored by others [36, 42, 45, 49, 50]. One of the critical deformation occurring in ISF is the strains in the thickness direction. The solid elements proved to accurately capture the thickness direction stress and strains regardless of the different combinations of material constitutive models used. Malhotra et al. [48] showed that in some cases, shell elements could result in a better force prediction while lacking in accuracy for the prediction of the thickness distribution. In contrast, the model with the solid elements showed opposite results. While the computational cost can vary depending on the optimization of the model, it has been observed that shell element generally results in lower computational cost than solid elements.

However, To lower the computation cost to the extreme, Ben Ayed et al. [51] have used Discrete Kirchoff Triangle Shell elements (DKT12) with a simplified contact procedure. It was shown that computational cost could be lower by 60% with errors in the acceptable range for two specific geometry cases.

Some have turned to solid-shell elements due to limitations existing for both solid and shell elements. The solid element has high computation cost, and the shell element does not accurately predict the deformation in the through-thickness direction. It was shown that the solid-shell elements were able to provide an accurate prediction of the thickness and forces [52]. Adaptive remeshing was introduced to decrease the additional computational cost associated with using the complex element formulation found in solid-shell elements. The method showed a significant decrease in the computational cost, as shown in De Sena et al.[45].

Many factors contribute to the model's accuracy, with each unique combination resulting in a different amount of computational cost. Various impact of the model parameters is investigated to understand the recent advancements in the modeling of ISF. It can be concluded that the complicated nature of the ISF process makes the development of the finite element model difficult and that further studies need to be conducted.

2.4. Summary and conclusions

The literature review of the topics that are related to this thesis is presented in this chapter. Various theories have been introduced to explain the material behavior occurring during the ISF process. These theories on the forming mechanism of ISF allow one to understand the ISF process's unique characteristics that are different from the conventional sheet metal forming process. Among the proposed theories, the suppression of necking and localization of necking provides the most convincing reasons for the ISF process having higher formability than the conventional process.

The development of the models, numerical and analytical, plays a critical role in understanding the mechanical behavior in incremental forming. In analytical modeling, sine law was utilized to provide geometric predictions, while some have turned to the stress-strain relationship with various assumptions to describe the material behavior during forming. In numerical modeling, many works have been done to understand the effect of material modeling on the forming performance. Different combinations of yield functions and hardening laws were considered to find the optimal material constitutive model, leading to the highest accuracy of thining and bulge prediction. It was observed that the hardening law and yield function specific to the material and geometry must be selected to achieve optimal prediction.

Chapter 3 Modeling of Incremental Forming

In this chapter, a finite element model (FEM) is developed to simulate the incremental forming process, mainly focusing on the deformation of materials. The model serves as a tool for understanding the influence of the process parameters on the forming process's outcome. It also provides insight into the deformation of the material in the vicinity of the tool that contributes to the unique deformation seen in incremental forming. Another significant contribution of this chapter is providing an accurate assessment of the model parameters and the range of prediction errors they produce. This knowledge allows the users to choose the proper model parameters for ISF simulation and utilize it to reduce trial and error in both the experiment and the modeling approach. The goal is to investigate the influence of different parameters used in experiments and modeling and provide a guideline for the optimal process parameter range based on their impact on the forming force and part geometry.

This chapter presents the original approach to understand the mechanical behavior of the material during forming by developing an original meso-macro scale finite element model. The expected contributions are to relate the process parameters with phenomena that develop in the material and generate relationships such as the influence of the tool size or step size on the surface roughness of the parts as well as the influence of the tool path on the accuracy of geometry prediction

In the following section, details of the FEM model are presented, starting by describing how each process parameter is incorporated into the model and, with the model parameters, how

they influence results. The key model parameters are investigated, and their prediction results are validated compared to experimental results.

3.1. Incremental forming schemes and associated process parameters

3.1.1. Incremental forming schemes

The incremental forming can be divided into three different schemes. The first scheme is the single point incremental forming (SPIF), which only utilizes a single tool with the sheet clamped between the two clamps. This scheme is the truly die-less form scheme in incremental forming, as shown in the schematic in Figure 3.1. The second scheme is the two point incremental forming (TPIF). This scheme utilizes a die in the back clamp where the die's presence allows the forming of concave and convex shape with higher accuracy than that of single point incremental forming, which can lack geometric accuracy in the region near the clamp and for complex geometry, as shown in Figure 3.2. Also, the die's presence allows squeezing the material to induce extra thinning and compressive stress. This squeeze can enhance the formability of the material due to increased hydrostatic pressure. However, it can also result in squeezing out material and contributing to a bulge formation in the undeformed section. The third scheme is called double sided incremental forming (DSIF), which utilizes a second tool in the place of the die in TPIF. This work will focus on the two incremental forming schemes, the SPIF and the TPIF, which share many common aspects yet have some profound differences. The DSIF, which displays characteristics that are quite different from the SPIF and the TPIF, will not be considered in this work.
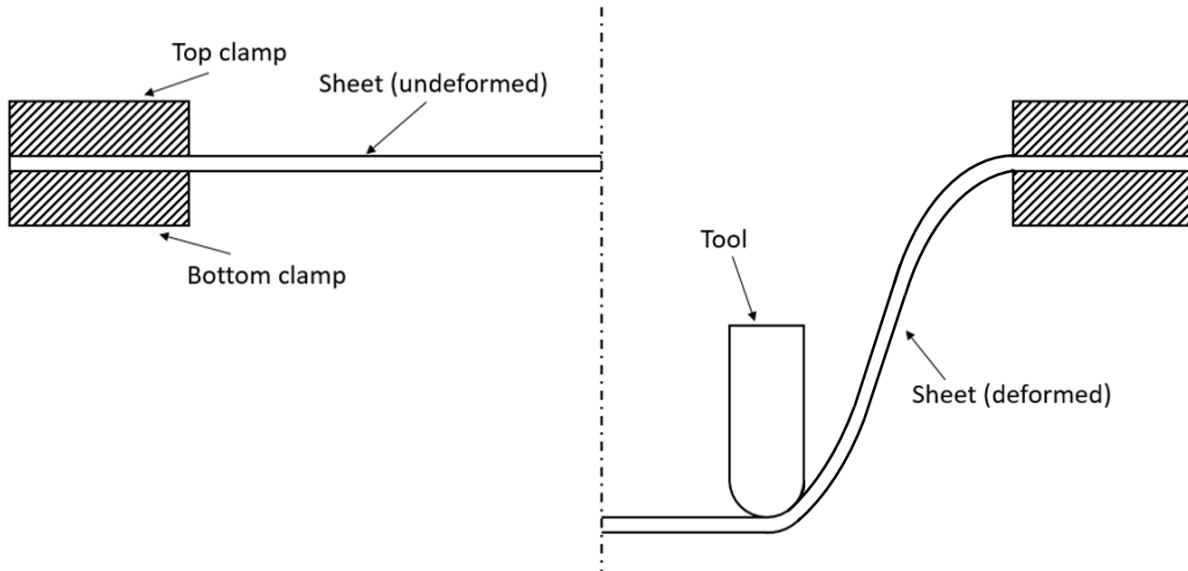
Figure 3.1 Schematic of the Single Point Incremental Forming (SPIF) setup
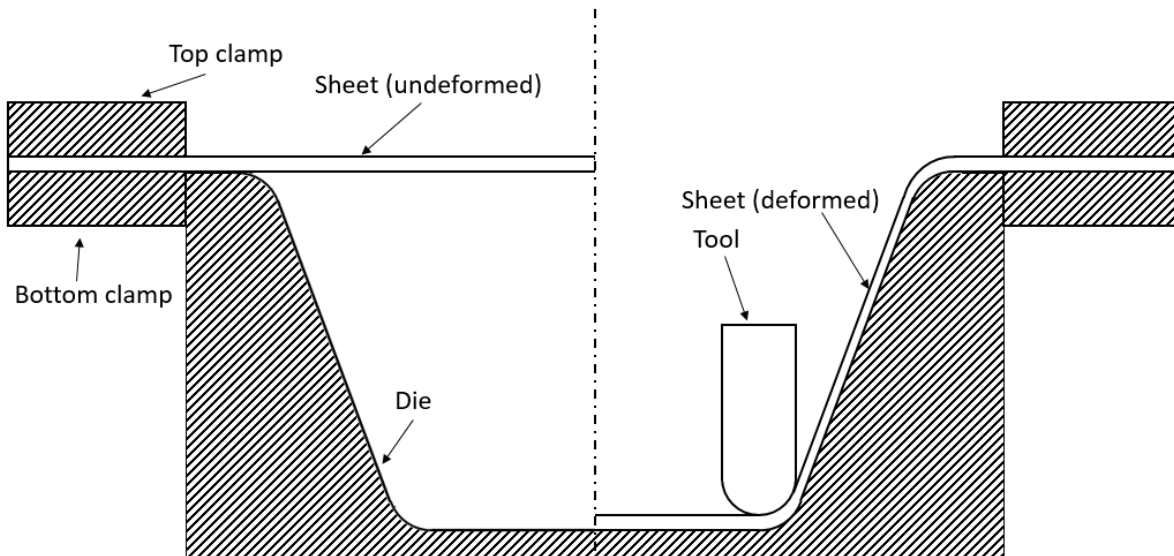
Figure 3.2 Schematic of the Two Point Incremental Forming (TPIF) setup

The incremental forming, both the SPIF and the TPIF process, is dictated by a series of process parameters. The uniqueness of these process parameters that are not found in conventional forming allows the incremental forming process to differ from other forming processes. In the sheet metal forming process, in both the conventional and ISF processes, tunning of the process

parameter is a costly trial and error process. In the conventional sheet metal forming process, this tuning process involves investigating each of the process parameters' influence to understand its effect on the forming outcome. While this approach is still valid, it is not easy to apply the same approach to incremental forming. This is because the number of process parameters is much larger in ISF, and the impact of the process parameters are coupled together into localized deformation. Thus, it is hard to distinguish the effect of one single parameter. With the use of the finite element method (FEM) modeling techniques, it is possible to simulate the different process parameters to understand their effect on the forming result.

3.1.2. Categorization of the process parameters

The process parameters are common throughout the experiment and model. However, there exist experimental parameters and model parameters, respectively. The experimental parameters are the parameters associated with the experimental process. These experimental parameters will have their counterparts in the models that play a similar role in the model. In many cases, the model parameters derived from the experimental process mirror its effect, and one experimental process parameter can influence one or more model process parameters.
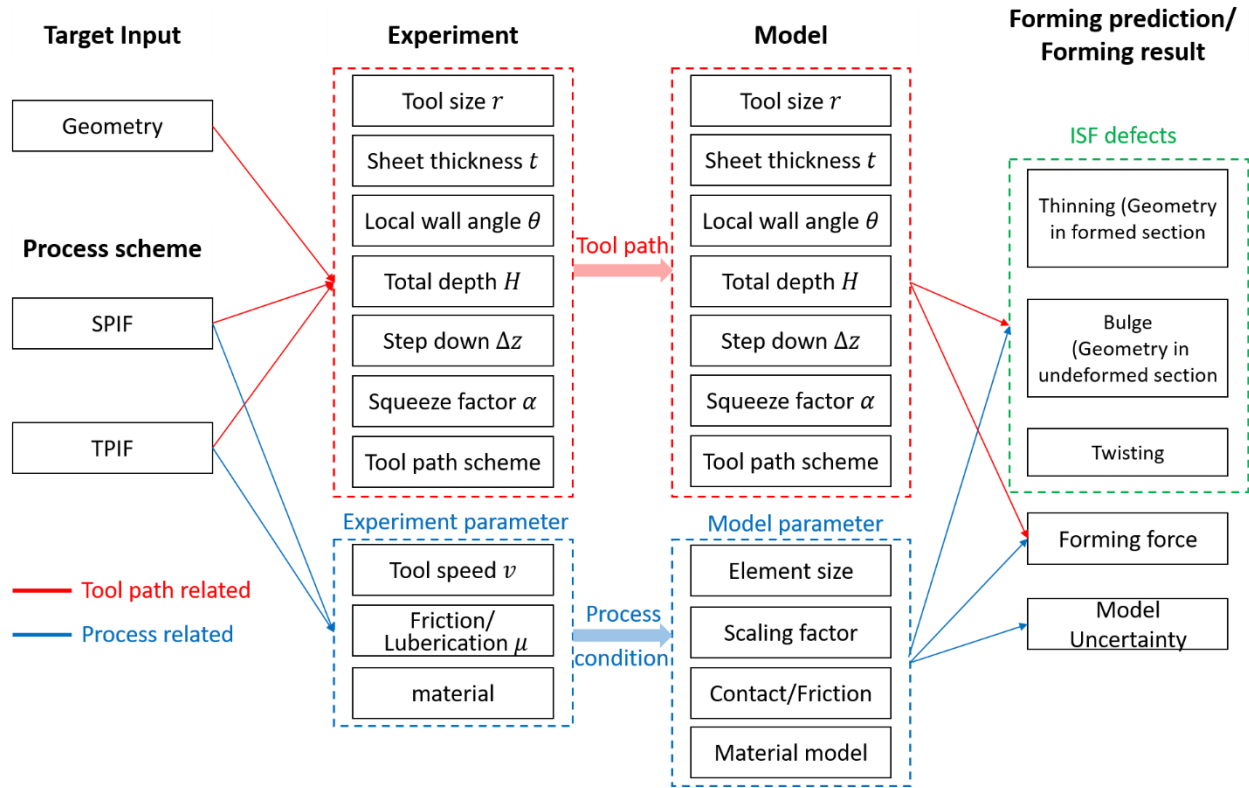
Figure 3.3 Flow chart of process parameters

The process parameters common in SPIF and TPIF include tool radius r, sheet thickness t, wall angle θ, step down Δz and the experimental parameters tool speed v, friction between the tool and the sheet μ. For TPIF, there exist an addition process parameter of squeeze factor α. These process parameters and experimental parameters are integrated into the FEM model with the same process parameters and model parameters. The model parameters consist of the material model, the element formulation and the size, the contact formulation and friction, and the scaling factors for artificially increasing the model's speed. These parameters influence the output of the model, which can be categorized into four segments. The thinning region, where the deformation of the material occurs by direct tool contact. The bulge/flange region where the deformation of the material occurs by indirect tool contact. The forming force prediction and the artificial errors

associated with the calculation process. How each of the experimental parameters is incorporated into the model process parameter also affects the prediction result.
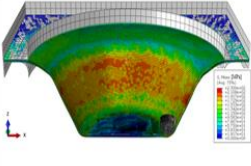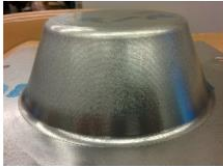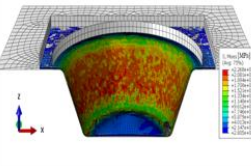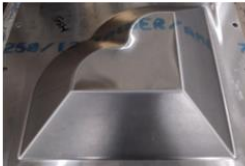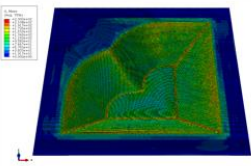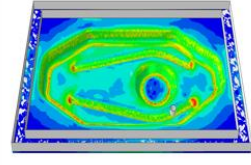
The goal of the model is to provide practical guidelines for establishing the process parameter based on the established model observation. While all of the process parameters play a role in the incremental forming process, some of the process parameters that play a more crucial role will be investigated in more detail. In contrast, others, such as tool speed, may remain constant throughout.

3.2. Experimental setup for model validation and investigated geometry

3.2.1. Investigated part geometries

The part geometries investigated using FEM modeling are 45° cone, 67° cone, heart, and a Boeing-model fuel cover. The 45° and 67° cones were modeled with both SPIF and TPIF schemes. The heart and the cover were modeled with only TPIF. First, the model is established based on simple geometries such as cones, which are easy to validate. Next, the model is expanded to more complicated geometry such as the heart and the cover. Two wall angle values were chosen for the cone: 45° and 67°. The 45°cone is a value representing a moderate wall angle, which lies within the forming limit. The 67° cone represents a high wall angle near the forming limit for the given material of AA7075-O.

Table 3.1 List of investigated geometry

Investigated Geometry	ISF Scheme	Experiment	Model
Cone (67°, 45°)	SPIF		
	TPIF		
Heart	TPIF		
Cover	TPIF		

3.2.2. Experimental setup

The parts are manufactured on a Cincinnati HMC 400 EP CNC milling machine integrated with a 4-component KISTLER force sensor. The general layout of SPIF consists of a sheet of aluminum AA 7075-O clamped between top/bottom clamp with a hemispheric tool doing the forming. For TPIF, the bottom clamp is substituted with the backing die. A hemispheric tool is set to moves at the speed of 100 inches per minute with varying degrees of step down. A layer of MoS_2 multipurpose grease is applied on the sheet surface to reduce friction in the tool-sheet interface. Forming forces are continuously recorded and monitored at 100 Hz frequency using a custom-built Labview interface with the force sensor.
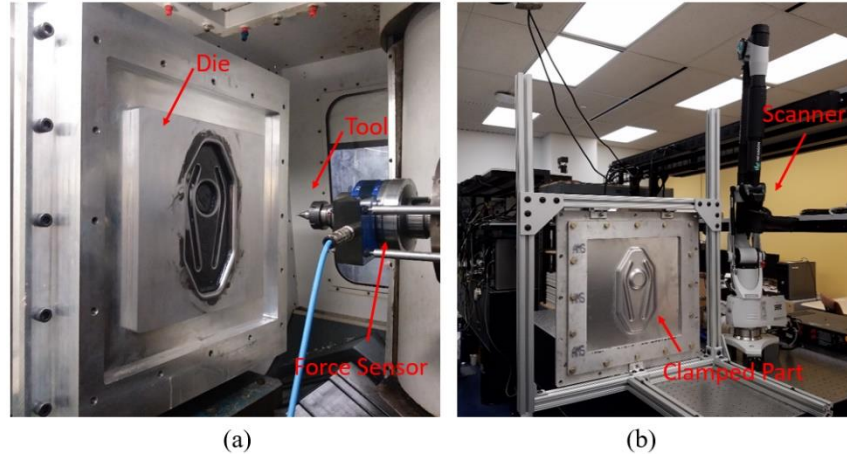
Figure 3.4 Experimental Setup of TPIF including a die, tool with a mounted force sensor (a), and laser scanner setup with clamped part (b)

To measure the geometry and calculate the deviation of the incrementally formed part from the original design, a laser scanner, Romer Absolute Arm with Integrated Scanner 7525SI, was used. It has the capacity of single point repeatability and scanning system accuracy of 0.027mm and 0.063mm, respectively. The Polyworks Inspector software collects the data in the point cloud format during the scan and meshes them into surfaces. Once the scan is complete, a CAD file is imported into the Polyworks Inspector software and is used as a reference. Post-processing of the data is conducted to match the point cloud data's coordinate system to that of the reference CAD by translation and rotation. These results are then compared with the results of the model for validation purposes.

3.3. Finite element modeling of incremental forming

The general setup procedure for the FEM model is as follows. First, the domain has to be defined and divided into a finite number of nodes and elements. The domain consists of parts such as the sheet, the tool, and the clamp/die. The way they are meshed influences the accuracy and the computational cost of the prediction. Then, boundary conditions are defined for each of the parts. These conditions are encasting the bottom clamp/die, applying a clamping force to the top clamp

to hold the sheet in place, assigning the movement of the tool along with its constraints. Next, material properties are assigned to each part. Most importantly, the elastoplastic material property is assigned to the sheet. A series of material tests are conducted to derive the material properties used to calculate the material models' parameters. Finally, the contact between the part, tool, and die is defined, and the model is calculated using an explicit integration scheme.

3.3.1. General layout of the finite element model for SPIF and TPIF

Finite element model layout for SPIF scheme

The general layout of SPIF consists of a sheet of aluminum AA 7075-O clamped between top/bottom clamp with a hemispheric tool doing the forming. Figure 3.5 shows the established model of SPIF for 67° cone with the image of the initial and final prediction result from the model.
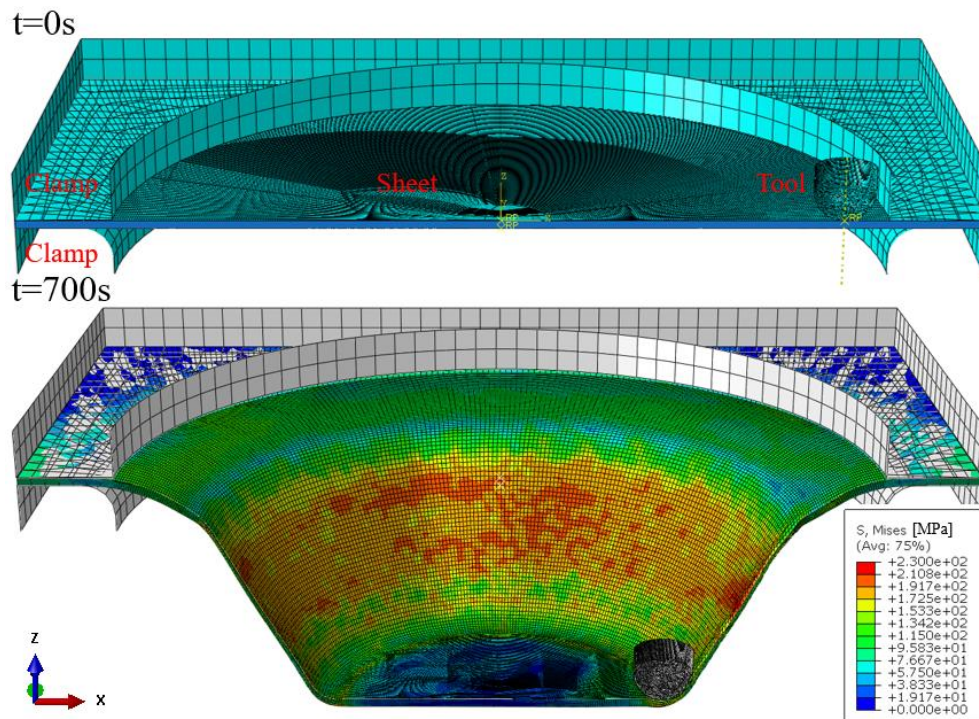
Figure 3.5 SPIF setup of 67° cone

Finite element model layout for TPIF scheme

The general layout TPIF model is similar to that of the SPIF but with a backing die in the place of the bottom clamp. Figure 3.6 shows the established model for TPIF for 67° cone with the image of the initial and final prediction result from the model.
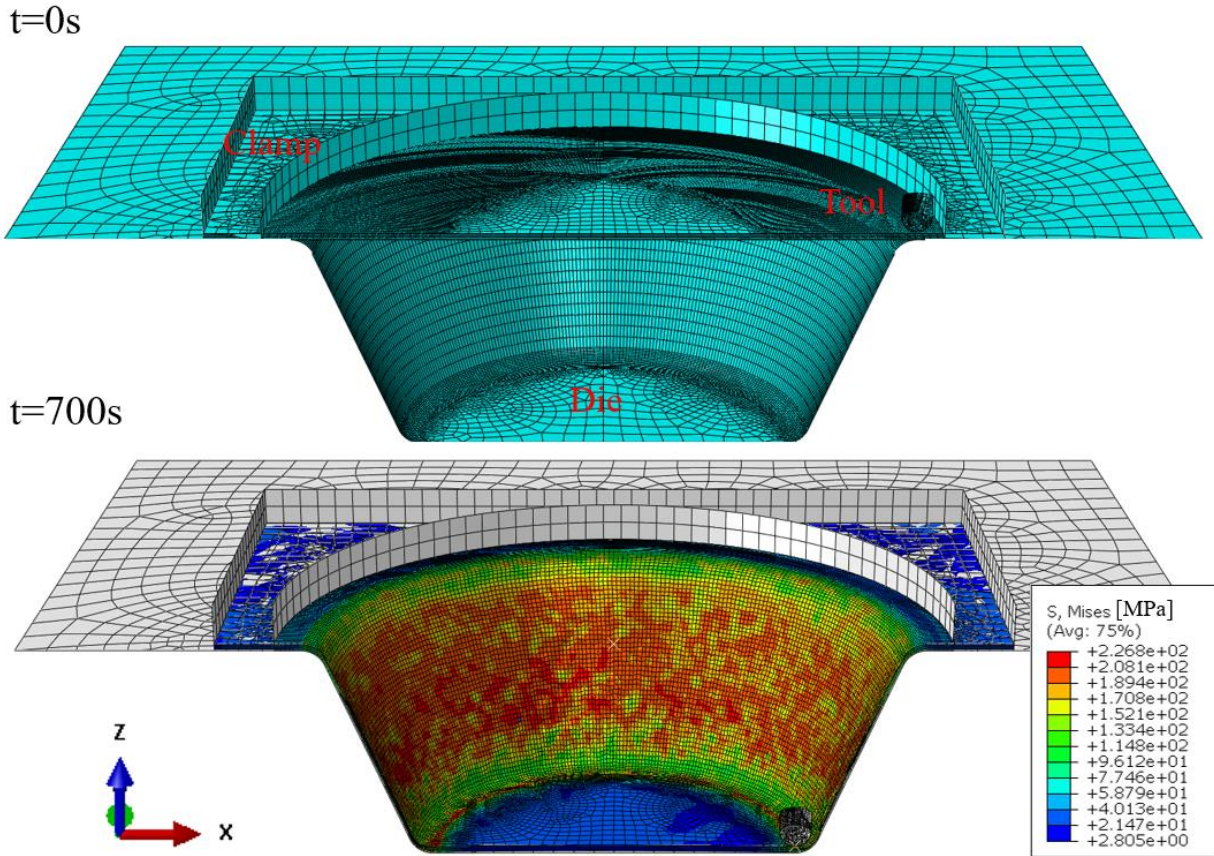
Figure 3.6 TPIF setup of 67° cone
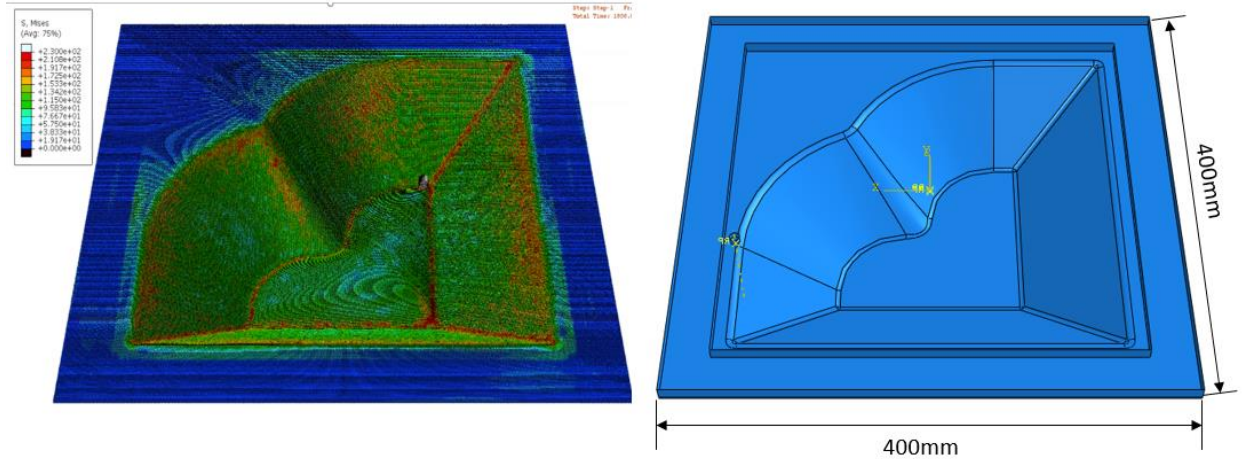
Figure 3.7 TPIF CAD and FEM results for the heart shape
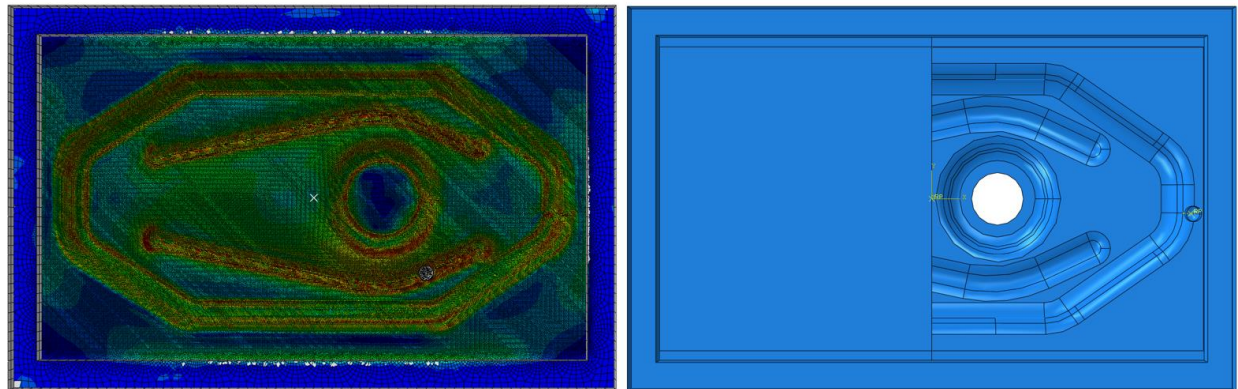
Figure 3.8 TPIF CAD and FEM results for the cover

3.3.2. Tool path for incremental forming

The tool path in incremental forming plays a crucial role in controlling the movement of the tool. All of the deformations in incremental forming are induced by the tool. Thus, any wrong tool movement can negatively impact the outcome of the forming operation. The experimental tool path is created by considering the tool size, the sheet thickness, the step-down size, the wall angle, and the total height. In the case of TPIF, the squeeze factor is additionally considered.

The tool path for the cones was generated using Matlab code, while the tool path for the heart and the cover was created using AMPL tool path software, which was developed by the Cao

group at Northwestern. The experimental tool path is translated into the model tool path. But during the transition, the tool position is compensated by the amount of the tool deflection to provide the actual tool position during forming. Depending on the amount of compensation occurring, the actual tool path could be significantly different from the original design tool path if large tool deflection occurs. However, this compensation allows the model to mimic the experimental condition and eliminate complications with the tool deflection problem. The tool path is read in tabular format in the amplitude section and applied as a displacement boundary condition to the reference point at the tool tip.

3.3.3. Material model

The material model is what represents material behavior for the choice of material used during the forming process. The stress and strain distribution in ISF is more complicated and nonlinear than the conventional sheet metal forming processes, such as deep drawing or hydroforming. The constitutive equation can be simplified enough to solve the constitutive equation for analytical solutions. This complicated deformation mechanism puts emphasis on choosing the right material model in FEM, which can reflect the behavior or material to obtain accurate prediction results. The choice of different yield functions and hardening in law for the material model can range from simple von Mises yield with isotropic hardening law to complicated Barlat type yield with anisotropic hardening law. This section looks closely at the influence of the yield function and hardening to give the users information about the outcome of the process with given input for the aerospace-grade aluminum AA 7075-O.

<u>Behavior under tensile loading</u>

The behavior of material to the tensile loading is the most well-known way of characterizing the behavior of metals. Most FEA software has material cards already built for

tensile behavior requiring the values for the associated parameters. To obtain a stress-strain relationship under tension, tensile tests were conducted on the MTS Insight 10 Mechanical Tester with the sheet metal samples created based on the ASTM B557M standard. The samples were taken every 15° relative to the rolling direction to test the material's anisotropy. The strains were measured with both a 50mm extensometer and correlation solution's DIC. The tests were repeated three times per direction, and the results were converted to true stress and true strain. The data were averaged, and the deviation was calculated to check for any anomalies in the material properties. The 0.2% offset method was used to determine the yield point of the material, and only the plastic portion of the data was taken and plotted using Matlab. The results were compared with the literature value given in the Atlas of Stress-strain Curves [53]. The stress and strain values were converted to equivalent stress and strain and then to true stress and strain. The stress-strain diagram of the tensile test is shown in Figure 3.9.
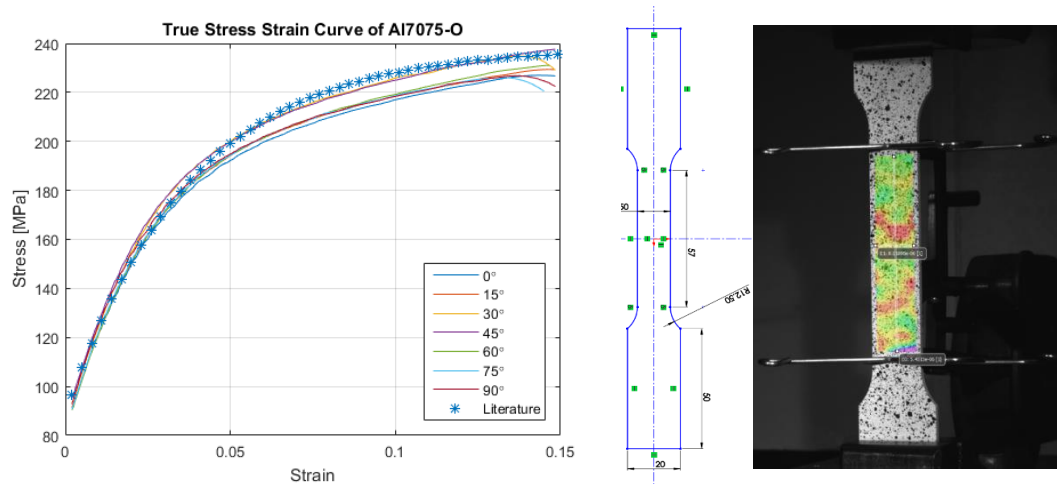
Figure 3.9 a) Stress-strain curve, b) sample dimension, and c) DIC image

The stress-strain diagram was fitted with a Voce-type hardening law as described in Equation (3.1) to describe the is isotropic hardening properties of the aluminum alloy

$$\overline{\sigma} = k_0 + Q(1 - e^{\beta \varepsilon^p}) \tag{3.1}$$

where $\bar{\sigma}$ is the effective stress, ε^p is the effective plastic strain, and k_0, Q, and β. The basic material parameters and exact value for the parameters for the hardening law are defined below in

Table 3.2 Elastic properties of AA5754-O and material parameters for the Voce hardening law

Modulus	Yield Strength	Density	Poisson's Ratio	k_0	Q	β
69.74 GPa	89 MPa	2810 kg/m^3	0.33	91.30 MPa	149.34 MPa	26.71

Behavior under cyclic loading

The kinematic hardening is another way of modeling the hardening behavior in metal where the yield locus does not expand but moves around based on the back stress. The kinematic hardening was implemented with a nonlinear kinematic hardening model based on the associated flow rule provided in the Abaqus 6.14-1. The back stress of the kinematic hardening law is described by the following equations given in the Abaqus 6.14 manual [54].

$$\alpha_i = \sigma_i - \sigma_i^0 \tag{3.2}$$

$$\alpha = \frac{c}{\gamma}(1 - e^{-\gamma \varepsilon^p}) \tag{3.3}$$

Where the parameters C, and γ are the hardening modulus and the rate at which the kinematic hardening modulus decrease with increasing plastic deformation. These coefficients are calculated from back stress α using Equation (3.2) and Equation (3.3), which is calculated for each given set of half-cycle data $(\sigma_i, \varepsilon_i^p)$.
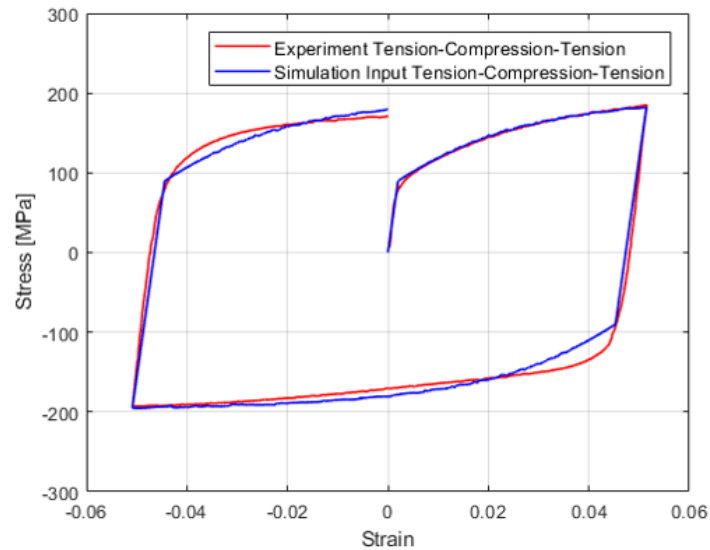
Figure 3.10 Calibration of the kinematic hardening model with the TCT test [43]

The cyclic hardening law curve, derived based on the tensile behavior, was later compared with the experimental tension-compression-tension curve. The experiment was conducted by the Cao group at Northwestern University, as shown in Figure 3.10. The result show sign of Bauschinger effect when going through compression after tension. However, the difference between the two curves can be considered small enough to conclude that it would significantly differ in the finite element model's outcome.

Material yield function

The yield function plays a vital role in determining whether the material subjected to deformation has undergone strains that would induce plastic deformation. von Mises yield criteria are one of the most widely used yield criteria for its ease of implementation. It does not require calibration of the coefficient like in other yield functions. This simple form has made von Mises yield function a popular yield function for material that does not exhibit strong anisotropy. The von Mises yield function is described as

$$\sigma_{Mises} = \frac{1}{2}\left[\left(\sigma_{11} - \sigma_{22}\right)^2 + \left(\sigma_{22} - \sigma_{33}\right)^2 + \left(\sigma_{33} - \sigma_{11}\right)^2 + 6(\sigma_{12}^2 + \sigma_{23}^2 + \sigma_{31}^2)\right] \qquad (3.4)$$

where σ_{Mises} denotes the equivalent von Mises yield stress, σ_{11} the stress component (MPa) in the circumferential direction, σ_{22} the stress component (MPa) in the meridional direction, σ_{33} the stress component (MPa) in through-thickness direction and σ_{12}, σ_{23}, and σ_{13} their respective shear stress components (MPa).

From the tensile test in various directions, it was seen that the AA 7075-O does not exhibit strong anisotropy. However, anisotropic yield functions are implemented to check the influence of mild anisotropy on the prediction result. The most simple is the Hill 48 yield criteria. The Hill 48 yield function is described as in Equation (3.5) [55].

$$f_{Hill}(\sigma) = \sqrt{F(\sigma_{22} - \sigma_{33})^2 + G(\sigma_{33} - \sigma_{11})^2 + H(\sigma_{11} - \sigma_{22})^2 + 2L\sigma_{23}^2 + 2M\sigma_{31}^2 + 2N\sigma_{12}^2} \quad (3.5)$$

The parameters F, G, H, L, M, and N are constants obtained by a test of the material in different obtained in a different orientation. As for the stress components, σ_{11} is the stress component (MPa) in the circumferential direction, σ_{22} the stress component (MPa) in the meridional direction, σ_{33} the stress component (MPa) in through-thickness direction and σ_{12}, σ_{23}, and σ_{13} their respective shear stress components(MPa).

$$F = \frac{1}{2}\left(\frac{1}{R_{22}^2} + \frac{1}{R_{33}^2} - \frac{1}{R_{11}^2}\right)$$

$$G = \frac{1}{2}\left(\frac{1}{R_{33}^2} + \frac{1}{R_{11}^2} - \frac{1}{R_{22}^2}\right)$$

$$H = \frac{1}{2}\left(\frac{1}{R_{11}^2} + \frac{1}{R_{22}^2} - \frac{1}{R_{33}^2}\right) \tag{3.6}$$

$$L = \frac{3}{2R_{23}^2}$$

$$M = \frac{3}{2R_{13}^2}$$

$$N = \frac{3}{2R_{12}^2}$$

The parameters F, G, H, L, M, and N can further be defined as a function of R_{ij} where R_{11}, R_{22}, R_{33} denote the anisotropic yield stress ratios in circumferential, meridional, and through-thickness directions, respectively. The R_{12}, R_{23}, and R_{31} are their respective shear components [55]. Table 3.3. summarizes the coefficients of the Hill 48 yield criteria. These quantities can be calculated from the Lankford coefficients r_0, r_{45}, and r_{90} which are the ratio of in-plane strain and through-thickness strain as given in Equation (3.7) [55].

$$R_{11} = 1$$

$$R_{22} = \sqrt{\frac{r_{90}(r_0 + 1)}{r_0(r_{90} + 1)}}$$

$$R_{33} = \sqrt{\frac{r_{90}(r_0 + 1)}{(r_0 + r_{90})}} \tag{3.7}$$

$$R_{12} = \sqrt{\frac{3(r_0 + 1)r_{90}}{(2r_{45} + 1)(r_0 + r_{90})}}$$

The Lankford coefficients of the sheet were determined after conducting tensile tests for the 0º, 45º, and 90º directions with respect to the rolling direction of the sheet. The ratio of the in-

plane strain to the through-thickness strain was calculated where it resulted in the r_0=0.7244, r_{45}=0.4327, and r_{90}=0.9364.

Table 3.3 Anisotropy coefficients for the Hill '48 model

F	G	H	N	L	M
0.4486	0.5799	0.4201	0.9700	-	-

Finally, Barlat Yld2004-18p was utilized along with isotropic hardening to see the effect of anisotropy described by a full 3D stress state. Equation (3.8) describes the yield function, which is the linear combination of two stress deviators where

$$
\begin{aligned}
\varphi = \varphi(\overline{S'}, \overline{S''}) &= \left|\tilde{S}'_1 - \tilde{S}''_1\right|^a + \left|\tilde{S}'_1 - \tilde{S}''_2\right|^a + \left|\tilde{S}'_1 - \tilde{S}''_3\right|^a + \left|\tilde{S}'_2 - \tilde{S}''_1\right|^a \\
&+ \left|\tilde{S}'_2 - \tilde{S}''_2\right|^a + \left|\tilde{S}'_2 - \tilde{S}''_3\right|^a + \left|\tilde{S}'_3 - \tilde{S}''_1\right|^a + \left|\tilde{S}'_3 - \tilde{S}''_2\right|^a + \left|\tilde{S}'_3 - \tilde{S}''_3\right|^a = 4\bar{\sigma}^a
\end{aligned}
\tag{3.8}
$$

$$
\begin{aligned}
\tilde{\mathbf{s}}' &= \mathbf{C}'\mathbf{s} = \mathbf{L}'\boldsymbol{\sigma} \\
\tilde{\mathbf{s}}'' &= \mathbf{C}''\mathbf{s} = \mathbf{L}''\boldsymbol{\sigma}
\end{aligned}
\tag{3.9}
$$

a=8, $\bar{\sigma}$ is the flow stress, $\tilde{S}'_i$ and $\tilde{S}''_j$ are principal values of the tensor $\tilde{\mathbf{s}}'$ and $\tilde{\mathbf{s}}''$ which are defined by the two linear transformations on the stress deviator $\mathbf{s}$. The coefficients of $\mathbf{C}'$, $\mathbf{C}''$ are taken from the work of Esmaeilpour et al. [44]. In the work, CPFEM is utilized to conduct virtual experiments to account for the out-of-plane coefficient of the material, which is difficult for sheet metal forming that is not considered in the other yield functions.

Table 3.4 Coefficients for Yld 2004-18p

c'_{12}	c'_{13}	c'_{21}	c'_{23}	c'_{31}	c'_{32}	c'_{44}	c'_{55}	c'_{66}
0.8440	1.2864	1.2398	1.3860	1.3214	1.4549	0.9374	0.8194	1.2077
c''_{12}	c''_{13}	c''_{21}	c''_{23}	c''_{31}	c''_{32}	c''_{44}	c''_{55}	c''_{66}
0.8341	1.0716	0.8122	0.6433	0.4379	0.3502	0.9940	1.0418	0.7782

3.3.4. Element formulation and element size

The meshing scheme significantly impacts the model's accuracy, the convergence of the integration scheme, and the computational cost. The simulation's overall computational cost generally depends on the number of elements and the total simulation time. It is one of the goals of the FEM model to optimize the computational cost such that the overall computation can be done in an acceptable time. The simulation time in incremental forming is generally long. Thus, the incremental forming models can be very computationally heavy. Since the total simulation time is a fixed quantity and generally impossible to change unless using time scaling, it is important to choose the mesh size for the parts such that it has an acceptable computation while retaining good accuracy.
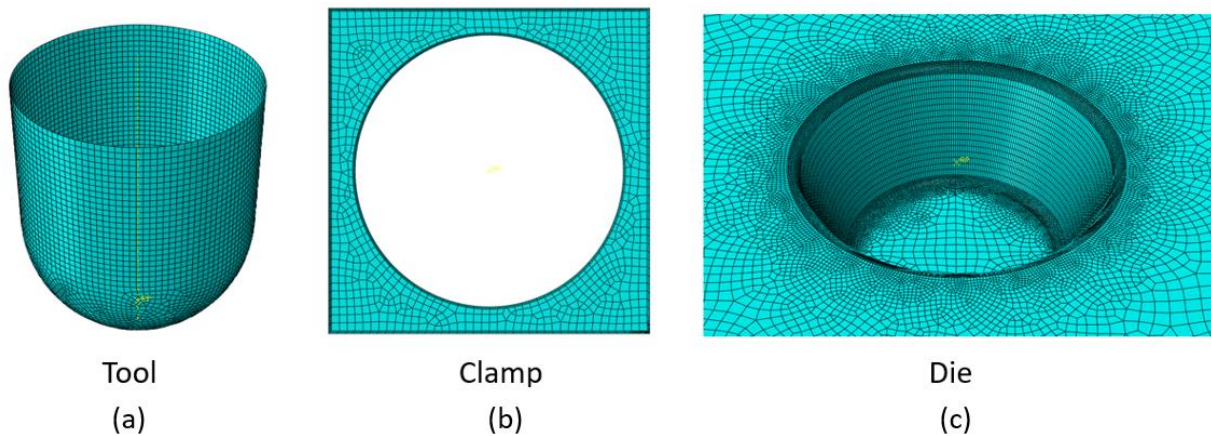
Tool	Clamp	Die
(a)	(b)	(c)

Figure 3.11 Detailed description of meshing of the rigid components: (a) tool, (b) clamp, and (c) die

The top/bottom clamp, die, and the tool is meshed using R3D4 rigid elements. The tool and the die are meshed sufficiently small to avoid any elements in the sheet getting caught by the rigid elements they contact. For axisymmetric parts such as cones and pyramids, an axisymmetric circular scheme was chosen to smoothly express the curvature of the part. Figure 3.11 shows the meshing scheme of the sheet for a cone model. The number of elements in the radial and circumferential direction was chosen to be less than or equal to 0.5 mm. This particular threshold

value was chosen because the value represents around 10% of the tool's radius and goes along with the step size of 0.5 mm is utilized during forming. Having the mesh size be similar to or smaller to step size allows the element to situate themselves at the exact spot when it comes into contact with the tool. This choice of element size ensures both accuracy and convergence.
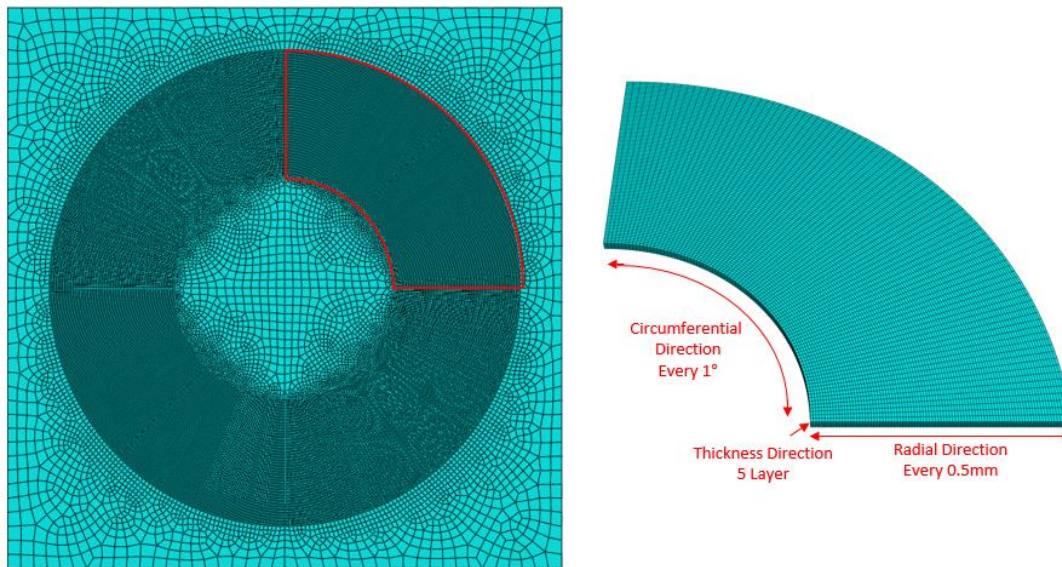
Figure 3.12 Detailed meshing scheme for the sheet in the cone model

The heart and the cover sheet are meshed with square grid mesh. The heart has a 1mm×1mm element with three layers in the thickness direction, while the cover has the 0.5mm×0.5mm element with three layers in the thickness direction. The mesh size in the heart is chosen to be 1mm×1mm because using 0.5mm×0.5mm would result in the number of the element becoming too big and the computation time getting out of control. A compromise had to be made to reduce the computation time while losing accuracy.
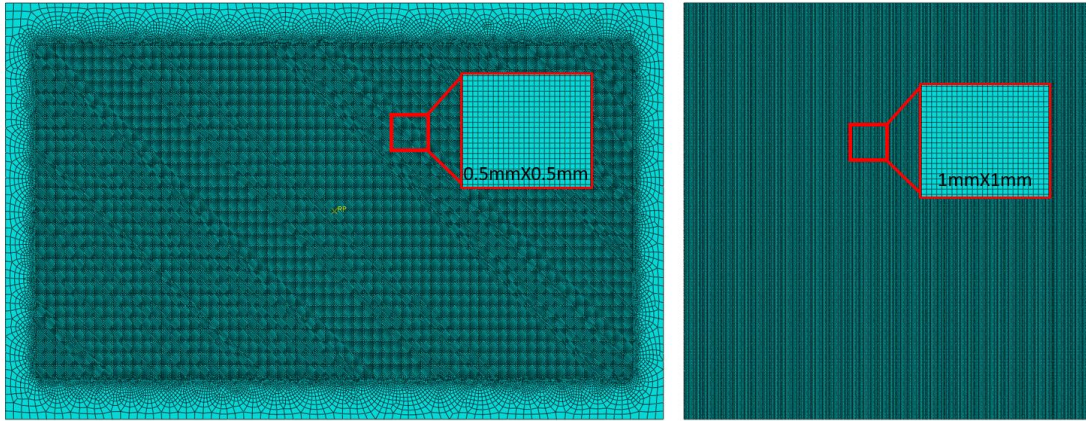
Figure 3.13 Detailed meshing scheme for the sheet in the cover model

Table 3.5 Benchmark study with the varying number of elements in the thickness and with a different mass scaling factor

	Model1	Model2	Model3
No. of Element in Thickness	5	7	5
Mass Scaling Factor	10^7	10^7	10^6
Total No. of Element	223285	312599	223285
Computational Time	29hours	39hours	87hours

The benchmark study was conducted to come up with the default value for the number of elements in the thickness direction. This work was conducted by collaborative research between the University of Michigan, Northwestern University, and Ohio State University. The default number of elements in the thickness direction was chosen to be five. In the study, 3, 5, and 7 elements are used in the thickness direction. An odd number was chosen such that the middle element would serve as the point of reference. Three cases with two different numbers of elements

41

in the through-thickness direction were investigated. The details of the parameters and the computational cost are described in Table 3.5. The resulting strain data were analyzed, and the thickness distribution plotted, as shown in Figure 3.14. It can be seen that five layers are sufficient to capture the thinning during the incremental forming process.
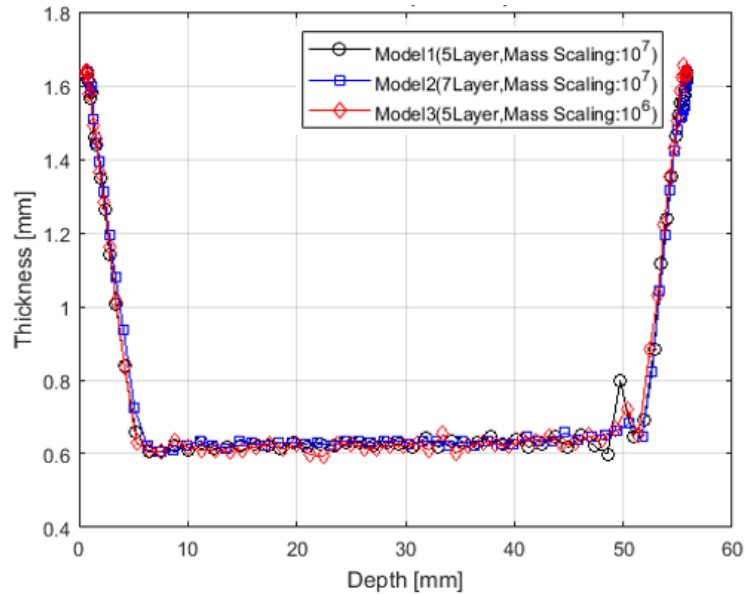
Figure 3.14 Thickness distribution comparison between Model1, Model2, and Model3

3.3.5. Contact formulation and friction coefficient

The contact between the sheet and the tool plays a vital role in the deformation of incremental forming. The most widely used contact algorithms provided in the FEM software are node to surface contact and surface to surface contact. Node to surface contact is when nodes on the master surface interact with the surface of the slave surface. Surface to surface contact utilizes a discretization method to enforce each contact. The discretization method can avoid some of the problems that can arise from the incorrect use of node to surface contact.

In most cases, FEM software requires the user to define the contact pairs. If two surfaces do not have contact defined between them and they come together, one surface will simply penetrate the other, disregarding that surface. In this study, a contact algorithm called general contact is used, a user-friendly version of the surface-to-surface contact developed by Abaqus. This function can let the Abaqus software detect any surface that is in contact and apply the surface to surface contact.

Once the contact algorithm is selected, the contact property has to be defined. The contact property includes tangential and normal behavior between the contact pairs. For tangential behavior, the penalty method is used. The penalty method utilizes the stiffness method, which permits the relative motion of the surfaces. The magnitude of sliding is defined by the frictional behavior where the Coulomb friction coefficient is utilized. For normal behavior, hard contact is used for pressure-overclosure. The hard contact minimizes the penetration of the slave surface into the master surface at the constraint location. It does not allow the transfer of the tensile stress across the interface. A separate case study has been conducted with various friction coefficients in the model to see the effect of the friction coefficient on the resultant forces.

The resultant force consists of tangential(In-plane) and axial force representing the frictional force and forming force. The frictional force is a force that develops due to friction. Thus, the higher the frictional between the sheet and the tool would result in the higher the frictional force. The forming force is a force that is purely required to form the sheet and independent from the frictional effects. As seen from Figure 3.15, the friction coefficient does not influence the forming force in incremental forming. However, the friction coefficient influences the in-plane force. As the friction coefficient values increases, so did the in-plane force. The friction coefficient between the values 0.01 – 0.1 resulted in less than a 10% difference in the tangential force. For

this model, a value of 0.1 was used, which seems to reflect the experimental condition and the measured force values.
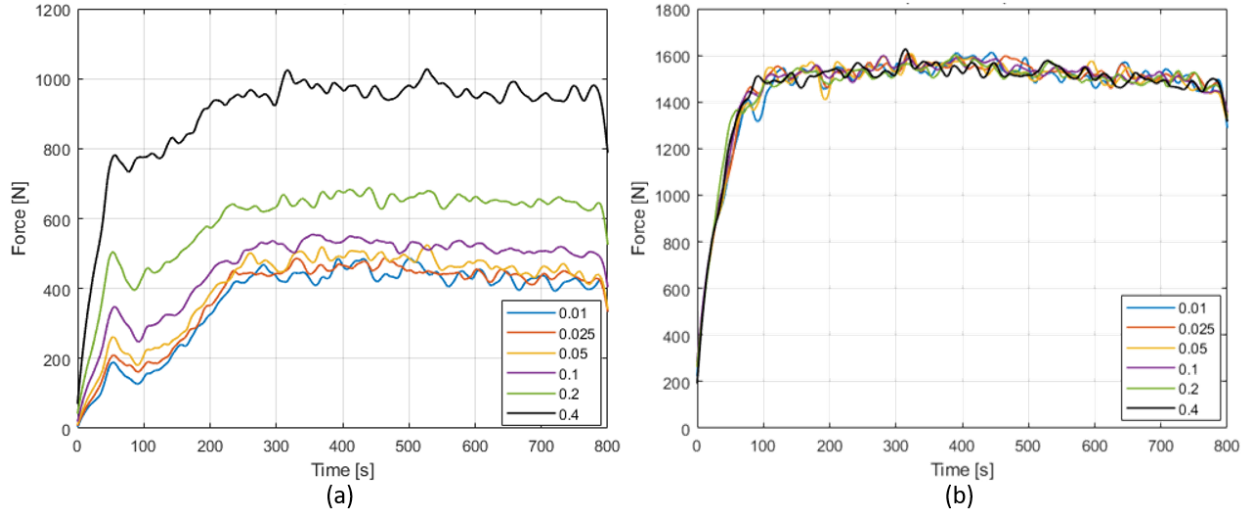
Figure 3.15 (a) In-plane force and (b) axial force calculated for the various friction coefficient

3.3.6. Scaling factors

The scaling factors play an important role in optimizing the computational cost of a FEM model. The computational cost is proportional to the total model time length and proportional to the inverse of the time increment. The time increment is calculated as follows, as shown in Equation (3.10)

$$\frac{T}{n} = \Delta t = L_c \sqrt{\frac{\rho}{E}} \tag{3.10}$$

where T is the total time, Δt the time increment, n number of time increment, ρ density, L_c characteristic length, and E the young's modulus. Mass scaling involves artificially increasing the density to increase the minimum time increment. For a quasi-static problem, mass scaling can significantly benefit computational cost but with small errors in the calculation. On the other hand, the velocity scaling is artificially increasing the tool speed to shorten the total simulation time. Velocity scaling will have a similar effect to mass scaling as long as no rate-dependent inputs are

used. Since both scaling artificially alters the internal quantities that affect the kinetic energy, the user must be cautious in using these numerical manipulations. Normally, a sanity check is conducted to ensure that the model output is accurate. The ratio of kinetic energy to internal energy KE/IE is checked and kept at less than 1% to ensure the model's sanity. In this work, a mass scaling value of 10^7 is used for both cone and heart shape models with no velocity scaling. This value was proven to be effective with minimal artificial errors arising from the scaling.

3.4. Results and discussions

The result of the model with different cases was compared and validated with the experimental data. The main focus of validation is the forming force and the geometry after forming. The part is manufactured using a SPIF or a TPIF process using the experimental setup described in section 3.2.2.

3.4.1. Geometry and thickness comparison for model validation

The geometry profile and the thickness profile of each of the modeled cases were compared with the experiment. The experimental profiles were taken using the laser scanner, Romer Absolute Arm with Integrated Scanner 7525SI, which outputs the point cloud data. A post-processing program is utilized to convert the point cloud data into a profile, which is then used to calculate the thickness distribution. The work focuses on understanding the influence of the material model. Two different hardening functions in combination with three different yield function was investigated. This section aims to understand how the material model influences the accuracy of the prediction and quantifies the prediction errors.

SPIF 67° cone
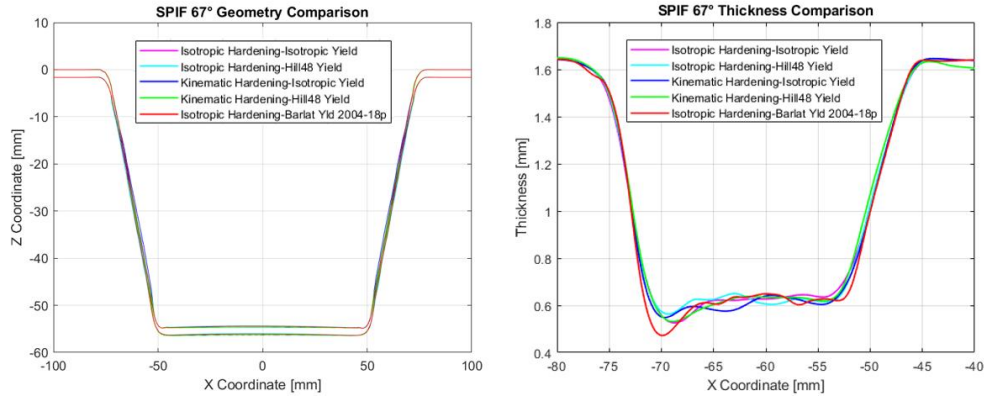
Figure 3.16 Comparison of the geometry and thickness for SPIF 67° cone

TPIF 67° cone
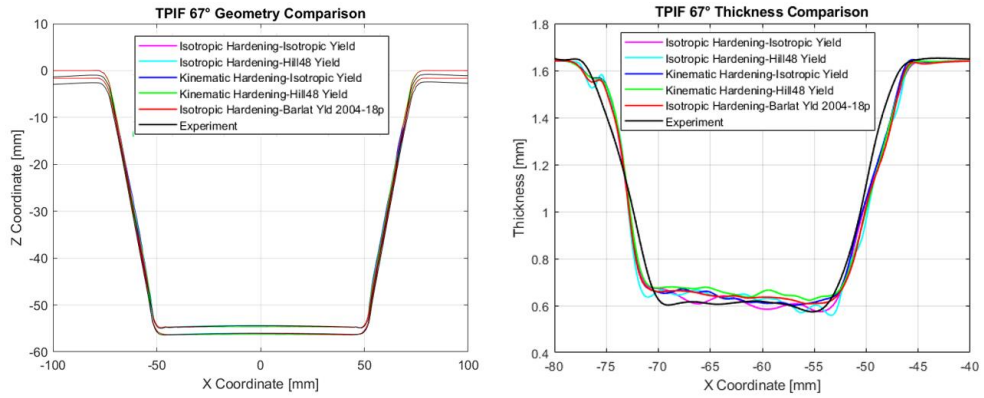
Figure 3.17 Comparison of the geometry and thickness for TPIF 67° cone

SPIF 45° cone
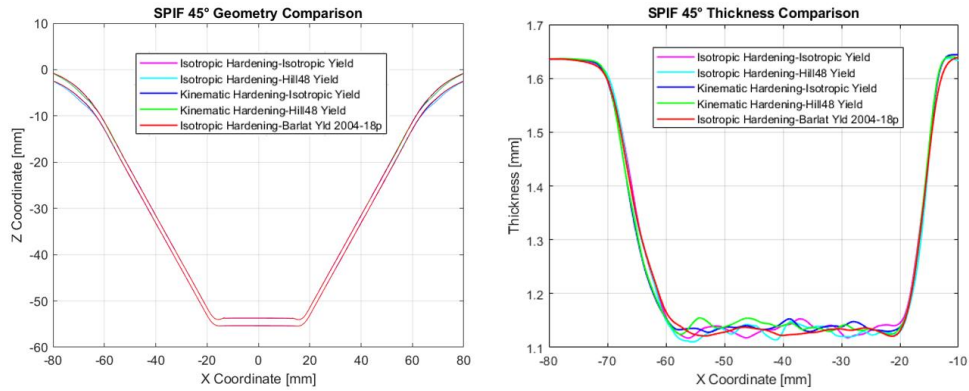
Figure 3.18 Comparison of the geometry and thickness for SPIF 45° cone

TPIF 45° cone
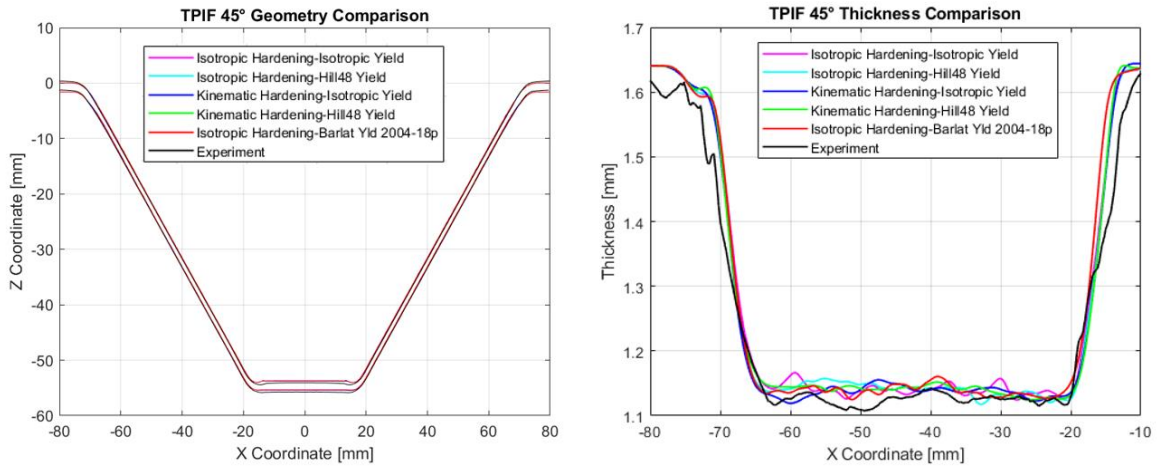
Figure 3.19 Comparison of the geometry and thickness for TPIF 45° cone

Heart
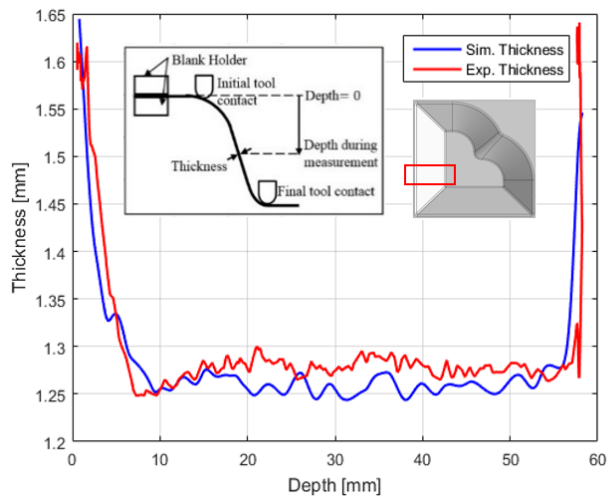
Figure 3.20 Comparison of the thickness for TPIF heart

Cover
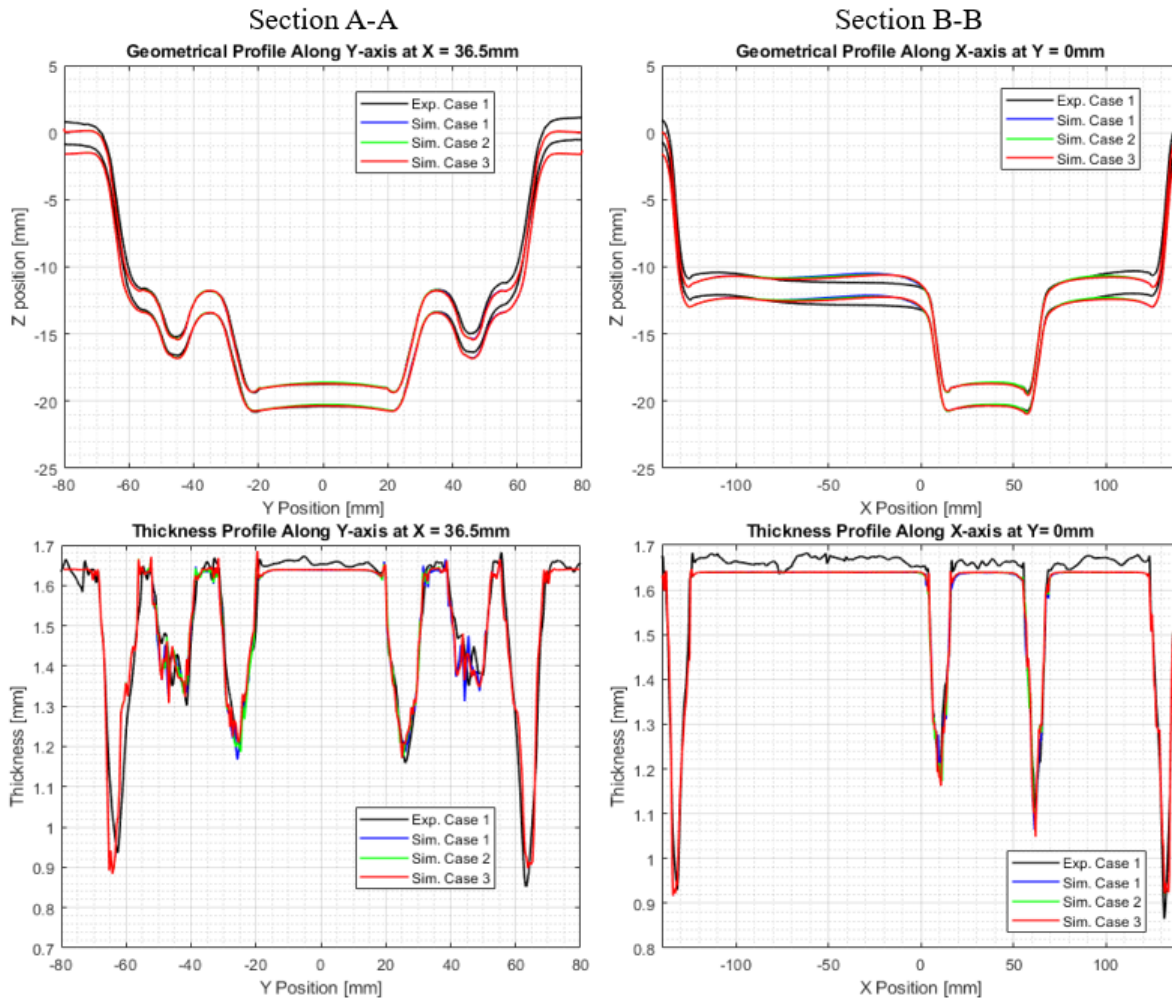
Figure 3.21 Comparison of the geometry and thickness for TPIF cover in section A-A and section B-B

The thickness distributions are generally in good accordance with each other regardless of the combination of the yield function and hardening law. This similarity in geometry maybe because the tool movement is controlled via displacement control. Since the tool is rigid, it would induce a similar strain while generating respective stress components within the element based on the utilized material model. This difference would be reflected in the forming force.

The profile of the cover part had some differences in the flange section. This difference is because of the difference in the boundary condition. The clamps are situated further out in the

experiment than in the model to reduce computation cost by reducing the number of elements. This difference in boundary condition allows some bending and springback in the region near the clamp, resulting in the difference in the profile in the flange section.

3.4.2. Force comparison for model validation

The force in the in-plane radial direction and the z-direction (vertical) were compared with the experiment. The in-plane force is a square root of the x and y direction in the machine/model coordinate system, which considers the force required to form in the radial direction. This force component can be influenced by the friction coefficient, as discussed in section 3.4.3. The vertical force is the remaining z-direction, which is required to form the part in the depth direction.

SPIF 67° cone
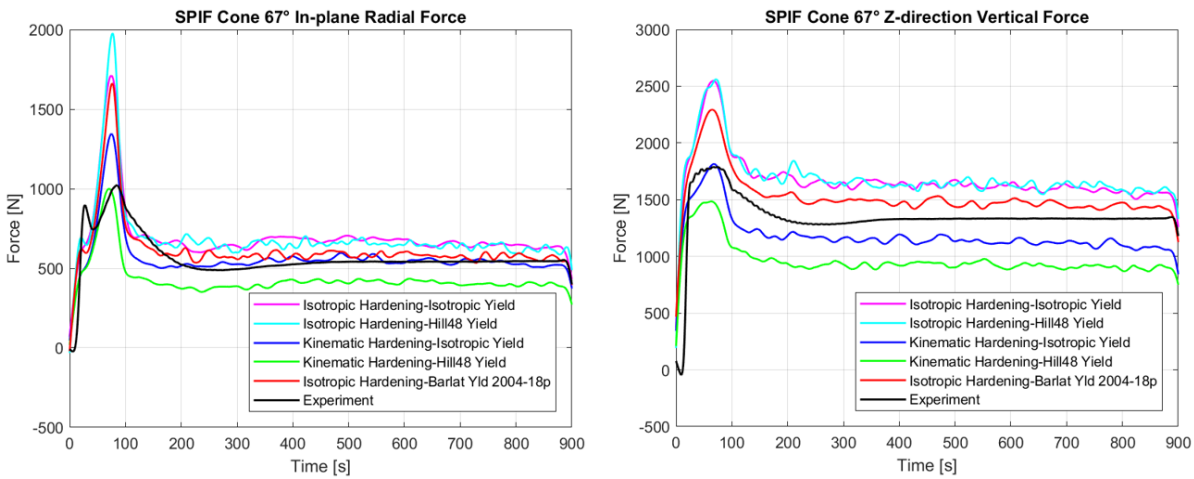
Figure 3.22 Comparison of the force components for SPIF 67° cone

TPIF 67° cone
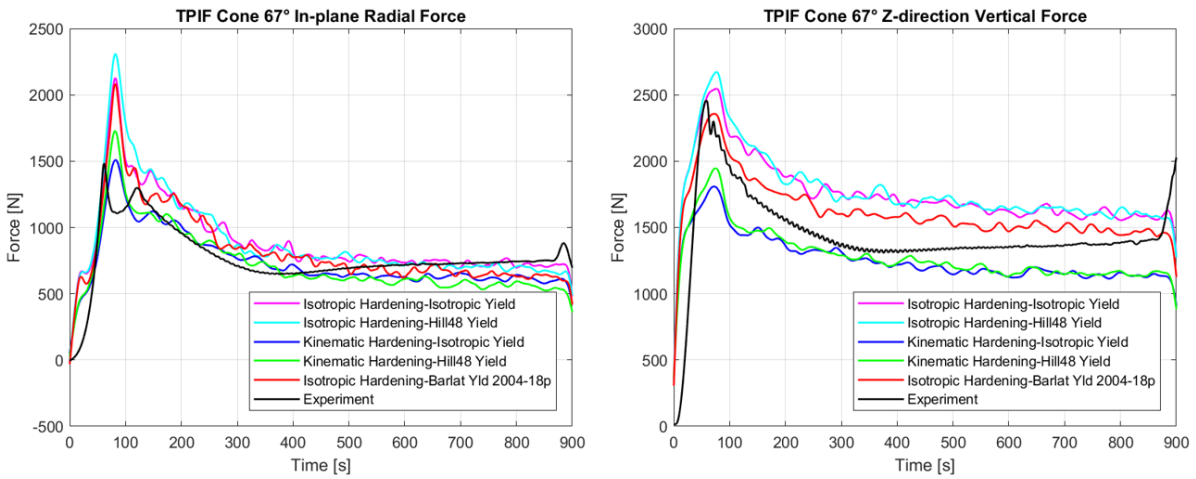
Figure 3.23 Comparison of the force components for TPIF 67° cone

SPIF 45° cone
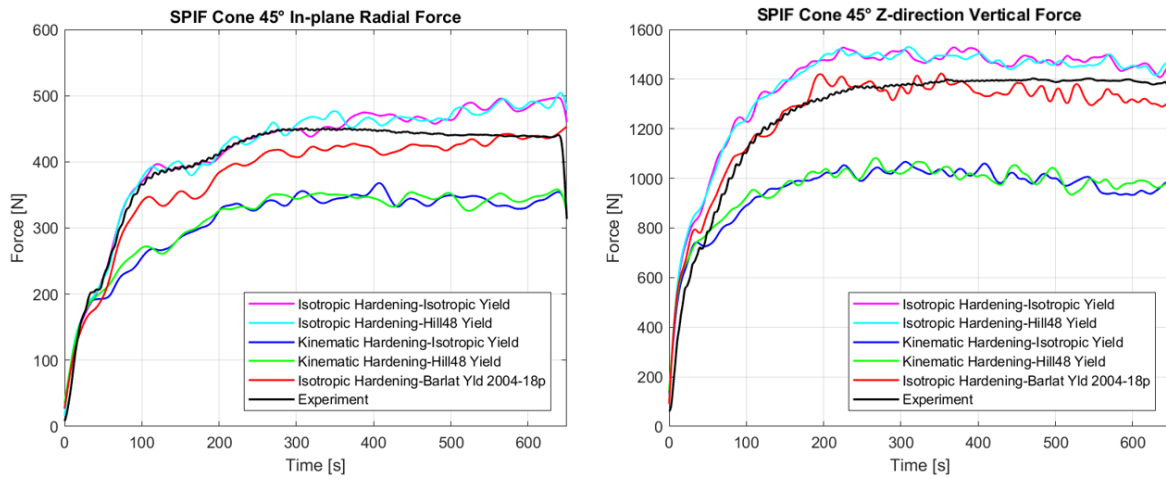
Figure 3.24 Comparison of the force components for SPIF 45° cone

TPIF 45° cone
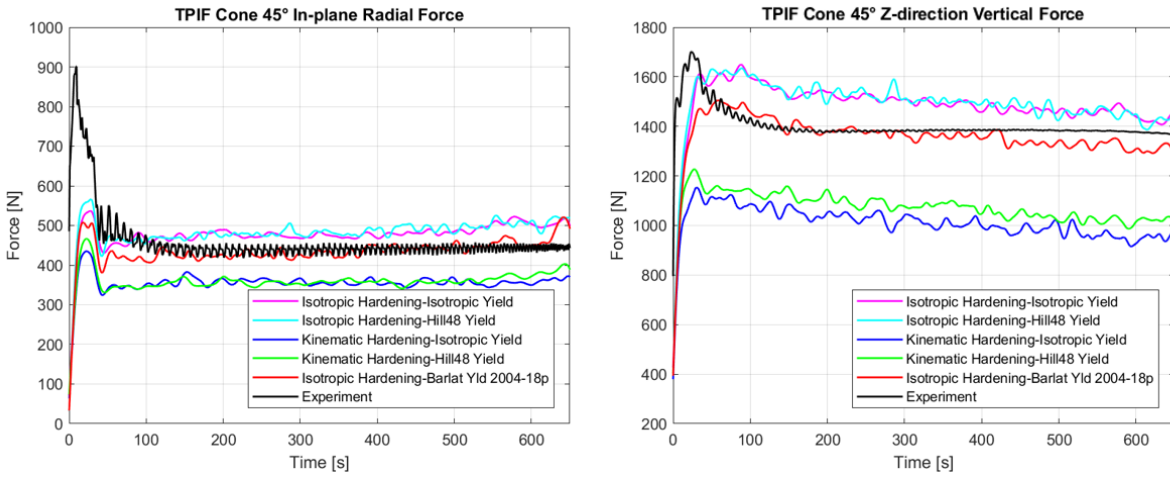
Figure 3.25 Comparison of the force components for TPIF 45° cone

Boeing Heart Shape
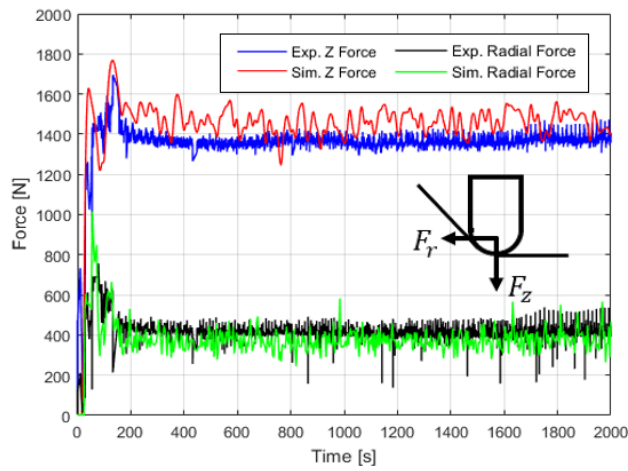
Figure 3.26 Comparison of the force components for TPIF heart

Boeing Fuel Cover
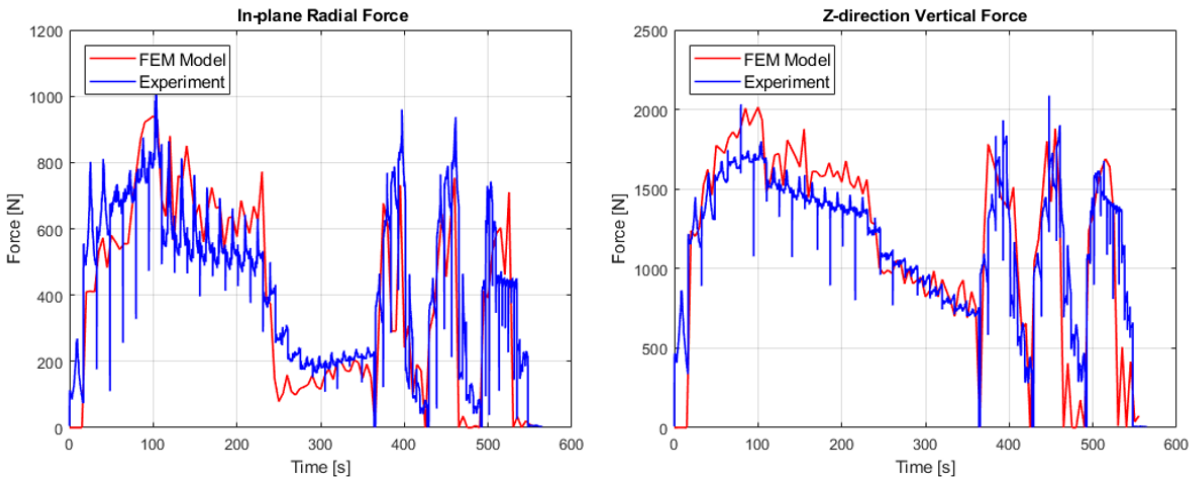
Figure 3.27 Comparison of the force components for TPIF cover

It can be seen that different combinations of hardening law and yield function results in different amounts of errors in terms of predicting the forces. The difference between the experimental forces and the predicted forces has been measured in the steady-state region. The corresponding errors of the force prediction have been calculated for each of the cone cases. The detailed values are found in Table 3.6. The first abbreviation in the hardening law-yield function section denotes the hardening law, and the second denotes the yield function. Iso, Kin, Hill, and Barlat each stand for Isotropic hardening/yield, Kinematic hardening, Hill48 anisotropic yield function, and Barlat Yld 2004-18p.

3.4.3. Error analysis and impact of the material model on the accuracy of the prediction

Comparing the geometry and thickness showed that various material models had minimal impact on the geometric prediction. However, the impact of the various material model on force prediction was significant. Understanding the effect of material models was difficult with analyzing the graphs since it was challenging to quantitatively compare each of the cases. Thus, the force prediction error based on each of the input material models was calculated to quantify

the material model's effect on the prediction results. The summary of the results is presented in Table 3.6. The mean error in the steady-state region was calculated for each part. This region was chosen is because the steady-state region is where most of the deformation is taking place, away from the transient end effects. Finally, a bar plot containing each geometry and model deviation was plotted, which provided explicit comparison.

It can be seen that kinematic hardening-based models severely underpredict the force for all of the cases. This underprediction indicates that kinematic hardening does not represent the deformation mechanism occurring in the incremental forming process. It can be seen that the conventional simple model of isotropic yield criteria with isotropic hardening based on tensile-based curve give fair force prediction with around 10% error for the SPIF parts for both 45° and 67° wall angle. However, for the TPIF part, it can be seen that simple models with isotropic yield and hardening are not sufficient for force prediction and especially the z-direction force is severely over predicted. The difference between SPIF and TPIF is that there is a die for the TPIF process. This die provides additional support for more accurate geometry. However, the die's presence seems to make the stress state more complicated, inducing more deviation from the isotropic yield locus and ultimately more deviation in the forming forces. It can be seen that the simple material model is not capable of accurately describing the additional complication that the die brings. The model using Barlat 2004-18p was able to capture both force components for all cases with less and 10% accuracy, which proved to be the most accurate model of all.

One observation of using the Barlat type yield function was that it lowered the vertical force prediction. The Barlat model has a lower vertical force compared to the isotropic yield and hardening model. This observation was witnessed in all cases utilizing the Barlat model since the Barlat model is an add-on to its isotropic counterpart. This phenomenon can be explained by

comparing the yield locus of the Barlat 2004-18p to the isotropic yield locus. It can be assumed that the Barlat yield locus is closer to the actual yield locus of the material than the isotropic yield locus because more material experiments were conducted to derive the locus. Suppose the stress state developed during incremental forming corresponds to a particular point in the yield locus where the difference between the Barlat curve and von Mises curve is great. It will result in a greater deviation in the forces as we observed in the predictions, explaining the Barlat model's more accurate prediction. Since the Barlat yield locus is smaller in those regions, it results in a lower force prediction leading to a decrease in the vertical force. The yield locus's difference seems to be due to Barlat Yld 2004-18p being calibrated for the out-of-plane components while the other yield functions were not. The isolation of the effect of out-of-plane components is required as future work. However, this can also open up the possibility of calibrating the isotropic yield locus to match those points in the yield locus, which greatly influences the forming force to enhance the isotropic yield model's prediction accuracy.

Table 3.6 Percentage of errors found in the force prediction for each of the cases

	Hardening Law-Yield Function	SPIF 45° (%)	TPIF 45° (%)	SPIF 67° (%)	TPIF 67° (%)	Average (%)
In-Plane Radial Force	Iso-Iso	5.05	5.87	28.38	3.89	10.80
	Iso-Hill	4.24	9.91	20.95	-3.71	7.85
	Kin-Iso	-21.06	-20.74	5.04	-13.46	-12.55
	Kin-Hill	-23.92	-18.65	-22.06	-24.50	-22.28
	Iso-Barlat	-4.33	-0.23	7.43	-6.67	-0.95
Z-Direction Vertical Force	Iso-Iso	6.18	7.38	22.58	13.28	12.35
	Iso-Hill	4.38	8.32	19.73	17.42	12.46
	Kin-Iso	-28.45	-21.84	-16.35	-18.72	-21.34
	Kin-Hill	-26.87	-27.62	-31.73	-16.26	-25.62
	Iso-Barlat	-3.52	-1.81	7.43	5.73	1.96

From the error analysis, it can be concluded that using a fixed combination of hardening function and yield function would result in a similar value of error regardless of the geometry. This observation indicates that there could be a constant offset of errors in the prediction of forces when a particular set of hardening and yield functions is used. The combination of isotropic hardening and the Barlat yield function does result in the minimum amount of error. However, it is challenging and expensive to conduct tests required to establish the yield function parameters. Thus, once the deviation for each of the material models is established, it is possible to simulate with the most basic yield function and hardening law offset the result to obtain the prediction close to the actual value based on the observation above.
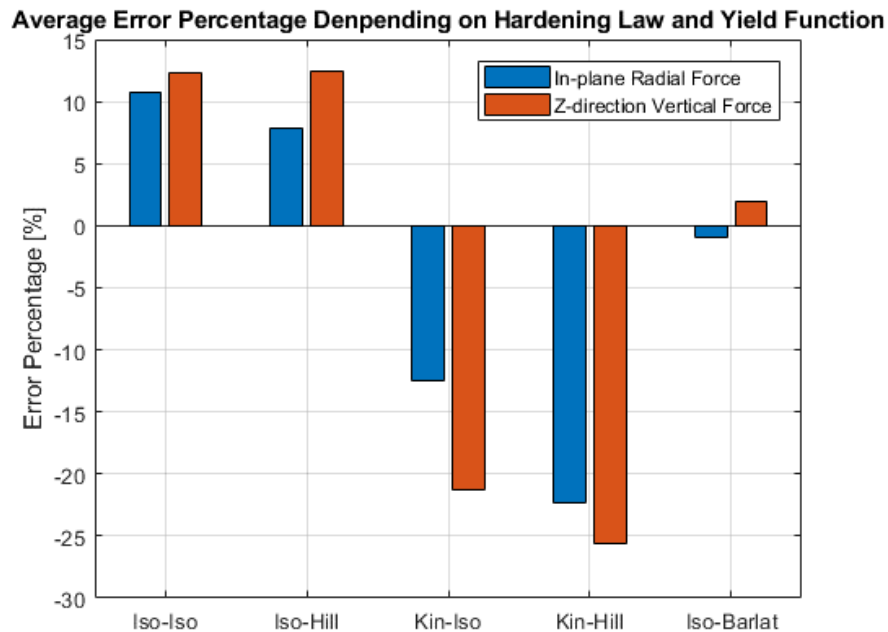
Figure 3.28 Comparison of the average error percentage for a different combination of hardening law and yield function

3.4.4. Process parameter recommendation for incremental forming

There is no single right answer to the choice of process parameters that lead to a successful result. Various combinations of process parameters can result in a successful outcome for a given

part. However, the process parameters have to be chosen carefully to achieve precision and to meet the quality standards. While the general trend of how each process parameter impacts the formability and precision has been investigated, it is difficult to establish a set of process parameters that may work robustly with that information alone. Thus, it is necessary to establish a guideline for the range of values for the process parameter that would generally result in a successful forming operation.

The parameter found in ISF has been categorized into thee categories, the process parameters that are common in both experiment and model, the experimental parameters and model parameter. While it is possible to connect the experiment with the forming result directly, it is possible to understand what interaction of the process parameters and understand the underlying mechanism by introducing the model. Also, it is possible to use the model to simulate various cases with different combinations of process parameters which would be difficult to do in the experiment.

The forming result/prediction is divided into three categories, the deformation at the wall, the deformation at the undeformed region, and the forming force. These three categories can be used as the criteria in assessing whether the choice of process parameter is appropriate. Most important is the deformation in the wall and the deformation in the undeformed region since it directly correlates to the formability of the material. If the forming operation cannot achieve the desired result in these regions, one can say that part has failed. As seen in Figure 3.3, it can be seen that the deformation in the wall is influenced by the tool path, which is created from the process parameters the radius r, thickness t, wall angle θ, and the step-down Δz. The deformation in the undeformed region, which can be indicated as the amount of bulge, is influenced by the step-down Δz, and the squeeze factor α. Tables 3.7 - 3.11 show the detailed value of process parameters

utilized in the forming process. The ISF variant indicates whether SPIF or TPIF is used, while geometry indicates what part is manufactured. The tool diameter, thickness, step size, and squeeze factor are explained in the previous section. The feed rate is the speed at which the tool travels. While most of the tests were conducted at 100in/min, 25 and 50 in/min were also used. The r/t ratio is a value established based on the ratio of tool radius to sheet thickness. The highlighted lines indicate the part that has resulted in a failure. The failure could be either failure in the wall or failure due to a severe bulge development. The value of programmed squeeze factor of 5%, 10%, 15% and 20% which corresponds to effective squeeze factor value of roughly 0.5%, 1%, 3%, and 6% for the step down of 0.5mm. For other step-down value cases, the programmed squeeze factor will correspond to similar effective squeeze factor values, although the exact values may differ.

Table 3.7 List of the investigated combination of process parameter for SPIF

ISF Variant	Geometry	Tool Diameter (mm)	Thickness (mm)	Step Size (mm)	Feed Rate (in/min)	Programmed Squeeze (%)	Tool radius/ Thickness (r/t)	Failure
SPIF	45	8	1.64	0.5	100	0	2.44	N
SPIF	67	8	1.64	0.5	100	0	2.44	N
SPIF	45	12.5	1.64	0.5	100	0	3.81	N
SPIF	67	12.5	1.64	0.5	100	0	3.81	N
SPIF	Funnel (30~67)	12.5	1.64	0.5	100	0	3.81	N

Table 3.8 List of the investigated combination of process parameter for TPIF 67°

ISF Variant	Geometry	Tool Diameter (mm)	Thickness (mm)	Step Size (mm)	Feed Rate (in/min)	Programmed Squeeze (%)	Tool radius/ Thickness (r/t)	Failure
TPIF	67	8	1.64	0.5	50	0	2.44	N
TPIF	67	8	1.64	0.5	50	10	2.44	N
TPIF	67	8	1.64	0.5	50	0	2.44	Y
TPIF	67	8	1.64	0.5	25	0	2.44	N
TPIF	67	8	1.64	0.5	25	0	2.44	N
TPIF	67	8	1.64	0.5	50	10	2.44	Y
TPIF	67	8	1.64	0.5	50	0	2.44	Y
TPIF	67	8	1.64	0.5	25	20	2.44	N
TPIF	67	8	1.64	0.5	25	30	2.44	N
TPIF	67	8	1.64	0.5	25	40	2.44	N

TPIF	67	8	1.64	0.5	100	30	2.44	Y
TPIF	67	8	1.64	0.5	50	30	2.44	N
TPIF	67	8	1.64	0.5	50	30	2.44	N
TPIF	67	8	1.64	0.5	25	20	2.44	N
TPIF	67	8	1.64	0.5	25	10	2.44	N
TPIF	67	8	1.64	0.5	75	30	2.44	N
TPIF	67	8	1.64	0.5	25	0	2.44	N
TPIF	67	8	1.64	0.5	25	40	2.44	Y
TPIF	67	8	1.64	0.5	25	40	2.44	N

Table 3.9 List of the investigated combination of process parameter for TPIF 45°

ISF Variant	Geometry	Tool Diameter (mm)	Thickness (mm)	Step Size (mm)	Feed Rate (in/min)	Programmed Squeeze (%)	Tool radius/ Thickness (r/t)	Failure
TPIF	45	8	1.64	0.5	100	0	2.4390	N
TPIF	45	8	1.64	0.5	100	10	2.4390	N
TPIF	45	8	1.64	0.5	100	20	2.4390	N
TPIF	45	8	1.64	0.1	100	10	2.4390	N
TPIF	45	8	1.64	0.2	100	10	2.4390	N
TPIF	45	8	1.64	0.1	100	10	2.4390	N
TPIF	45	12.7	1.64	0.5	100	0	3.8720	N

Table 3.10 List of the investigated combination of process parameter for TPIF Heart

ISF Variant	Geometry	Tool Diameter (mm)	Thickness (mm)	Step Size (mm)	Feed Rate (in/min)	Programmed Squeeze (%)	Tool radius/ Thickness (r/t)	Failure
TPIF	Heart	8	1.64	0.25	100	0	2.4390	Y
TPIF	Heart	8	1.64	0.25	100	5	2.4390	Y
TPIF	Heart	8	1.64	0.25	100	10	2.4390	Y
TPIF	Heart	8	1.64	0.5	100	5	2.4390	N
TPIF	Heart	8	1.64	0.5	100	10	2.4390	N
TPIF	Heart	8	1.64	0.5	100	15	2.4390	N
TPIF	Heart	8	1.64	0.63	100	5	2.4390	N
TPIF	Heart	8	1.64	0.63	100	10	2.4390	N
TPIF	Heart	8	1.64	0.63	100	0	2.4390	N
TPIF	Heart	8	1.64	0.63	100	15	2.4390	N
TPIF	Heart	8	1.64	0.75	100	10	2.4390	Y
TPIF	Heart	8	1.64	0.75	100	15	2.4390	N

Table 3.11 List of the investigated combination of process parameter for TPIF Cover

ISF Variant	Geometry	Tool Diameter (mm)	Thickness (mm)	Step Size (mm)	Feed Rate (in/min)	Programmed Squeeze (%)	r/t	Failure
TPIF	Cover	8	1.64	0.5	100	0	2.4390	N
TPIF	Cover	4	1.64	0.1	100	0	1.2195	Y
TPIF	Cover	4	1.64	0.25	100	0	1.2195	Y
TPIF	Cover	4	0.635	0.25	100	0	3.1496	N

Based on Table 3.7 – 3.11, it is possible to establish the upper bound and lower bound for the experimental process parameters that would result in an acceptable forming operation. Establishing the boundaries for the process parameters lays the foundation for the hypothesis for understanding the material behavior in incremental forming in the later chapters.
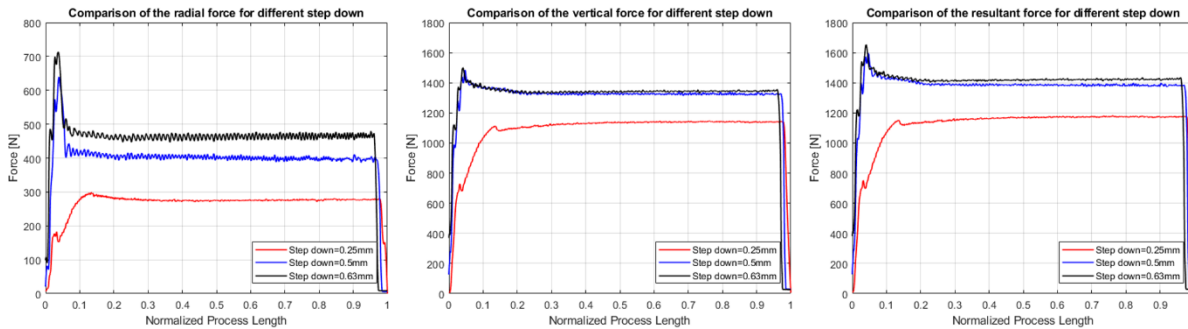
Figure 3.29 Comparison of the forces for different step-down size

Sheet thickness _t_

The sheet thickness should be chosen based on the design criteria for the required section thickness. The undeformed sheet thickness can be back-calculated using the sine law while considering the wall angle.

Radius over thickness _r/t_

The tool radius can be chosen based on the observation of the r/t ratio. It can be observed that there is a threshold value of r/t that has to be exceeded for the part to be formed successfully. The threshold value was found to be around two. As long as the tool radius is chosen so that the r/t ratio exceeds the value of two, it will be sufficient. However, as the tool radius becomes larger, the forming force increases accordingly since the contact area increases. This increase in the force can result in significant tool deflection and, in some cases, result in a broken tool. Thus the radius

has to be chosen such that the forming force is low enough for the CNC set up to withstand the force.

Wall angle _θ_

The wall angle is a parameter derived from the given part design. It is possible to establish the maximum wall angle that the part can achieve before failure for a given material. A funnel that varies from low wall angle to high wall angle can be manufactured to test the maximum wall angle value. If an arbitrary geometry has a wall angle value that is less than that of the maximum wall angle possible for a given material, in most cases, it will not result in failure of the part.

Step down _Δz_

The step-down size influences both the deformation in the wall and the bulge. It was observed that the higher step-down results in higher formability and better surface quality. However, it results in a higher forming force due to more material contact, as seen in Figure 3.29, where there is an increase in the resultant force as the step-down increases. Thus step-down value has to be chosen to balance the formability and forming force. Generally, it was observed that values close to 10% of the tool's radius result in a good forming result.

Squeeze factor _α_

The squeeze factor is an additional process parameter that can be introduced in the TPIF process. By squeezing the material, more hydrostatic pressure can be generated, resulting in higher formability. However, large squeeze factor values can lead to more material being pushed in the undeformed region, resulting in the bulge and ultimately failure. Thus, a low value of squeeze factor is desired based on whether the geometry exceeds the material's formability.

3.4.5 Uncertainty analysis for experiment and model

For the models to be accurate, validation of the results is important. However, it is crucial that the experimental results that the model results are being compared to have a minimum level of uncertainty for it to be considered an accurate validation. If the experimental uncertainties themselves have high variabilities, the model results validated against these results would not be credible. As this work focuses on developing credible numerical and analytical models, it is crucial to know the uncertainties associated with the experiment and the models.

Table 3.12 shows the experimental and numerical uncertainties found during incremental forming. The main reason for experimental uncertainties rises due to the variability in the material and the variability in the forming setup. In the case of numerical uncertainties, they are brought about by the numerical parameters in the model. These uncertainties can be quantified and compared. The uncertainties for both the experiment and the numerical simulation were calculated for the forming results: geometry measurement, thickness measurement, and force measurement.

Table 3.12 Cause of uncertainties in experimental and numerical simulation for incremental forming

Category	Experimental Uncertainty		Numerical Uncertainty
	Experiment	Measurement	
Source	• Material variability • Rigidity of the setup • Clamping • Friction condition	• Measurement uncertainty • Calibration error	• Mesh sensitivity • Boundary conditions • Scaling factors • Friction and contact
Target	Force measurement Geometry/Thickness measurement		Force prediction Geometry/Thickness prediction
Calculation method	Repeated experiment		Comparison with experiment

The values of the experimental uncertainties for the geometry, thickness, and forces were calculated based on the results of the repeated test for the geometry of cone 67°. The variability

between the parts was measured, and the standard deviation for each of the values was calculated to compute the average variation between the parts. The experimental geometry, thickness, and force uncertainties were 0.0883mm, 0.0139mm, and 28.4899N, respectively. For the model, the geometry, thickness, and force uncertainties were 0.3759mm, 0.0259mm, and 119.6907N, respectively.

Table 3.13 Values for the experimental and numerical uncertainties

	Experiment	Error	Model	Error
Geometry	0.0883 [mm]	0.22%	0.3759 [mm]	0.94%
Thickness	0.0139 [mm]	2.18%	0.0259 [mm]	4.07%
Force	28.4899 [N]	2.33%	119.6907 [N]	9.81%

The model uncertainty ratio to the experimental uncertainty was calculated by setting the experimental uncertainty values as 1 to get the relative comparison, as shown in Figure 3.30. It can be seen that the model uncertainty values are much greater than that of the experiment for all cases by the factor of 4 for force and geometry and 2 for thickness. It can be observed that the experimental uncertainty values are very small, with less than 100microns for the geometry and thickness. The force uncertainty is less than 30N, which is less than 5% of the smallest force component. It can be concluded that the experimental results can serve as validation points for the model with reliability. The work done in this thesis which focuses on minimizing the numerical uncertainty is directly related to enhancing the accuracy of the prediction.
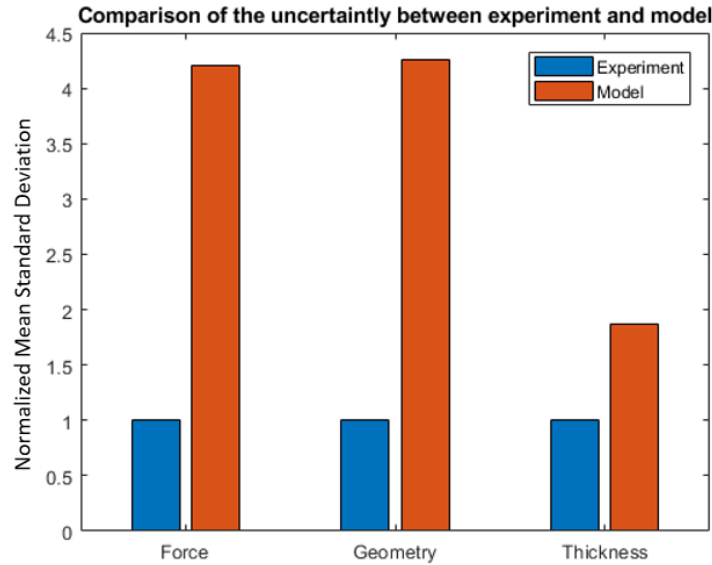
Figure 3.30 Comparison of the experimental and numerical uncertainty by normalizing the experimental uncertainty as one and calculating the ratio

The industry standard on geometry and thickness tolerance for aluminum 7075 is established by Aluminum Association. Based on the spec sheet provided by Tenneco and Boeing, the geometry and thickness tolerances are ± 0.5mm and ± 0.0762mm for sheet thickness of 1.63mm, respectively. As seen in Table 3.13, the variability found in the experiment and in the model is within limits of the tolerance standard practiced by the industry. This proves that the incremental forming setup and the model established at the University of Michigan is capable of manufacturing and predicting incremental forming parts with repeatability and reliability. The variability of the force is not compared since the force values are unique for processes with different input parameters and ultimately is coupled to geometry and thickness result.

3.4.6. Complexity, cost, accuracy analysis for finite element models

The knowledge of the model's cost and complexity, along with the accuracy of the model, provides a valuable understanding of choosing which parameters to use for a given part and constraints. The cost and complexity of various numerical models and their expected accuracy are

compared between the models with different input numerical parameters and geometry to give a quantitative evaluation of each model.

Separate functions calculate the cost and the complexity of the models. The parameters that influence the cost and the complexity of the model were separately identified. The models introduced in this chapter are utilized to demonstrate the effectiveness of the cost and complexity function and plotted on a single plot displaying its accuracy values.

The components of the cost function N_{cost} include the type and cost of experts needed to create/run the model, the cost of conducting material testing for material characterization and the cost of parallel computing for the models. The components of the complexity function $M_{complexity}$ are defined based on the components that require calibration in the numerical model. These are the number of parts and features in the geometry, the number of material parameters, the complexity associated with assembly, the complexity associated with time increment and scaling factor, the contact formulation and boundary condition, the tool path generation and implementation, and meshing. These values are stored in the vector as shown in Equation (3.11) and Equation (3.12).

To calculate the final value of the cost and complexity, these vectors goes through the weighted summation, which is the dot product between N_{cost} and $M_{complexity}$ and its corresponding weights w_{cost} and $w_{complexity}$, respectively using the Equation (3.13) and (3.14). Finally, the accuracy values calculated in chapter 3 was used to illustrate the expected accuracy of each model.

$$N_{\mathrm{cost}} = [n_1, n_2, n_3] \tag{3.11}$$

$$M_{\mathrm{complexity}} = [m_1, m_2, m_3, m_4, m_5, m_6, m_7] \tag{3.12}$$

$$g(N_{\mathrm{cost}}) = w_{\mathrm{cost}} \cdot N_{\mathrm{cost}} \tag{3.13}$$

$$f(M_{\text{complexity}}) = w_{\text{complexity}} \cdot M_{\text{complexity}} \tag{3.14}$$

Seven cases of models with different input parameters were compared. These cases are the models which were analyzed in detail in chapter 3. Three different geometries, the cone 67°, the heart and the cover was analyzed. The complexity of the geometry increases as the part evolves from cone, which is one single geometry, to the cover, which combines several geometric features. The different combinations of material hardening and yield function were used. The models utilized single hardening law, the isotropic hardening, while different yield functions, isotropic, hill48, and the Barlat 2008-18p, were used. They also increase as you go from the isotropic to Barlet as they require more material parameters and consequently an increased number of tests to calibrate them.

Based on the calculated complexity, cost and accuracy value, the values were plotted on the scatter plot shown in Figure 3.31. The complexity was normalized based on the maximum possible complexity value calculated based on the upper limit of the parameters. While there may be some discrepancy in the cost values from the actual values, it provides a good relative comparison. Given more accurate cost data such as wage and material testing, a more accurate total cost can be calculated.

As seen in Figure 3.31, the cone with the isotropic yield resulted in the lowest complexity and cost as the cone is the simplest geometry and isotropic yield is the simplest to calibrate. The cover models resulted in a generally high cost and complexity as their complex geometry contributes to the difficulty in generating and running the model. The model with barlat 2008-18p resulted in a modest cost even for a simple cone geometry as the cost of material testing and computation exponentially increases as the yield function becomes complex. It can be observed that the accuracy of the model does not necessarily follow the cost. The simple models can still

65

achieve accurate predictions compared to more complicated models. Thus, the right choice of parameters is crucial in getting the optimal prediction accuracy. This work provides a baseline understanding of the relationship between the numerical models' cost, complexity, and accuracy in incremental forming.
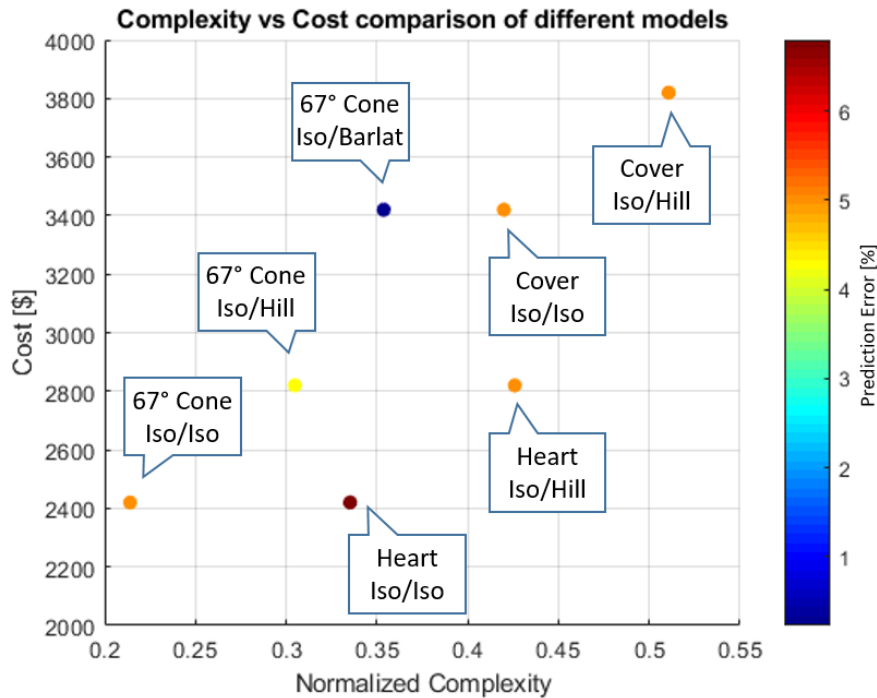
Figure 3.31 The comparison of the cost, complexity and accuracy of different models

3.5. Summary and conclusions

In this research, the finite element model for incremental forming is introduced. The parameters that influence the ISF process were categorized into process parameters, experimental/model parameters. The connections are made between the process parameters, experimental/model parameters, and the forming operation. The goal of the research is to understand the role of each process parameters that influences the forming result, which falls into one of the three categories, the deformation in the region where the tool is in direct contact, the deformation in the region where the tool is not in direct contact, and the forming force. Based on

the connections, a guideline for selecting each of the process parameters is established. The conclusions of the study are as follows:

(1) The connections can be made between the process parameters, experimental/model parameters, and the forming result.

(2) The finite element model was established, and each of the model parameters was analyzed for optimal results.

(3) Among the model parameters, the material model has a major influence on the finite element model result. A simple combination of isotropic hardening and isotropic yield function can result in the prediction of less than 15%. The complicated models of Barlat 2008-18p resulted in the most accurate result. However, since each material model combination results in a fixed amount of offset to the prediction result, complicated material testing may not be necessary to obtain parameters for sophisticated material models. Instead, simple material models can be adopted and the result offset by the known error amount.

(4) With the model parameters established, a different combination of the material models was run to establish the lower and upper bound for the experimental process parameters.

(5) The experimental uncertainties were smaller than the model uncertainties by a factor of four. Both experimental and model uncertainties were within the industry standards.

(6) The cost – complexity – accuracy analysis provides a quantitative evaluation of the cost and complexity associated with various geometry and material models allowing the user to choose the appropriate model.

Chapter 4 Prediction of Defects in Incremental Forming

The defective phenomena found during incremental forming are detrimental to the formed part. These negative impacts can range from simple geometric deviation to localized thinning, leading to weaker sections leading to failure. The defective phenomena found in incremental forming are the thinning/necking of the wall, the formation of the bulge, and the twisting of the wall. Understanding the cause of these phenomena helps with the successful forming operation and allows the achieving the precision of the part and meet the design criteria.

In this chapter, the mechanisms of the defective phenomena found during the incremental forming process are investigated. Based on the experimental observations, different parts with various process parameters and forming schemes are analyzed using the finite element models developed in the previous section to understand the cause of these defective phenomena.

4.1. Thinning/necking in incremental forming

In SPIF, the thinning of the sheets results from the accumulation of strains during contact with the tool. For some components, the thickness variation can negatively impact the part's functionality in the assembly stage. It can bring about the local weakening of the mechanical properties. Usually, the thickness of ISF generally agrees well with the analytical sine law. However, for high wall angled parts, the development of a thinning band that exhibits smaller thickness than predicted by the sine law was observed in the region between the bending and steady-state thickness regions. Young and Jeswiet [11] also observed this phenomenon and stated that it resembles over spinning in shear forming and concluded that it results from a localized

necking and that localized necking can be witnessed. However, further investigation is needed to understand the reason behind the development of the thinning band. To understand the thinning band mechanism, the finite element model developed in the previous chapter is utilized. The comparison between SPIF and TPIF is made for the part with the same geometry. Comparing the two schemes allows locating the source of thinning band since TPIF does not exhibit the thinning band.
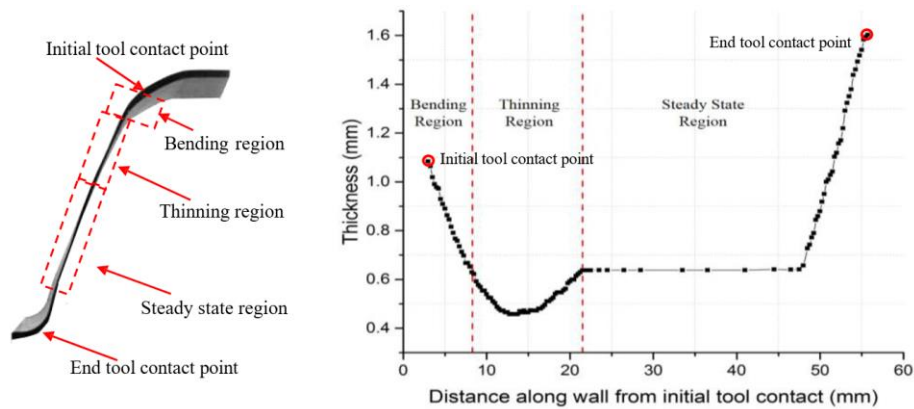
Figure 4.1 Categorization of the formed region based on thickness distribution [6]

4.1.1. Finite element model setup of cone 67°

A SPIF model of 67° cone was utilized to investigate this phenomenon. The model consists of a sheet metal clamped between two clamps and a hemispheric tool. The sheet was meshed with C3D8R hexahedral solid elements, the clamps and the tool were meshed with R3D4 rigid elements. A circular meshing scheme is applied to calculate the geometry resulting from the spiral tool path accurately.

The material properties for AA7075-O were determined by tensile testing. The measured Young's modulus of 72 MPa matches reported data [56]. The material was assumed to be elastoplastic; thus, a combination of isotropic von Mises yield criteria and an isotropic hardening law was used. The hardening curve was introduced as raw table data. Poisson's ratio was assumed

to be 0.33 [56]. No direct boundary conditions were imposed on the sheet, which is held in place by the top and bottom clamps where the top clamp applies the downward vertical force that represents the clamping force. The forming tool path was the same as the one programmed in the experimental setup and was implemented in the model through the displacement control method.

The general contact algorithm provided by ABAQUS was used to specify the contact. The general contact algorithm allows automatic application of contact algorithm for interacting domains based on the contact properties. This allows more robustness in contact formulation than the traditional surface to surface or node to surface contact, which requires the assignment of the slave and master surfaces. Two contact properties, tangential and normal behavior, were specified between the contact partners. The tangential behavior used was a classical isotropic coulomb friction model, which allows the friction coefficient to be defined in terms of slip rate, contact pressure, and average surface temperature at the contact point. The friction coefficient of 0.1, which is consistent with other studies [57] was utilized. The normal behavior specifies a hard contact relationship, which minimizes the penetration of the slave surface into the master surface at the constraint locations. It does not allow for the transfer of tensile stress across the contact interface.

The dynamic explicit scheme was used with a mass scaling factor 10^7. This value was determined by trial and error so that the ratio between kinetic energy and internal energy remains below 5%. The energy ratio is a sanity indication for steady-state dynamic calculations.

4.1.2. Result and discussions

<u>Analysis of the deformation that thinning of the wall</u>

Initially, the SPIF cone was analyzed to observe the deformation process and the occurrence of the thinning band. Five models were simulated to obtain truncated cones with 20

mm, 30 mm, 35 mm, 45 mm, and 55 mm depth. Among the sets of output, equivalent plastic strain and displacements were used for analyzing the thinning of the sheet. Five samples were virtually cut from the formed cones, as seen in Figure 4.2.
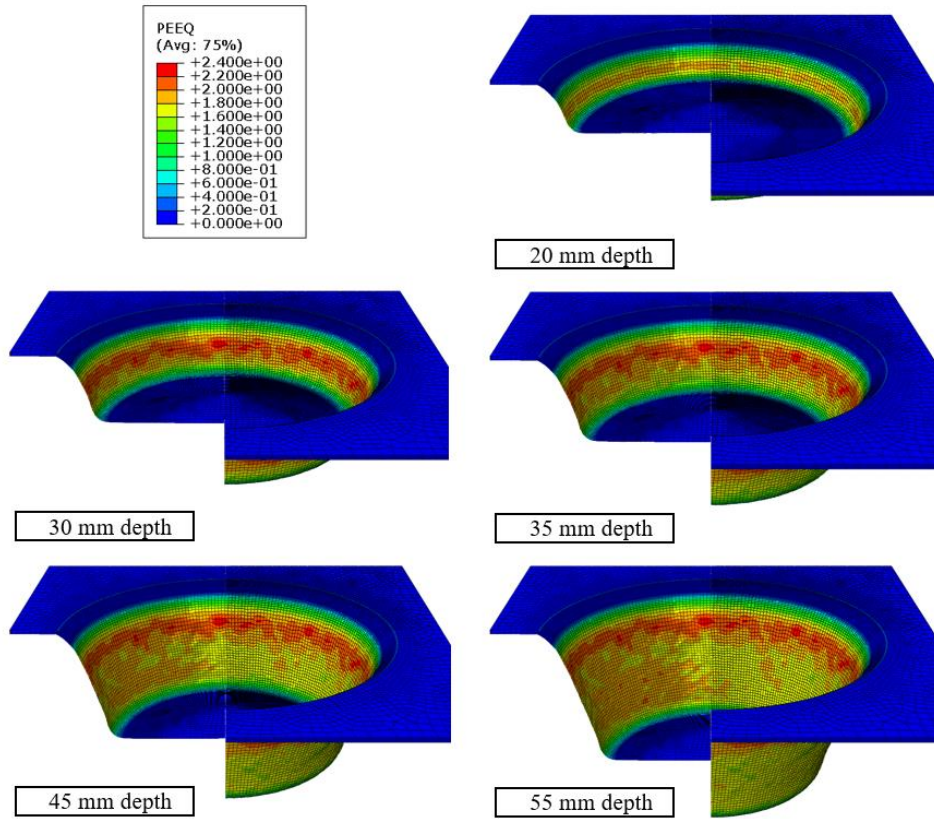
Figure 4.2 Distribution of equivalent plastic strain during forming of a truncated cone of varying depth

The comparison between the thinning in the sheet for the simulation and the experiments was made for an area of interest. The output data was post-processed to compensate for the noise in the data.
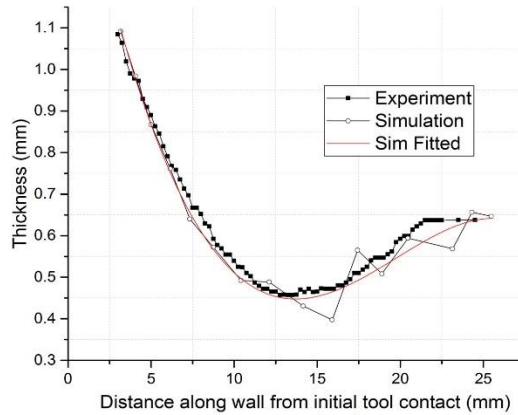
Figure 4.3 Comparison between simulation and experimental results of thickness evaluation in the thinning area

The model shows the excellent agreement of the thinning observed in the experimental samples. Moreover, the position of the maximum thinning location in the wall is well predicted. Three elements were chosen and monitored, each located in the bending, thinning, and steady-state regions where the equivalent plastic strain was computed. These elements were selected to be the most representative in showing the accumulated strains. Thus, the element labels of a column of these elements from the thickness were identified. With the label of these elements, three series of monitoring areas were created: Series A, Series B, and Series C, which corresponds to bending, thinning, and steady-state regions, respectively, shown in Figure 4.4. A new simulation was run up to 55 mm depth recording the equivalent plastic strain for the three selected series.
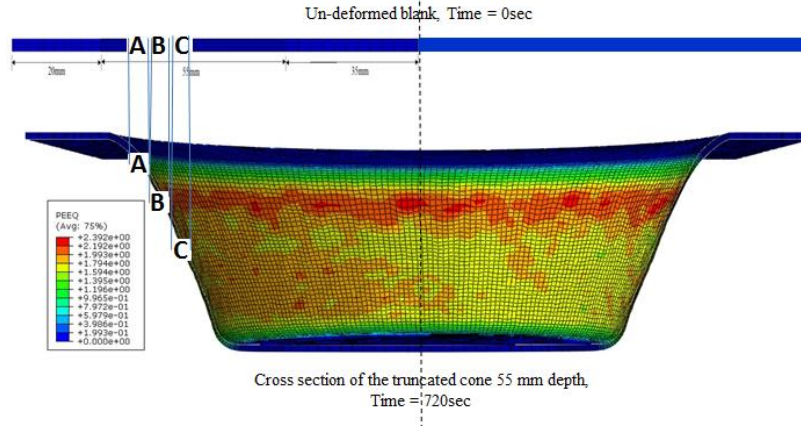
Figure 4.4 Equivalent plastic strain history of the thinning area along the wall. Identification of the Series A, B, and C on the formed cone

The simulation shows limited strain and thinning in all three regions before and after the tool contact. This observation confirms that the deformation in SPIF is dominated by localized plastic deformation under the tool. The grey bar in Figure 4.5 indicates the point in time when the tool is in contact with the element of interest belonging to each series A, B, and C.
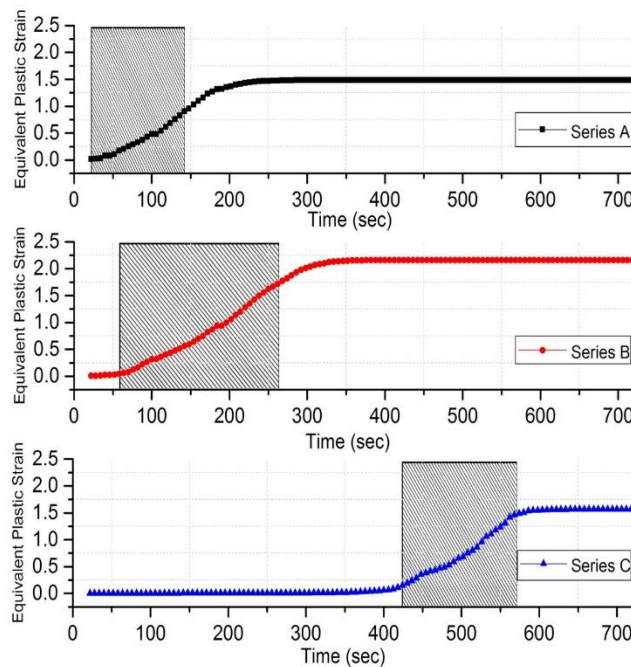
Figure 4.5 Equivalent plastic strain of the wall during the passing of the tool

73

The mechanism of thinning band

A comparison is made between the SPIF and TPIF cases with identical tool paths and boundary conditions to investigate the reason for the thinning band's development. The only difference is that the TPIF has a die instead of the bottom clamp.
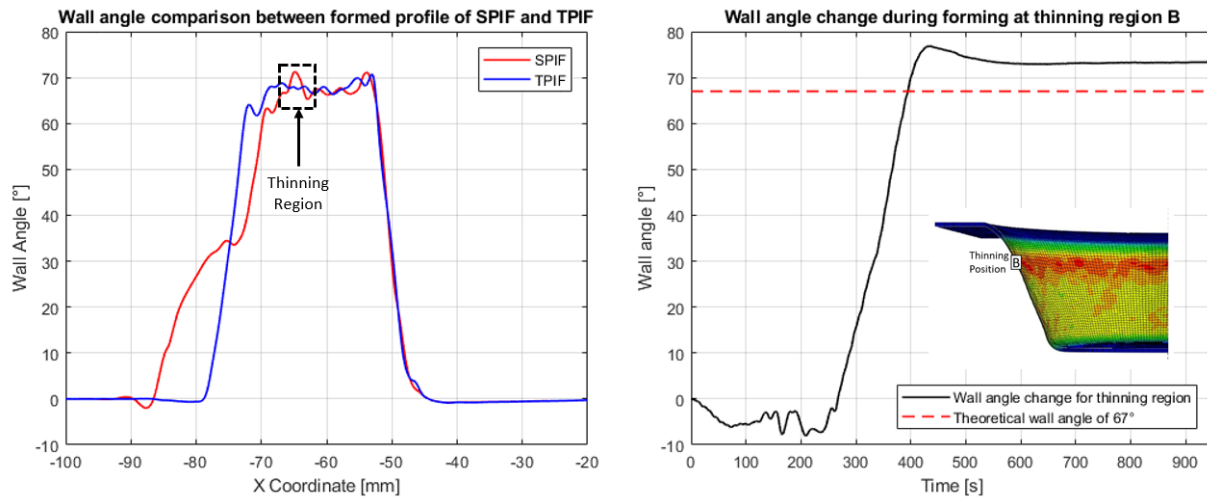
Figure 4.6 The comparison of the wall angle between the SPIF and the TPIF process with identical tool path (right) and the wall angle change during forming the thinning region (left)

The development of thinning region in SPIF can be observed from Figure 4.6, where the wall angle exceeds 67° and has a maximum value of 72°. The increase in the wall angle directly results in the thinner section based on the sine law. In TPIF, no thinning region was observed, and the wall angle remains close to the programmed value of 67°. The wall angle evolution at the thinning region during the forming process is examined to better understand the wall angle. It can be seen that the wall angle at thinning region during forming goes higher than the programmed value of 67° and reaches the maximum value of 76°, and drops to a steady state of 72°. Thus, when the tool is in direct contact with the element in question, the element reaches a higher value of wall angle, resulting in a thinner thickness before coming to a steady-state wall angle.

The cause of the thinning region can be analyzed by looking at the difference in the boundary condition between the SPIF and TPIF. The SPIF has the sheet clamped further out from the region where the forming occurs, while the TPIF has direct support underneath the sheet. The support condition in SPIF is less rigid, and the sheet immediately starts to bend due to the lack of support. As further the tool moves out, the tool exerts forming force in the outward radial and normal direction. The lack of support in SPIF the material internal stress has counter the radial forming force, and this results in the sheet bending around the tool, creating a higher wall angle than 67°, as shown in Figure 4.7. The first subscript of the force components denotes the object that is exerting the force and the second subscript denotes the direction. The $F_{t,r}, F_{t,z}$ are the radial and vertical forming force exerted by the tool, $F_{d,r}, F_{d,z}$ the force exerted by the die, $F_{c,z}$ and $F_{m,r}$ the force exerted by the clamp and the material, respectively. In TPIF, the presence of die the friction between the die and the sheet prevents the sheet from deviating from the programmed geometry. The wall angle is maintained close to the programmed value. It seems that as the tool moves further down the part, this effect by boundary condition is lessened and achieves a steady-state thickness.
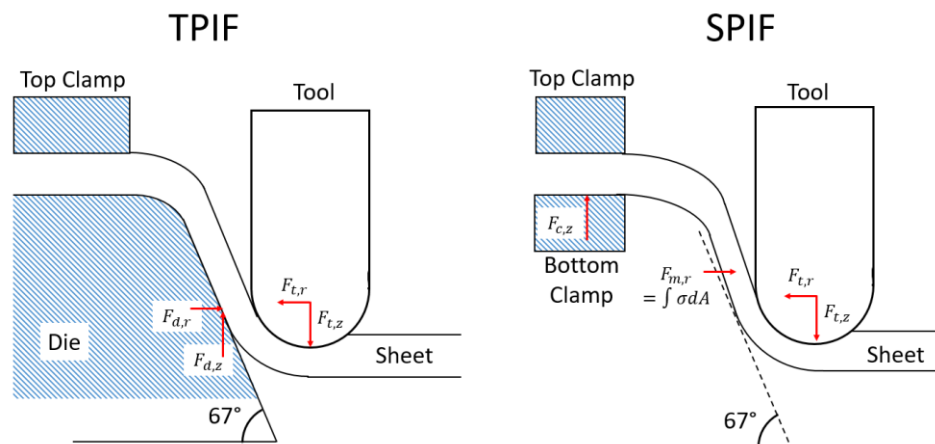
Figure 4.7 Free body diagram comparison between SPIF and TPIF

4.2. Compressive bulge instability in incremental forming

In two point incremental forming (TPIF), the presence of the backing die allows additional process variables, the squeeze factor. The squeeze factor can be categorized into the programmed squeeze factor (PSF) and the effective squeeze factor (ESF). The programmed squeeze factor (PSF) quantifies the amount of material intended to be squeezed between the forming tool and die. Assuming local sheet thickness is estimated by sine law, the squeeze factor can be defined as a ratio of the distance between the tool contact point and die surface to local sheet thickness. However, elastic deflection of forming tools and intrinsic machine compliance effectively reduces the amount of intended squeeze. Therefore, an effective squeeze factor (ESF) at any instant can be represented as Equation (4.2), where Δ is the summation of tool deflection and machine compliance. The ESF will always be less than PSF, and consequently, less material will be squeezed between the tool and die than expected. Empirical relations to estimate machine compliance and tool deflection are produced based on forces later employed to calculate Δ. The equations for PSF and ESF are given below

$$PSF = \left(1 - \frac{d}{t \sin d(90 - \alpha)}\right) \times 100 \tag{4.1}$$

$$ESF = \left(1 - \frac{d + \Delta}{t \sin d(90 - \alpha)}\right) \times 100 \tag{4.2}$$

where d is the squeezed thickness, t the original thickness, and α the wall angle.

During the incremental forming process, the undeformed section in the middle is supposed to flat changes in geometry and develop a spatial curvature of the surface. This phenomenon is called the bulge or pillow effect. Ambrogio et al. [58, 59] reported this effect while studying the springback during incremental forming. Hussain et al. [60, 61] tried to correlate forming parameters with bulge formation using the response surface method. It was shown that there exists

a combination of processing parameters that minimize the degree of bulging. Also, the stress ratio is suggested as a useful parameter in controlling SPIF defects. Al-Ghamid et al. [62] reported the bulge in SPIF using the finite element method (FEM) to connect the hardening of the material, forming depth, and tool size. Isidore et al. [63] tried to predict the bulging effect by changing the tool's shape using FEM. Compressive stress is built up at the tool contact region induces bulge. Changing from hemispheric tool to flat-headed tool decreases compressive stress, resulting in a lower bulge. Mohammadi et al. [64] concluded that depending on the wall angle, the direction of radial stress could be different and that the application of laser heating could improve geometrical accuracy in low angled parts.
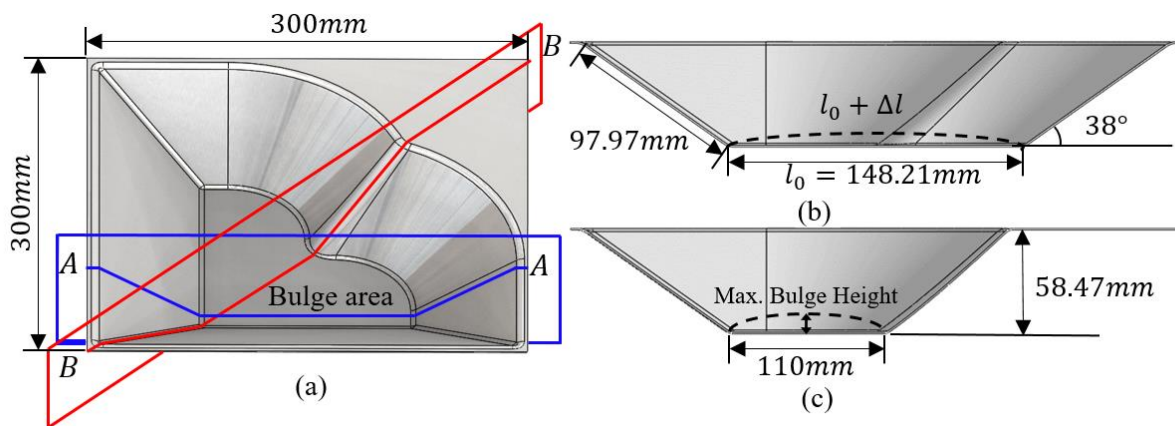
Figure 4.8 Heart shape part (a) cross-cut planes used for measuring the dimensional accuracy, (b) cross-section A-A, and (c) cross-section B-B

The correlation between step size and the bulging effect is investigated for an asymmetric heart shape using the TPIF setup. The detailed geometry of the heart shape is shown in Figure 4.8. The step size influence on bulge is investigated for step sizes of 0.5mm, and 0.63mm for a 10% programmed squeeze factor. The heart shape is a Boeing benchmark typically used to get tensile specimens from its flat side. This part is ideal because it incorporates various features from sharp corners, flat surfaces, and curved surfaces.

4.2.1. Multiscale finite element model setup for TPIF heart

Two different finite element model was created to understand the mechanism of the bulge. The first model simulates forming the whole part, while the second is explicitly created to simulate the material movement during deformation in a segmented region of the wall.
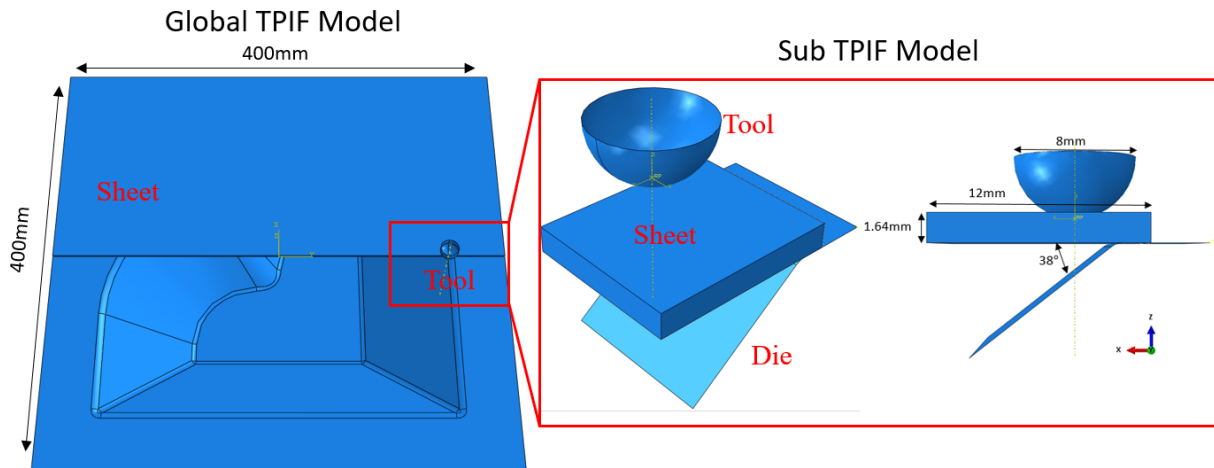
Figure 4.9 Setup of global TPIF and sub-TPIF model

The first model simulates the overall process of ISF forming operation. It consists of an 8mm diameter hemispheric tool, 400 × 400mm blanks of 1.64mm thickness, a heart shape die, and a matching top clamp has been created. The tool, die, and top clamp was modeled with discrete rigid bodies using R3D4, a 4-node 3-D bilinear rigid quadrilateral element. The mesh size of the tool and the die are set to 0.2mm to avoid any distortion due to the roughness induced by the rigid tool or the die. The sheet was modeled with a solid element of C3D8R, an 8-node linear brick element with reduced integration and hourglass control. The blank was meshed with a square element of 1mm with three layers in the thickness direction to capture the change of stress resulting in a total of 480,000 solid elements. A blank holding force of 300kN is applied to ensure no material is drawn in during the forming process.

4.2.2. Results and discussions

The thickness profile and the forming force were compared between simulation and experiment to validate the full TPIF finite element model for the heart shape with 0.5mm step size and 0% squeeze factor. Thickness variation along the wall of the heart shape was considered, both in simulation and experiment.
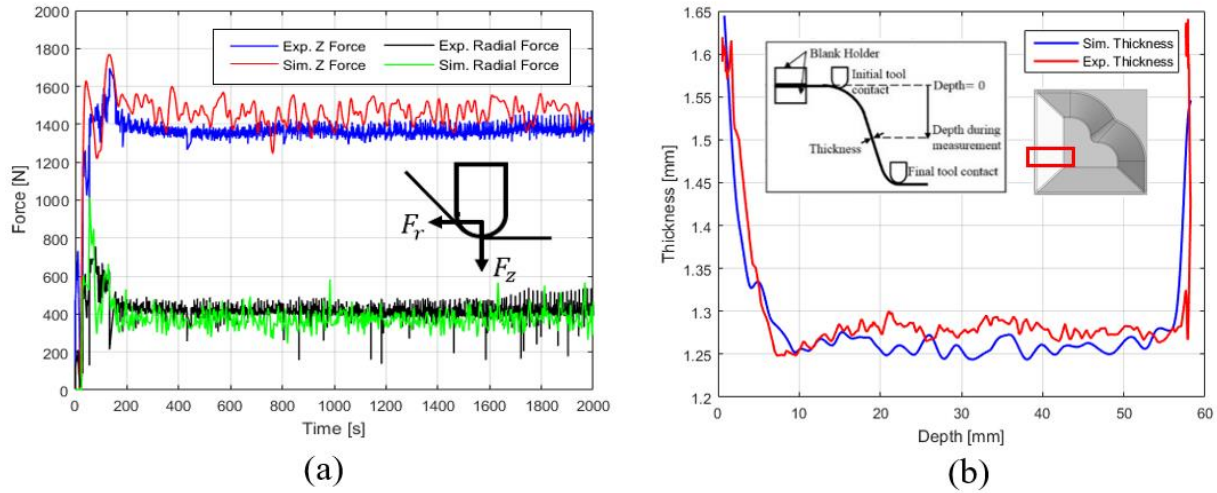
Figure 4.10 Forming force (a) and thickness (b) comparison between experiment and simulation

The thickness profile was obtained by calculating the distance between the top and bottom elements. The results show a good correlation between experiment and model for both thickness and forming forces, as shown in Figure 4.10. Principal stress components in the elements near the bottom of the walls were analyzed to confirm whether compressive stresses can produce the bulge, as proposed by Isidore et al. [63].
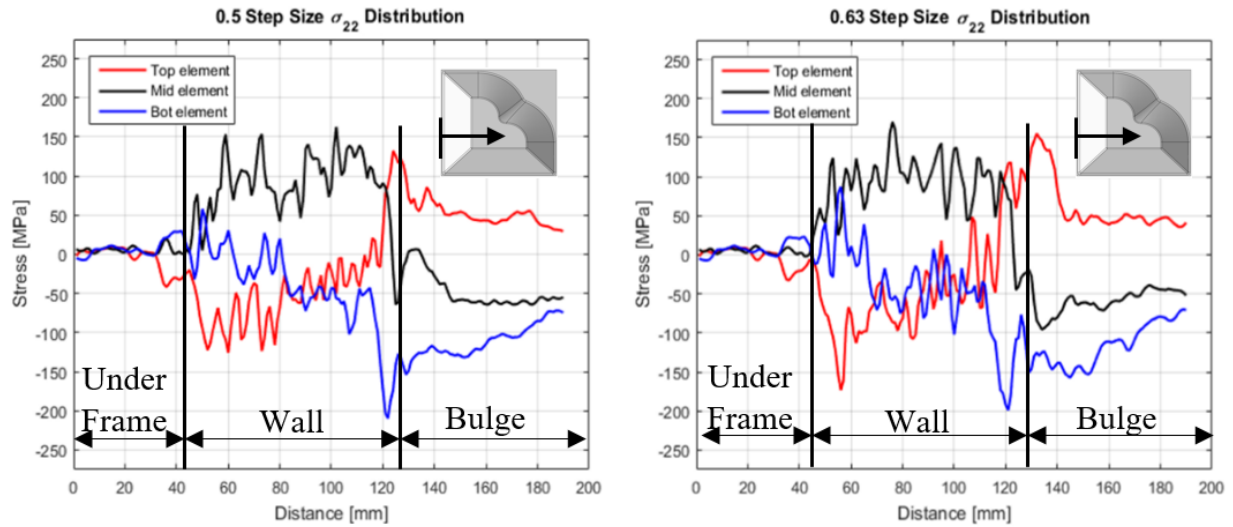
Figure 4.11 Stress component in the lateral direction along the wall calculated from the global model

Figure 4.11 shows the compressive stress component, σ_{22}, along the wall, in the local coordinate system. The plot of the evolution of σ_{22} in the top, middle, and bottom elements against the distance from the edge of the sheet in the lateral direction show that in the bulge area, compressive states are mostly induced in the bottom element while the top element is in stretching. The difference between the level of stresses developed in the global model is insignificant between the 0.5mm and 0.6mm step size. This small difference was not aligned with the experiment's result, where the heart with the 0.63mm step size showed a lower bulge. If Isidore's findings were to hold, there should be a significant difference in the compressive stress values. It can be concluded that the mechanism of bulge development cannot be fully explained by the effect of the compressive stresses along the wall. The finite element sub-model was proposed to understand better the material squeezing during forming.
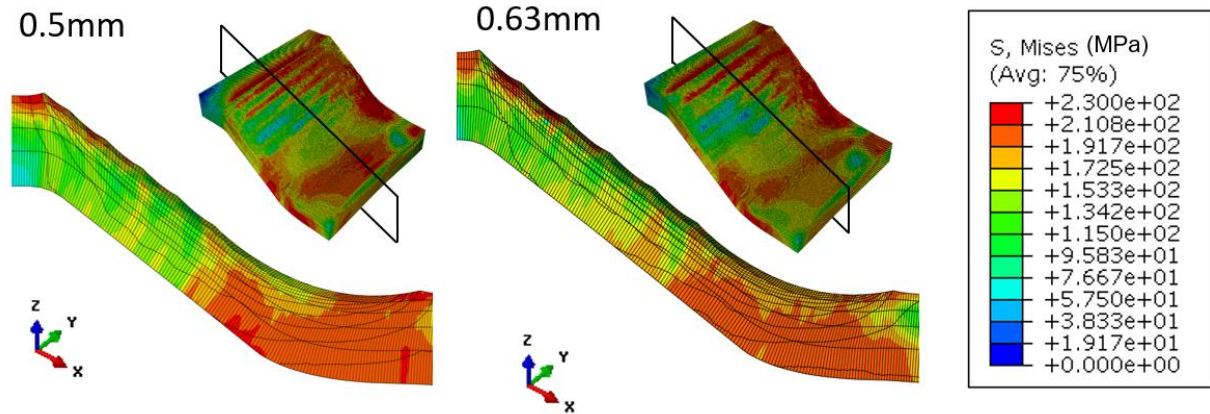
Figure 4.12 Result of the sub-model showing profile and von Mises stress distribution for step down of 0.5mm and 0.63mm

The second model (submodel) is a segmentation of the full TPIF model in the flat walled section to predict the surface profile during forming. This model is created to understand the effect of step size on bulge formation. The sheet size was modeled to 10mm×12mm ×1.63mm and the mesh size of 50µm ×50µm with six C3D8R elements across the thickness. Two step size values, 0.5mm and 0.63mm, were used for modeling. Only seven passes of the tool were considered identical to the original tool path used in the full TPIF model. Boundary conditions were imposed on the edges of the sheet to simulate actual conditions from the incremental forming process. The blank holder side edge was fixed while the opposing side was constrained in x and y while allowing movement in z. The edges perpendicular to the tool path were constrained in the direction of the tool path.
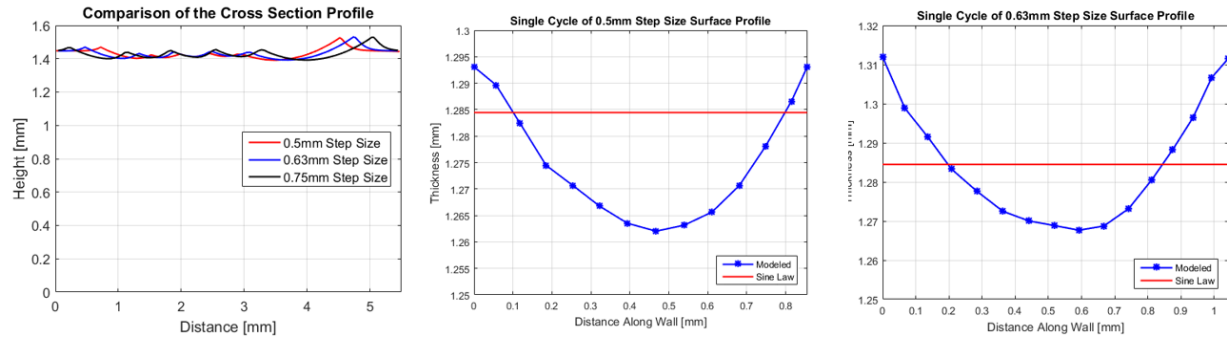
Figure 4.13 Overall comparison of the profile and its respective single cycle from the sub-model

The full TPIF model results were compared with the experimental data for a step size of 0.5mm, and 0.63mm. This comparison was focused on the bulge height in section B-B, as defined in Figure 4.8. The full TPIF model predicted the thickness variation well but was less accurate in the bulge dimensions (9 mm simulation versus 4 mm experiment) in Figure 4.15. Analysis of the model compared to the experiment showed that while the overall thickness of the part was close with only 20~30μm difference, the mesh was not able to capture the surface profile generated during forming, which resemble tool path striations parallel to tool path as reported by Nath et al. [65]. One potential cause of this prediction is that the step size in the tool path (less than 1mm) is smaller than the mesh size (1mm), resulting in the model's inability to capture geometrical changes smaller than 1 mm. Thus, a smaller mesh size was tested to capture the surface profile during the forming process. This mesh size change increased the computational time by more than 500%, which was not acceptable since the original computational cost was already around 50 hours. Thus, the sub-model was used to simulate forming with a higher resolution. The results showed surface profiles with repetitive half-sine waves corresponding to each step size, as seen in Figure 4.14. A single profile was selected at the mid-point of the simulation to minimize any end effect from the boundaries. The profile was then rotated by 38° (wall angle on the heart shape part) to align to the coordinate axis and allow easier post-processing. The bulge height in section A − A, Figure 4.8,

82

was considered for analysis. The assumption was made that while the 3-D profile of the bottom of the heart could be different depending on the surrounding wall geometry conditions, the bulge profile in section A − A would only be influenced by the amount of material being pushed in from either side of the profile. The amount of material transfer has been calculated from the simulation using Equation (4.3) and Equation (4.4). The values are compared with the experimental values.
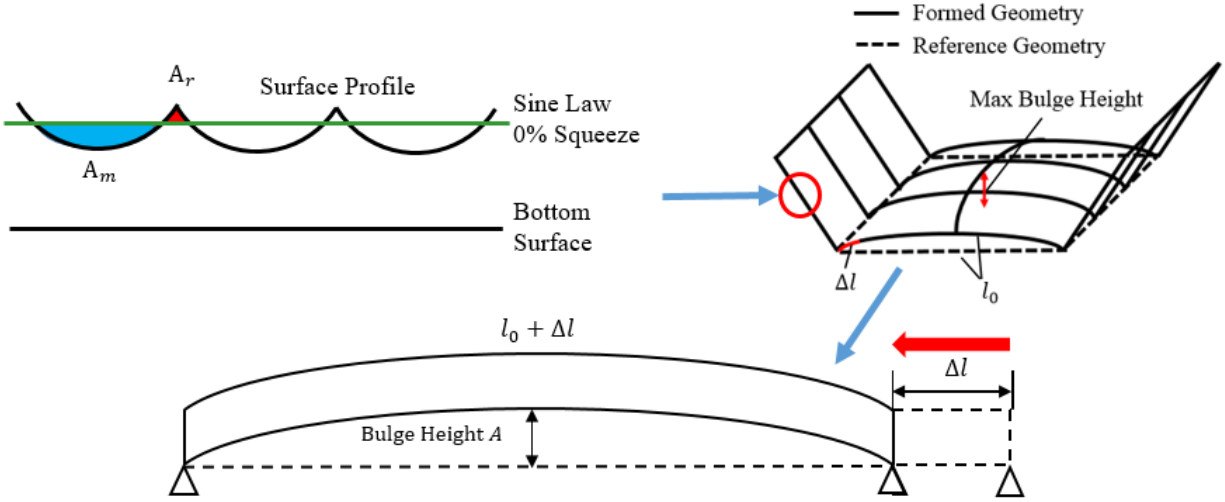
Figure 4.14 Schematic of the relationship between material movement and bulge formation using beam bending

$$\Delta l_{\exp} = l_{bulge} - l_0 \tag{4.3}$$

$$\Delta l_{\bmod el} = \frac{2n_s \left(\sum A_m - \sum A_r \right)}{t} \tag{4.4}$$

where l_{bulge}, and l_0 are the measured bulge and reference length in the experimental part, A_m, and A_r are the area under one period of the surface profile for modeled surface and sine law profile, respectively. The n_s is the number of cycles that the tool did to reach the bottom of the part, and t is the sheet's thickness. The results of the calculation versus experiments for 0.5 step size are Δl_{model} =1.9533mm, Δl_{exp} = 1.9772mm and for 0.63 step size Δl_{model} =0.7883mm, Δl_{exp} = 0.6996mm.
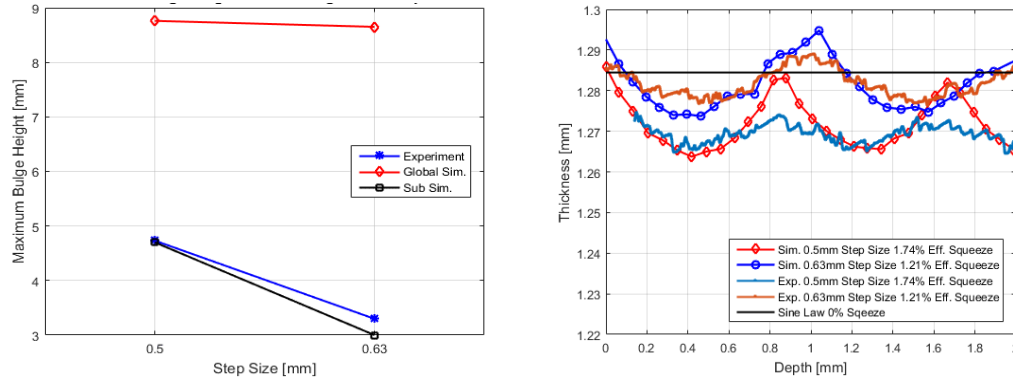
Figure 4.15 Comparison of the bulge height and profile with experimental measurement

The results show that different surface profiles are created due to a combination of the step size and the squeeze factor. For 0.5mm step size, a surface profile consisting of an average of 0.83mm period between peak to peak was created with a distance of 16μm from peak to valley. For 0.63mm step size, a surface profile of 1.0436mm between peak to peak and distance of 20μm between peak and valley. The area between the surface profile of 0.5mm step size and the sine curve is larger than that of the area between 0.63mm step size and sine curve. The area above the sine law curve can compensate for the area below, resulting in a smaller overall area difference, as shown in Figure 4.15. It can be concluded that more material is being pushed into the bulge area specified in Figure 4.8 for 0.5mm step size compared to 0.63mm step size. However, peak to peak period and peak to valley amplitude are larger than that of 0.5mm by 4μm.

Table 4.1 Comparison of the calculated material movement between the experiment and the model

Step Size	0.5mm	0.63mm
Area of the material accumulated per cycle A_m	0.0178mm^2	0.0091mm^2
No. of cycle n_s	110	87
Δl_{model}	1.9533mm	0.7883mm
Δl_{exp}	1.9772mm	0.6996mm

Although the above approach can predict the 2-dimensional accumulation of the material, additional expansion of the method is required to predict maximum bulge height, resulting from 3-dimensional material accumulation. Since bulging at the center is due to the addition of the material resulting in the compressive state, it can be considered a buckling phenomenon. Thus buckling analysis can be used to convert lateral length change to vertical displacement. The bottom section of the heart where the addition of the material results in the buckling of the part can be considered simply a supported element. The displacement of the bottom surface then follows second order differential equation given in Equation (4.5)

$$EI\frac{d^2w}{dx^2} + Pw = 0 \tag{4.5}$$

where w and x being the vertical and lateral displacement, E, I, and P being the elastic modulus, the moment of inertia, and the compressive load, respectively. Using the boundary conditions of simple support, the solution then becomes

$$w = A\sin\frac{n\pi x}{l_0} \tag{4.6}$$

where A is the amplitude, n the number of half-sine waves and l_0 the base length, with $n=1$.

The results show that the calculated maximum displacement is 4.3mm for 0.5mm step size and 3mm for 0.63mm step size, respectively, as shown in Figure 4.15. This result indicates an improved prediction of the sub-model compared to the full TPIF model. It can be concluded that the bulge during the ISF process is a combination of compressive stresses and a buckling phenomenon due to the accumulation of the material during forming, which is dependent on the combination of step size and squeeze factor.

4.3. Twist in incremental forming

Several researchers have reported the twist that occurred during incremental forming. Matsubara [66] reported a twist in TPIF with a female die. The formed part was not held rigidly enough to support subsequent forming operation, resulting in an uncontrollable twist. Neto et al. [67] investigated the stress that develops during incremental forming and the corresponding strain for several process parameters. The SPIF of a contour cone specimen was reported to have a twist as much as 2.5°. The amount of twist varied with the depth. Duflou et al. [68] studied the twisting that occurs on the cone and pyramid parts. Duflou identified two kinds of twists; the conventional twist observed in the low angled parts and the counter-intuitive reverse twist observed in the high angled part. The counter-intuitive reverse twist was witnessed mostly in the pyramid parts with the ribs. These parts exhibited higher strain in the meridional direction. Asghar et al. [69] investigated the effect of process parameters, the step size, sheet thickness, opening diameter, and tool diameter on the twist on the walls. It was seen that twist increases with larger step size, smaller tool diameter, and sheet thickness. Although many researchers reported the twist, its mechanism was only superficially explained via a tangential force that develops during incremental forming.

The tool path scheme plays a vital role in achieving the final geometry. Generally, in ISF, a spiral or a unidirectional contour approach is used. This type of tool path has the potential to involve the twisting of the sheet. Thus an alternate approach of the bidirectional scheme has been investigated. It was found to be effective in reducing the twist in incremental forming parts. Al-Attaby et al. [70] and Suresh et al. [71] observed the reduction of the twist using the bidirectional scheme in cone parts. They confirmed that the bidirectional scheme resulted in a significantly less twist than the unidirectional spiral or contour scheme. Finally, an effort was made by Liu et al. [72], where a multi-pass incremental forming was conducted with various combinations of tool

movement direction. The result showed that the twist could be reduced by changing the tool movement direction in the subsequent passes.

The twisting phenomenon in incremental forming is one of the side effects of the forming being done as an accumulation of localized deformation to achieve the final geometry. The mechanism of twist generation is necessary to understand and eliminate the twist. An investigation of the twist using the finite element model is conducted from a material point of view. The generated stresses are investigated to explain the mechanism of the twist.

4.3.1. Definition of the twist angle with respect to the part geometry
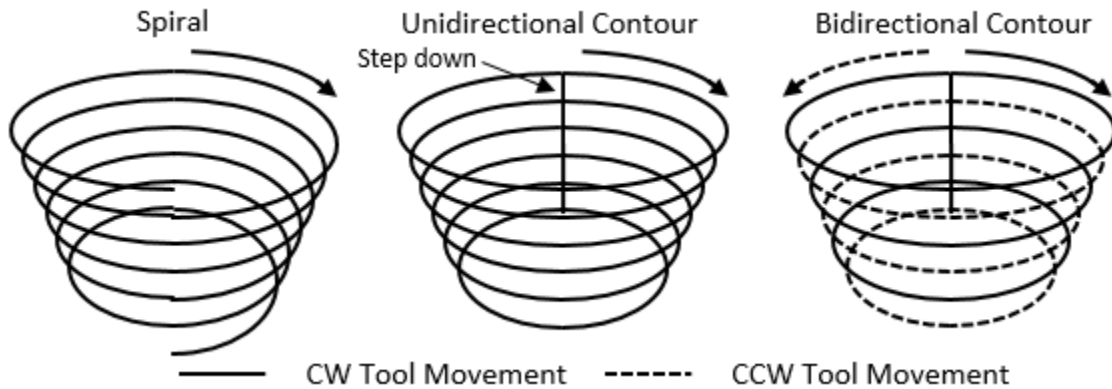
Figure 4.16 Spiral, unidirectional and bidirectional tool path scheme of a single point incremental forming (SPIF) of a truncated cone
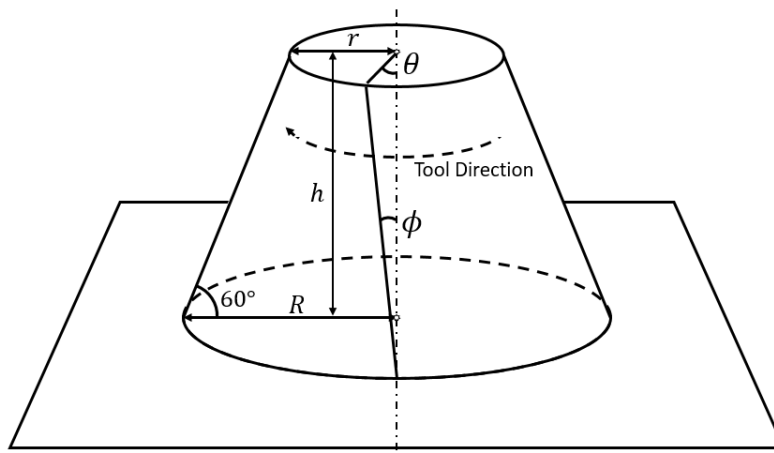
Figure 4.17 Schematic of the relationship between geometry and wall twisting angles θ and ϕ

The twist in the cone was measured in both experiments and modeled truncated cone using Image J software. The twist can be quantified in two ways, by measuring the twist in the wall of the truncated cone ϕ and by measuring the twist in the undeformed region in the middle θ. Generally, the two twist angle ϕ and θ are related by Equation (4.7), assuming ϕ and θ are small, and the wall angle is $60°$ where the h is the depth of the cone and r the bottom radius.

$$\theta = \phi \cdot \frac{h}{r} \cdot \sin 60°$$ (4.7)

4.3.2. Finite element model setup with different tool path scheme

The model consists of a tool, a set of frames, and a sheet. The tool and the frame were modeled with R3D4 rigid elements and given the same dimension observed in the experimental setup. The size of the mesh was kept around 0.2mm to ensure smooth curvature in the tool. The sheet has a dimension of 200mm×200mm with a thickness of 1.64mm and was meshed with C3D8R, an eight noded linear brick element with reduced integration. A circular meshing was adopted with $360°$ mesh in the circumferential direction, a 0.5mm mesh in the axial direction, and five layers in the thickness direction. The five layers were chosen after a parametric study shown in chapter 3. The result showed that five layers in the thickness direction provided a result with accuracy within 10%, while the computational cost was less than a quarter of that of 7 layers.

An elastoplastic constitutive material model was considered for the alloy AA7075-O. A Voce type hardening law $\sigma = k_0 + Q(1 - e^{-\beta\varepsilon})$ was identified based on experimental tensile tests. The coefficients for this law are given in Table 4.2 along with Von Mises yield criterion to describe the yield locus where the k_0, Q, and β are the tensile yield strength, saturation stress, and material constant.

Table 4.2 Mechanical properties and Voce law coefficients for A7075-O

Modulus	Density	Poisson's Ratio	k_0	Q	β
69.74GPa	2810kg/m^3	0.33	91.30 MPa	149.34MPa	-26.71

A clamping force of 200kN was applied in the z-direction on the top frame to ensure no material movement while the bottom frame was held rigid. The general contact algorithm in ABAQUS is used along with the friction coefficient of 0.1.

4.3.3. Results and discussions

The truncated cone of 60° with a depth of 50mm was created experimentally and was compared with the modeled result for validation. Three cases were investigated, each with a different tool path scheme explained in the previous section. The finite element model was first validated against the experiment by comparing geometry and the angle of twist. The stress state on the wall of the part in the same location is then analyzed to explain the twist occurring in the experimental part.

The exact values are shown in Table 4.3. The unidirectional spiral results in the largest amount of twist with the value of 1.25°, followed by unidirectional contour with the twist value of 1.1° and bidirectional contour with the twist value of 0°. It can be seen that no twist resulted from the bidirectional contour.
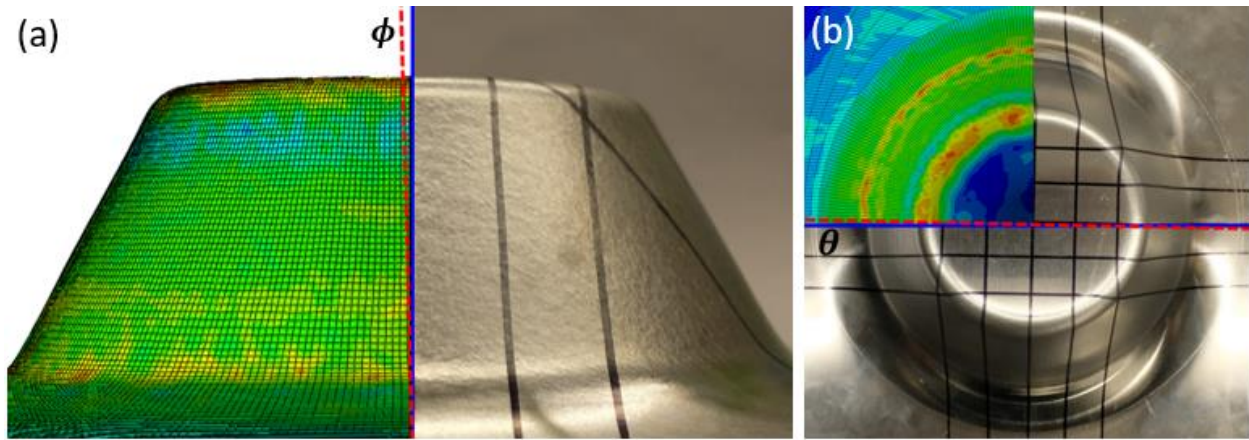
Figure 4.18 (a) Lateral view showing ϕ and (b) top view showing θ and the comparison between the experimental part and a modeled part (showing Von Mises Stress) for unidirectional contour

Table 4.3 Comparison of the twist in the experiment and modeling of θ

	Unidirectional Spiral	Unidirectional Contour	Bidirectional Contour
Experiment	1.25°	1.1°	0°
Model	1.18°	1.04°	0.1°

The stress state on the wall is analyzed to understand the impact of the different schemes. The element was chosen that is aligned with the x-axis at a depth of 35mm. This location is considered to be in a steady state of thickness distribution, meaning that the initial transient effect of the bending region is no longer affecting the wall angle and thickness distribution. Examination of all stress components revealed that values of σ_{11}, σ_{22}, and σ_{33} has no significant difference, as shown in Figure 4.19 (a) and (b). The σ_{12} component showed a significant difference between the cases, and the source of the twist could be traced back to the shear stress component σ_{12}.

Figure 4.19 (c) shows the modeled shear stress σ_{12} for an element in the middle of the wall for each of the three cases. The stress that develops up to $t = 500s$ is the stress develops while the material above the element is being deformed. The period between $t = 500s$ and $t = 600s$ is when the tool is in contact with the element that is being examined. From $t = 600s$ to end is when

90

the material below the element is being deformed.

Before the tool reaches the element under examination, it can be observed that the stress level is not too different between the three cases for $t < 300s$. Once the tool reaches the vicinity of the element, the unidirectional spiral and contour develop monotonously changing σ_{12} component. However, the bidirectional contour shows oscillation of the stress component. When the tool is in direct contact with the element in question, it can be observed that the stress level of the unidirectional spiral and contour exhibit a monotonous increase in the stress value having a similar stress level. As for the bidirectional contour, oscillating shear stress develops.
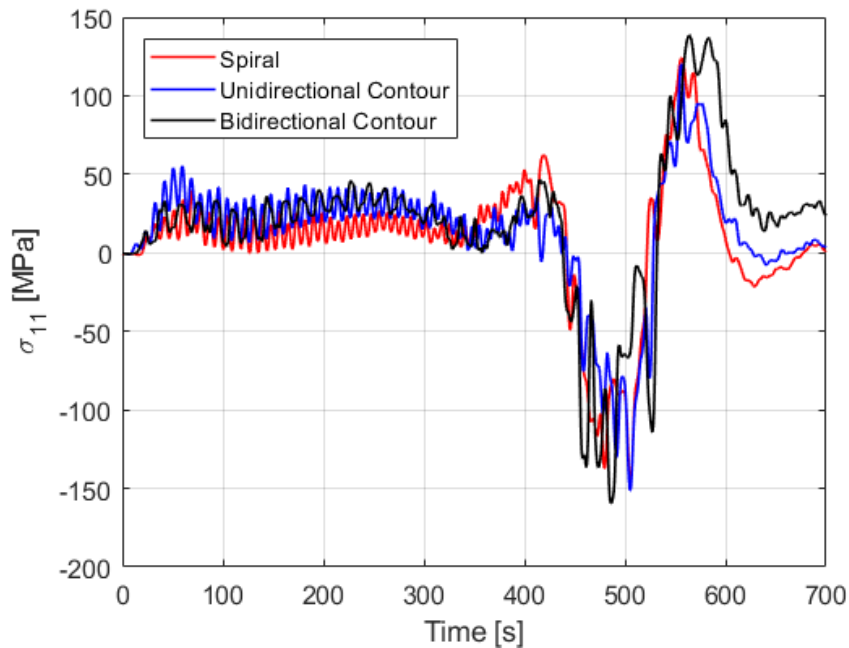
(a)
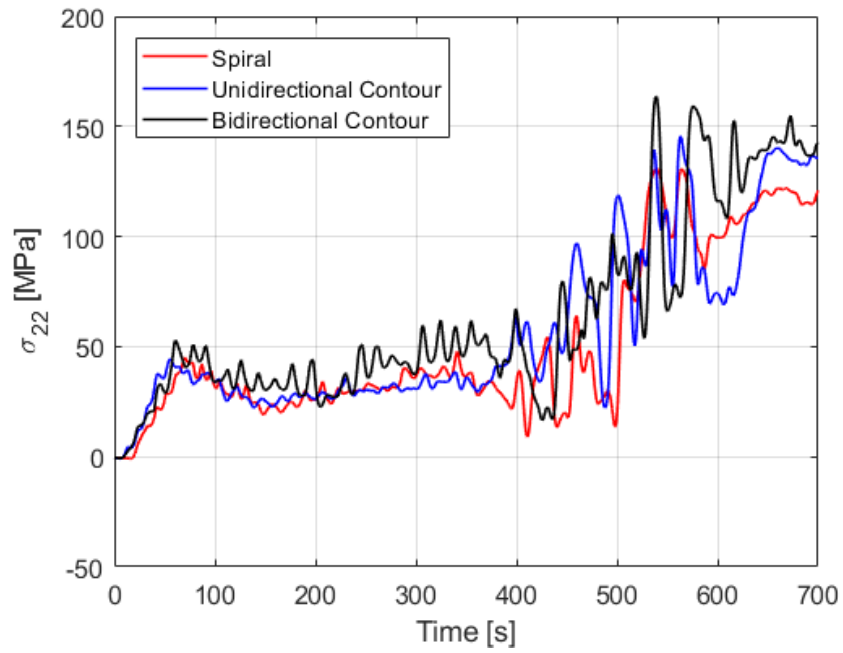
(b)
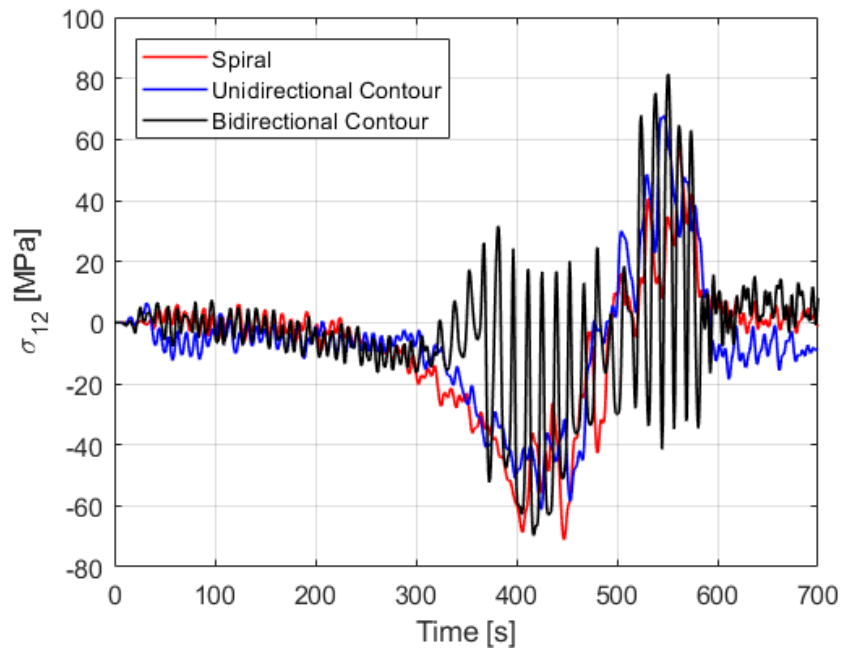
(c)

Figure 4.19 Comparison of the stress comparison of the element on the wall for (a) σ_{11}, (b) σ_{22} and (c) σ_{12}

The examination of the stress component and the angle of twist in the unidirectional scheme suggests that the positive monotonous shear stress drives the twist in increments. As the forming progress, these incremental twisting accumulate into the overall twisting of the wall. In the bidirectional contour case, the oscillating tool motion ensures that any twist in one direction is compensated in the subsequent tool motion. Comparing the unidirectional spiral and contour suggests that having a contour or a spiral tool path does not influence the occurrence of the twist. It seems that the twist is accumulated in the material even with the step-down motion. From this accumulative nature of the twisting, it is possible to deduce a relationship between the angle of twist and the process parameters as given in Equation (4.8). The θ is the angle of twist, N the number of revolutions that the tool does to reach the bottom and $f(\sigma)$ is a function of σ where the variables that affect the stress are taken into account, μ the friction coefficient, t the sheet thickness, r the radius of the tool, and α the wall angle.

$$\theta = N \cdot f(\sigma(\mu, t, r, \alpha)) \tag{4.8}$$

The $f(\sigma)$ would be influenced by the size of the step-down, friction coefficient, sheet thickness, tool radius, and wall angle for a given material.

Surface roughness has been measured using the profilometer for all three cases in the steady-state region of the wall to inspect the formed part's surface quality. The result is shown in Table 4.4. It reveals that the bidirectional tool path scheme had the lowest value of surface roughness on the tool side than the other two cases, while the backside had the roughest surface finish. No deteriorating surface was observed, as suggested by Duflou [68]. The question of whether the bidirectional scheme is flattening the surface asperities during forming resulting in a smoother surface remains to be answered for future study.

93

Table 4.4 Measurement of surface roughness_for both the tool side and the backside

			Spiral	Contour	Bidirectional
Rolling Direction // Forming Direction	Tool Side	Striation Peak (μm)	0.202 ± 0.015	0.218 ± 0.015	0.189 ± 0.018
		Striation Valley (μm)	0.202 ± 0.012	0.218 ± 0.018	0.184 ± 0.014
	Back Side	Forming Direction (μm)	0.297 ± 0.032	0.364 ± 0.029	0.374 ± 0.040
Transverse Direction // Forming Direction	Tool Side	Striation Peak (μm)	0.197 ± 0.014	0.204 ± 0.011	0.199 ± 0.030
		Striation Valley (μm)	0.192 ± 0.015	0.206 ± 0.024	0.219 ± 0.048
	Back Side	Forming Direction (μm)	0.365 ± 0.029	0.348 ± 0.030	0.372 ± 0.026

4.4. Summary and conclusions

In this chapter, various defective phenomena found during the ISF process are investigated. The finite element model developed in the previous chapter was utilized to investigate the mechanisms of the three significant defective phenomena, thinning, bulge, and twist. For the occurrence of a thinning band, it was found that the lack of support in the SPIF setup resulted in the internal stress that counteracts the radial forming force, which resulted in the local increase of the wall angle, thus induced more thinning than necessary. The bulge resulted from the accumulation of the incremental amount of material being pushed forward during forming. The difference between the volume of the formed geometry and the volume of ideal geometry is pushed into the undeformed region. This additional material creates compressive stress and bending of the material in that region, which resembles the beam bending. The twist in ISF was due to the shear stress that developed during the process. The use of bidirectional contour resulted in the oscillating shear stress, which compensated the material movement and resulted in a net-zero twist. By understanding the origin of these defective phenomena, it is possible to minimize their occurrence and contribute to achieving the precision of the part by selecting appropriate process parameters.

Chapter 5 Analytical Modeling of Incremental Forming

In this chapter, an analytical model for predicting 3-D geometry in incremental forming is developed based on the previous chapters' understanding. The ability to predict the incremental forming results accurately reduces the trial and error associated with selecting the process parameters that result in optimal geometry. This reduction of trial and error associated with tuning the process parameter can lead to a decrease in the cost of manufacturing a part using incremental forming. While the FEM models provide a good prediction of the incremental forming process, as demonstrated in chapter 3, the work required to create an accurate model is not trivial. Thus, based on the understanding found in previous chapters, analytical models are developed to make predictions of the formed geometry in the place of the FEM models.

This chapter's contributions are: (1) an analytical model for the prediction of thickness geometry based on the material movement model, and (2) an analytical model for predicting bulge based on the calculated results of the first analytical model and the buckling model. The combined output of the two models will give the full prediction of the geometry and thickness.

In the following section, the two analytical models' detailed schemes are introduced, followed by validating the prediction by comparing them to the experimental result.

5.1. Motivation for developing an analytical model for ISF prediction

Reliable models for predicting geometry and material property are required to speed up the adoption of incremental forming in the aerospace industry for part manufacturing. Many works have introduced analytical and physics-based models to predict thickness variation, damage, and

95

bulge. Among these models, the sine law analytical model is the most well-known for predicting ISF thickness [28, 29, 30, 31] and the final shape of the parts based on its wall angle. While the current analytical models developed for ISF can provide a swift prediction of the geometry, the prediction accuracy remains low since it does not consider the unique deformation found in ISF. To account for the material behavior, many researchers turned to various finite element models based on in-house code such as Lagamine; a finite element code developed at the University of Liege [73] and commercial software (Abaqus [38, 73], LsDyna [48, 74, 75]). These models consider various material models, such as von Mises simple yield functions, to more complicated yield functions such as Barlat 2002-2d [76]. Through simulation of ISF processes, it was possible to understand better the forming mechanisms in ISF, which allowed the explanation of the origin of the thinning [26] and provide a basic understanding of the bulge formation and evolution [60, 62, 77]. It was found in the previous chapter that bulge formation was due to the accumulation of a small amount of material that piles up and creates instability of the sheet in undeformed areas [78]. This accumulation is due to the multiple passes of the tool that generates scallops – defined as a periodical surface roughness feature on the part's tool side. This phenomenon is difficult to accurately capture using finite element models because they require the mesh's resolution to be small enough to capture the surface profile, which is in the order of microns. Any attempt to make the mesh size small would result in a high computation time and become too costly to solve.

In the race to create robust prediction tools, data-driven methods are being adopted in the industry community. The prediction error found in these data-driven methods depends on the number of training cases that represent an obstacle to their development. Recently, Mozaffar and Cao [79] published data-driven models for material characterization and optimization of the metal

forming processes. However, it is still a challenge to use them in the finite element modeling (FEM) of incremental sheet forming (ISF) due to a limited database regarding this process.

In this chapter, two new algorithms are proposed, one for thickness prediction and the other for the bulge prediction in two point incremental forming (TPIF) and single point incremental forming (SPIF). The algorithms are established based on data collected from experiments and simulations in the previous chapters. The Boeing benchmark part named heart shape is used to validate the algorithm as its complex asymmetric shape provides challenges which a simple cone would not provide.

5.2. Experimental setup

5.2.1. Experimental setup for TPIF

The experimental parts are manufactured using the TPIF process, set up on a Cincinnati HMC 400 EP CNC milling machine integrated with a 4-component KISTLER force sensor. An aluminum sheet of AA7075-O with a sheet thickness of 1.64mm is clamped between the die and the top clamp. A layer of MoS_2 multipurpose grease was applied on the sheet surface to reduce friction in the tool-sheet interface. Forming forces were continuously recorded and monitored at 100 Hz frequency using a custom-built Labview interface with the Kistler force sensor. A hemispheric tool with a radius of 4mm is used, which moves at 2,540mm/min with spindle speed set at zero and unlocked condition. The step-down size between each contour is set to 0.50mm and 0.63mm. Based on the heart shape CAD, a contour-type tool path was generated using AMPL toolpath generation software [80] developed by Northwestern University. The overall experimental setup is shown in Figure 5.1 and Figure 5.2.
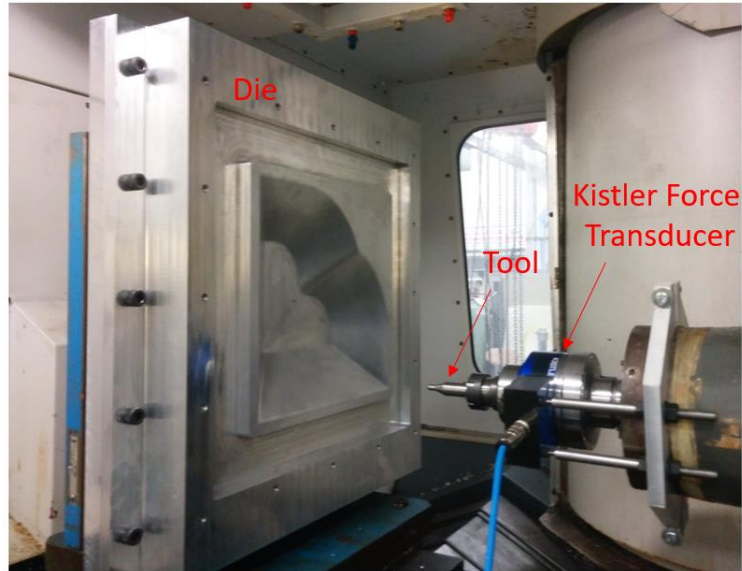
Figure 5.1 Set up of TPIF of the heart using the Cincinnati CNC with a hemispheric tool with a mounted force transducer and the die

Figure 5.2 (a) Experimental setup for a cone fabrication using TPIF on Cincinnati CNC, and (b) laser scanner set up for part geometry measurement using a Romer Absolute Arm with Integrated Scanner 7525SI

5.2.2. Measurement of the formed parts

To measure the geometry and the deviation of the incrementally formed part, a laser scanner, Romer Absolute Arm with Integrated Scanner 7525SI, was used, which has the capacity of single point repeatability and scanning system accuracy of 0.027mm and 0.063mm, respectively. During the scan, the software collects the points in the point cloud format and meshes the points

to form surfaces. Once the scan is complete, a CAD file is imported into the Polyworks Inspector software. It goes through successive translation and rotation to align the point cloud data coordinate system to the reference CAD. These results are then compared with the results of the analytical model for validation.
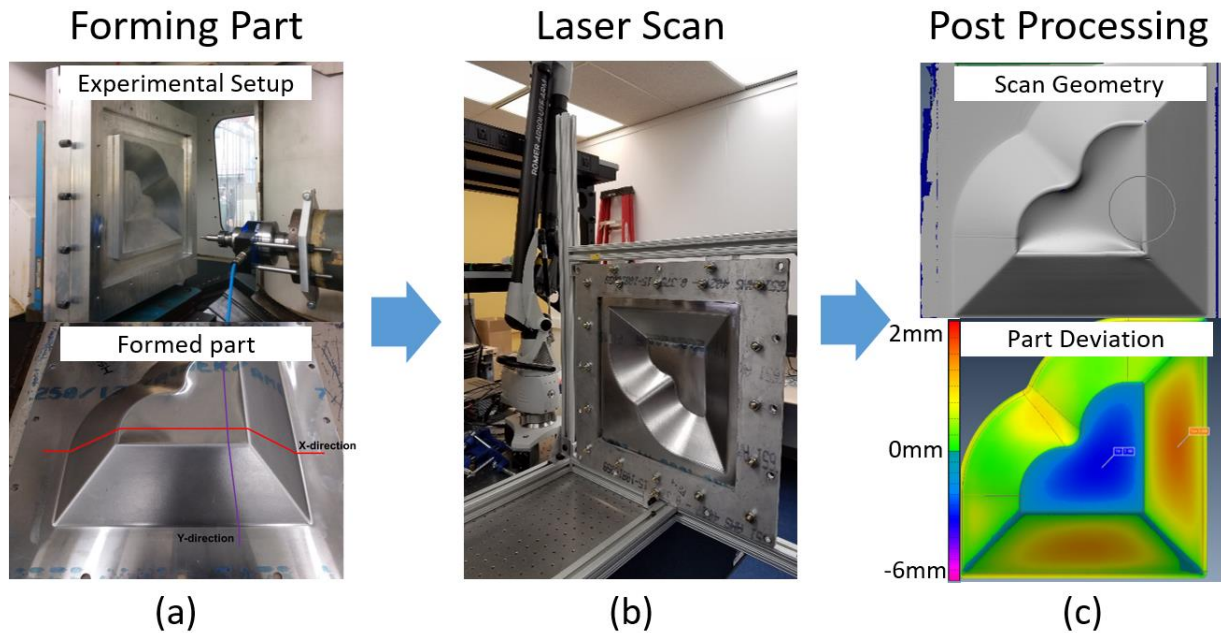
Figure 5.3 The flow chart of the investigation steps (a) part creation, (b) measurement, and (c) post-processing of the data

The heart shape part is ideal for validating the analytical model since it has a complex asymmetric shape. The surface of the heart consists of concave, convex, and flat surfaces. It is formed with the 400mm by 400mm sheet to include the long flat edge of the heart, which is 300mm. The depth of the heart is 58.47mm, with a wall angle of 37.5°. The radius of curvature for convex surface ranges from 58.09mm to 130.78mm, while the radius of curvature for concave surface ranges from 15.94mm to 23.48mm. During the experiment and modeling, it is possible to incorporate various process parameters for the tool radius, squeeze factor, sheet thickness, and step-down size. The details of the heart geometry are described in Figure 5.4.
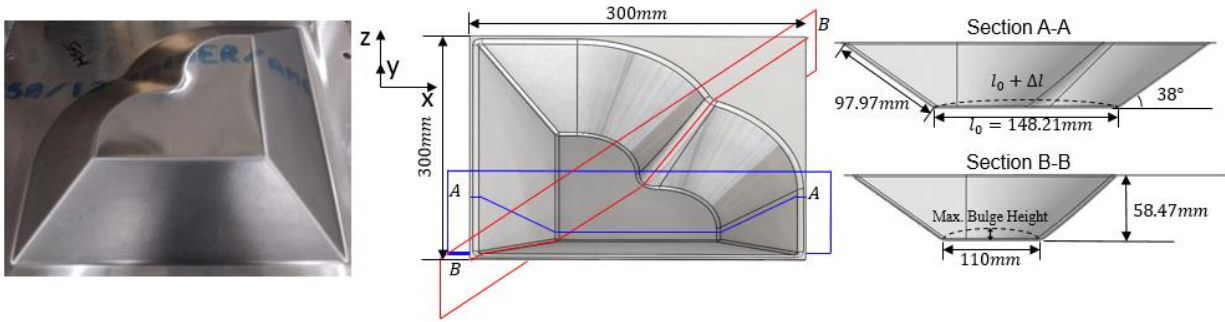
Figure 5.4 Detailed description of the geometry for the heart shape

5.2.3. Selection of the parameters to be used in developing the analytical model

To develop an analytical model for the prediction of thinning and bulge in ISF parts, it is required to select categories of parameters that influence thinning and bulge. Based on the previous chapters' results, it was observed that process parameters influence thinning of the formed part, and differences between the target thinning and the actual one are caused by surface features such as scallops. The following paragraphs describe how these two categories of parameters are accounted for in the analytical model.

Process parameters

A set of process parameters are required to generate a toolpath for the ISF process. These are tool radius r, tool step-down size after each contour Δz, initial sheet thickness t_0 and part geometry. In the TPIF process, an additional parameter called squeeze factor is required as an input that defines the gap between the tool and the die surface during the part forming. The contribution of each of the process parameters is summarized in the following paragraphs.

The tool shape and diameter: The tool shape and diameter tend to influence the maximum achievable wall angle and the part's surface quality. It is generally accepted that a smaller tool tends to yield a higher wall angle, as observed by Bhattacharya et al. [81]. In this work, a hemispheric tool with a radius r of 4mm is used. These values were chosen considering the tool

radius to sheet thickness ratio and the heart's geometric constraint. The tool radius to sheet thickness ratio allows some correlation to the material's optimal formability, as summarized in Duflou et al. [82]. It was further shown by Al-Ghamdi et al. [83] that the ratio has to exceed the value of 2 wherein this work the ratio is of 2.45.

Programmed squeeze factor and effective squeeze factor: The effect of the squeeze factor can be observed in the two point incremental forming (TPIF), where the presence of the backing die allows the tool to squeeze the material additionally. By definition, it is the amount of material that is squeezed beyond the amount stated by the sine law, which is calculated based on the material conservation. While one can try to program the squeeze factor into the tool path, the CNC setup's compliance deters from achieving the designed squeeze factor in the actual process. In this work, the squeeze factor will be categorized into two different quantities: the programmed squeeze factor *PSF* and the effective squeeze factor *ESF*. PSF is the amount of material programmed to be squeezed between the forming tool and die in the tool path, and it is calculated using Equation (5.1). The ESF at any instant can be calculated using Equation (5.2) which considers the compliance Δ, which is the summation of tool deflection and machine compliance. The *ESF* will always be less than *PSF* since the numerator in the negative term is larger. Thus, less material will be squeezed between the tool and die than expected. Empirical relations to estimate machine compliance and tool deflection are produced based on forces later employed to calculate Δ.

$$PSF = \left(1 - \frac{d}{t_0 \sin d(90 - \alpha)}\right) \times 100 \tag{5.1}$$

$$ESF = \left(1 - \frac{d + \Delta}{t_0 \sin d(90 - \alpha)}\right) \times 100 \tag{5.2}$$

where d is the squeezed thickness, t_0 the original thickness, and α the wall angle.

Step-down size: The *step-down size* is one of the process parameters that influence the formability

and the roughness of the surface. It has been generally accepted that a smaller step-down size results in increased formability, but further research is need since there have been conflicting reports of its influence, as summarized by Gatea et al. [84]. The step-down size Δz of 0.5mm and 0.63mm was selected based on the prior experimental results with the same material and tool diameter.

Formed part surface features

It has been found that during incremental forming, a periodic surface profile develops in the walls due to the repeated motion of the tool. These repeated profiles take the shape of the portion of the tool with which they are in contact. The partial arcs are named scallops for their similarities to the sea scallop outline. Several studies have been conducted to determining the surface roughness that arises [85] in a general sense.
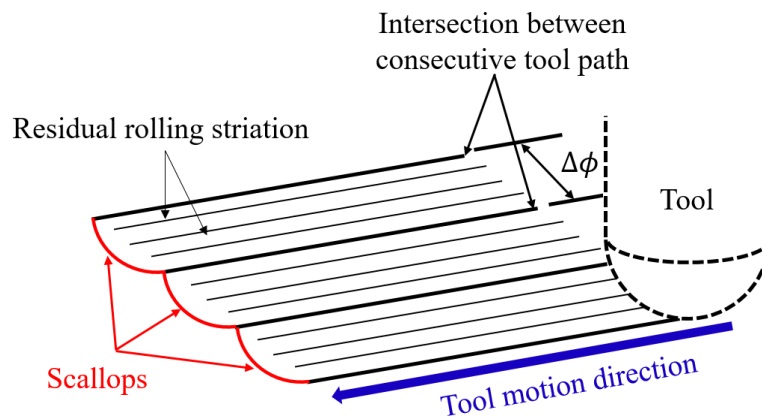
Figure 5.5 Schematic scallop formation at the intersection between consecutive tool path where the length of the scallop is proportional to the step-down size

While a qualitative relationship has been made between the process parameters and the material behavior, it has been challenging to make the connection quantitatively. However, a close-up examination of the surface and its formed geometry provides a clue to connecting each of the process parameters with the material behavior. Based on previous work [78], the periodic scallop

profile was broken down and analyzed to understand the connection between the process parameter and a single period of the scallop. As seen in Figure 5.5, as the material goes through deformation during the forming process, the tool leaves striations parallel to tool movement. These striations are due to the tool plowing through the material locally on the sheet's surface while the material underneath gets deformed globally.

The shape and location of the scalloped surfaces have a direct correlation with the process parameters. The distance between the peaks created by the intersecting tool $\Delta\phi$ is given in Equation (5.3) which is influenced by the step-down size Δz and the wall angle θ.

$$\Delta\phi = \frac{\Delta z}{\cos(\theta)} \tag{5.3}$$

The tool is positioned in the tool path so that the distance between the tool and the die would be equal to the sine law thickness. Ideally, the tool position ensures that the sheet is constrained so that the deformation would occur based on the volume conservation. The scalloped surface's horizontal axis would be located based on the sine law, and that any offset to the center in the direction of the sheet would induce a positive squeeze factor. A higher squeeze factor will result in the scalloped profile being further away from the ideal sine law profile than a tool path with a lower squeeze factor.
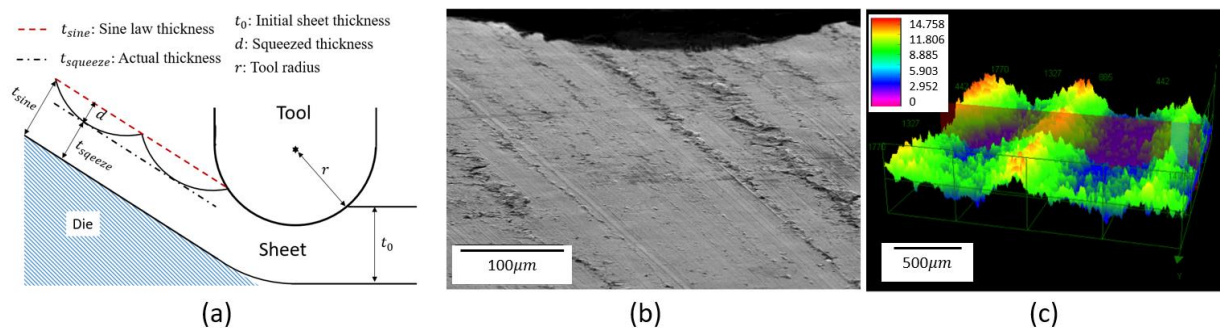
Figure 5.6 (a) Relationship between scallop position and squeeze, (b) experimental measurement of the surface profile using Tescan Mira3 FEG-Scanning Electron Microscopy (SEM), and (c) profile of the scallops measured using an Olympus DSX510 Optical Profilometer

The following connections can be made to summarize the relationship between the scalloped surface and the process parameters. The wall angle, sheet thickness provide a thresh hold profile based on the ideal sine law. The tool shape and size shape the surface profiles with each consecutive pass of the tool, creating a scalloped surface. The step-down size influences how wide each of the scallops should be or how far apart the scallop peaks should be. Finally, the squeeze factor defines how much the scalloped surface is offset from the ideal sine law profile. Figure 5.6 provides the measurements of the surface profile for a step-down size of 0.5mm. It can be seen in Figure 5.6 (b) that the cross-sectional profile of the scalloped surface resembles an arc that is from the hemispheric tool geometry. A hemispheric tool with a larger radius would result in the scallop with a larger radius of curvature, while a tool with a small radius would result in a smaller radius of curvature.

As the forming progress, the formed section can either obey or disobey the material conservation depending on the combination of process parameters. When material conservation is not observed in the formed wall section, when the wall section is too thin, volume difference is accommodated in the undeformed section, which results in the bulge. Knowing the exact profile of the formed surface and its location allows one to accurately calculate the geometry of the formed section and the undeformed section by using the accumulated material to calculate the bulge.

5.3. Segmentation based analytical model for thickness calculation based on material movement

5.3.1. Knowledge extraction from the TPIF finite element modeling

In the previous chapter, a finite element model was created to predict the surface profiles generated during incremental forming and was validated against experimental measurement. With the heart shape with its large part size where the straight edge is 300mm, it is difficult to sufficiently bring

down the mesh size to have acceptable computational cost while retaining prediction accuracy. If the element size is too big, the element will not portray the tool's curvature, and the prediction result would be inaccurate. Thus, a segmented strip finite element model was created where the domain of the model was a small narrow strip that was cut from the original global model. The segmented part was meshed finely to have the element resolution necessary to achieve model accuracy. This model was able to accurately predict the surface profile that occurs during the incremental forming. The symmetry condition was applied to the segmented strip model to simulate the global model's boundary condition. The details of the model can be found in the previous chapter. Figure 5.7 shows the result of the global simulation and segmented strip simulation.
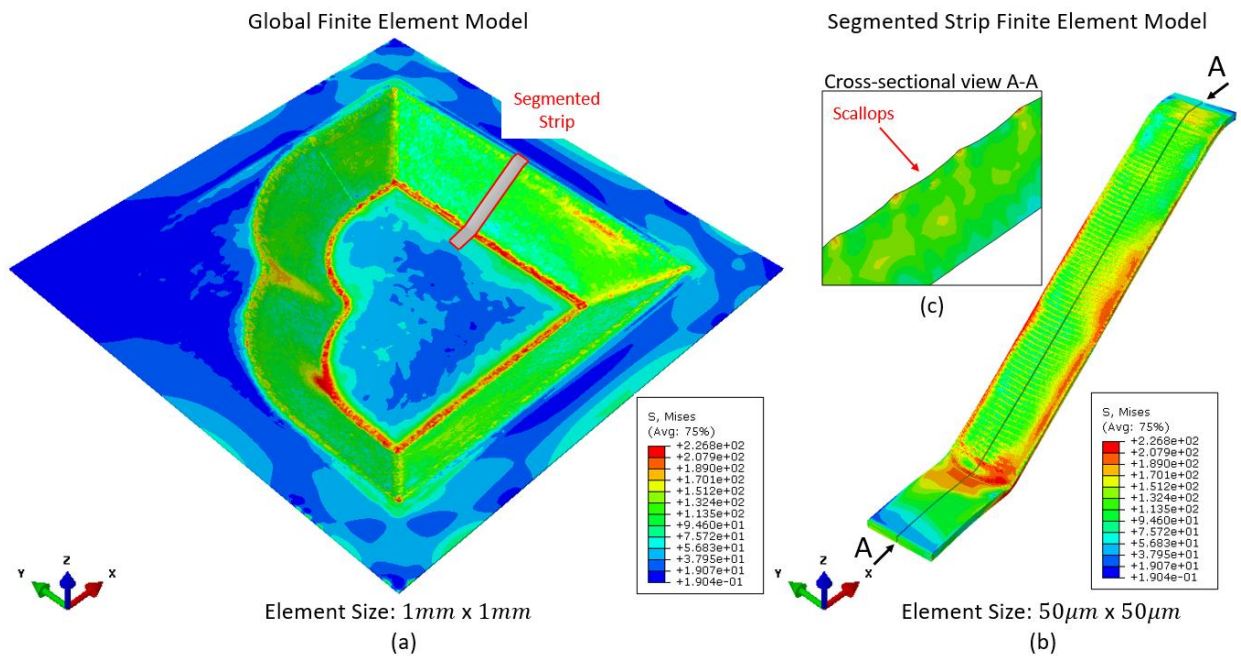
Figure 5.7 (a) a global FEM model of the heart, (b) a segmented strip FEM model of the heart, and (c) the close up of the cross-section A-A of the segmented strip finite element model

The surface profiles predicted in the segmented strip finite element model were compared with the experiment. While the finite element model provided a good prediction of the surface

profile, it was not easy to extrapolate the method to the whole part since applying the segmentation approach in the whole global domain in the finite element model was costly. However, suppose the calculation is conducted for all of the segmented strips in the domain. In that case, it is possible to have an accurate prediction of the surface profile and material movement for the full 3-D geometry. Thus, an analytical model was developed as an alternative to the finite element models to calculate the surface profile. This analytical model depends on the relationship between the surface profile and the process parameters found in the previous section.

5.3.2. Principle of segmentation based analytical model scheme

The segmentation scheme that produces the segmented strips plays a crucial role in the analytical model. The target geometry can consist of concave, convex, and flat shapes. The goal of the segmentation scheme is to have a sufficient number of strips that make up the part such that any curvature change within the strip in the width direction can be approximated to zero. Next, it is possible to conduct another segmentation in the lateral direction and isolate each of the scallops in each strip. As a result, the strip's final segmented element will contain one scallop, each containing multiple nodes that express the scallop's surface profile. Each scallop in the strip will align with the scallops in the consecutive strip since all of the segmented strips will contain the same number of scallops. This allows easy assembly of the point cloud data to a 3-D profile.
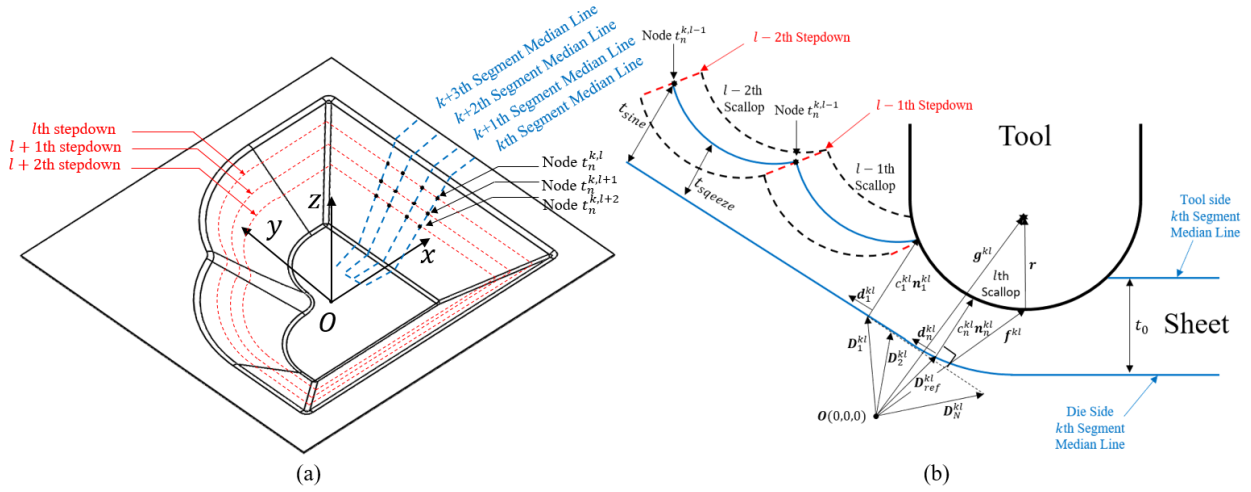
Figure 5.8 Scheme for longitudinal segmentation (a) and the scheme for lateral segmentation with relevant vectors for calculation of the formed geometry (b)
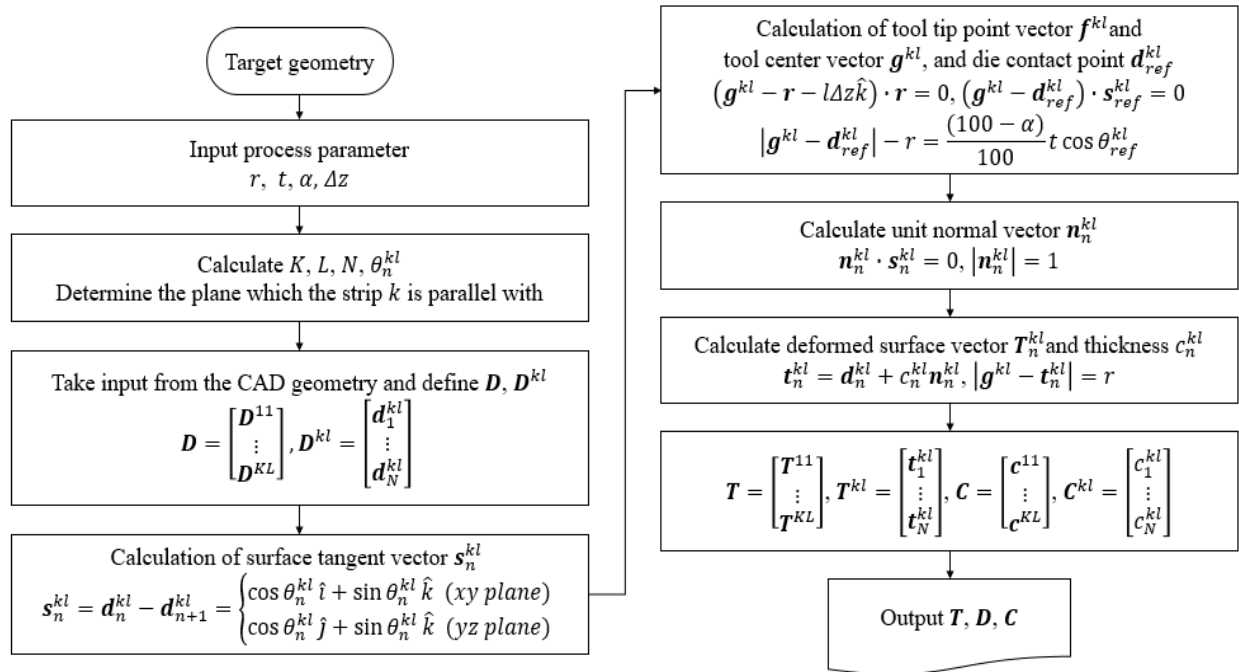
Figure 5.9 Algorithm for 3D geometric discretization based on the multi-scale analytical model

The outline of the algorithm for the segmentation-based analytical model is provided in Figure 5.9. The algorithm requires the following inputs; process parameters for incremental forming, including tool radius r, sheet thickness t, squeeze factor α, and step-down size of Δz and

the geometry data consists of point cloud data of coordinates that make up the target geometry. A preprocessing of the geometry data allows one to obtain the number of segmentation required in each direction and the number of nodes in the element for an accurate description of the surface. Based on these values, it is possible to calculate the interval in the lateral direction that the segmentation should be conducted. First, segmentation is done in the lateral direction along the wall to create a K number of the longitudinal strips. Next, a secondary segmentation is conducted in the longitudinal direction to create an L number of discretized segments containing only one scallop. The number of discretized segments L would correspond to the number of step-down, which can be calculated by dividing the total depth by step-down size Δz. Each strip will contain an N number node that will make up the scalloped surface. In total, $K \times L$ number of discretized segments are required to express the geometry of the part entirely. The algorithm calculates the part's final geometry based on the inputs and outputs the necessary nodal coordinates. Finally, by assembling the profile from all segmented strips, a full 3D profile of the formed geometry can be obtained.

The following steps are taken for calculating the nodal coordinates for the die side and tool side profile after forming. The die side represents the surface that is in contact with the die. Thus, an assumption will be made that the die side surface will be flush with the die. First, from the input point cloud data, die side nodal coordinate vectors $\boldsymbol{d}_n^{kl}$ are calculated. The superscript k and l corresponds to the kth strip, lth scallop, while the subscript n denotes the nth nodal point in that kth strip, lth scallop. From it, $\boldsymbol{D}^{kl}$ and $\boldsymbol{D}$ can be generated a matrix which contains nodal information for a discretized element in kth strip lth scallop and a matrix containing nodal information for the whole geometry. The detailed representation of the relationships is shown in Equation (5.4).

$$D = \begin{bmatrix} \boldsymbol{D}^{11} \\ \vdots \\ \boldsymbol{D}^{KL} \end{bmatrix}, \ \boldsymbol{D}^{kl} = \begin{bmatrix} \boldsymbol{d}^{kl}_1 \\ \vdots \\ \boldsymbol{d}^{kl}_N \end{bmatrix} \tag{5.4}$$

From the die side profile data, surface tangent vector $\boldsymbol{s}^{kl}_n$ for each node can be calculated according to Equation (5.5)

$$\boldsymbol{s}^{kl}_n = \boldsymbol{d}^{kl}_n - \boldsymbol{d}^{kl}_{n+1} = \begin{cases} \cos\theta^{kl}_n \hat{i} + \sin\theta^{kl}_n \hat{k} & (x - z \ plane) \\ \cos\theta^{kl}_n \hat{j} + \sin\theta^{kl}_n \hat{k} & (y - z \ plane) \end{cases} \tag{5.5}$$

where $\boldsymbol{s}^{kl}_n$ is the surface tangent vector for the kth strip, the lth scallop, and the nth node, which is the difference between the nodal point for the nth node and the $n+1$th node, which can also be expressed in terms of the wall angle θ^{kl}_n obtained by similarly conducting calculations.

The tool tip point vector $\boldsymbol{f}^{kl}$ for the kth strip, the lth step-down is displaced from the tool center point vector $\boldsymbol{g}^{kl}$ by the amount of tool radius in the z-direction. This satisfies the following relation $\boldsymbol{f}^{kl} + \boldsymbol{r} = \boldsymbol{g}^{kl}$ where $\boldsymbol{r}$ is the vector point upward in the z-direction with the magnitude of tool radius. The z coordinate of the tool tip will be constrained because it corresponds to the lth number of step-down. The z coordinate for the tool tip will have the value of $l\Delta z$. Since the tool has to contact the sheet tangentially, the surface tangent vector $\boldsymbol{s}^{kl}_{ref}$ and the coordinate vector $\boldsymbol{d}^{kl}_{ref}$ can be defined on the tool surface. Also, for every node on the tool side surface, the surface tangent vector $\boldsymbol{s}^{kl}_n$ and the coordinate vector $\boldsymbol{d}^{kl}_n$ will be defined in the same way. Since the number of nodes in the element is large enough, there will be an arbitrary node n on the tool side surface, which will be close enough to the tool contact point so that $\boldsymbol{s}^{kl}_{ref}$ and $\boldsymbol{d}^{kl}_{ref}$ can be replaced by $\boldsymbol{s}^{kl}_n$ and $\boldsymbol{d}^{kl}_n$. Since the sheet surface and the tool are tangent to each other, the vector pointing from the contact point to the tool center will be normal to the sheet surface, and its magnitude equal to the sum of the sheet thickness and the tool radius. These three constraints provide three equations and

109

three unknown to solve for to obtain the tool center point and its corresponding contact point, as shown in Equation (5.6)

$$
\begin{aligned}
\left(g^{kl} - r - l\Delta z \hat{k} \right) \cdot r &= 0 \\
\left(g^{kl} - d_{ref}^{kl} \right) \cdot s_{ref}^{kl} &= 0 \\
\left| g^{kl} - d_{ref}^{kl} \right| - r &= \frac{(100 - \alpha)}{100} t \cos \theta_{ref}^{kl}
\end{aligned}
\tag{5.6}
$$

where the first equation is the constraint in z coordinate, second the vector equation representing the normal vector, and the last regarding its magnitude with $\frac{(100-\alpha)}{100} t \cos \theta_{ref}^{kl}$ being the thickness based on material conservation and squeeze factor α.

For each of the node points, the unit normal vector n_n^{kl} can be defined which is perpendicular to the s_n^{kl} and have a magnitude of 1. It can be calculated using Equation (5.7)

$$
\begin{aligned}
n_n^{kl} \cdot s_n^{kl} &= 0 \\
\left| n_n^{kl} \right| &= 1
\end{aligned}
\tag{5.7}
$$

where n_n^{kl} is the unit normal vector, s_n^{kl} the surface tangent vector. Using the unit normal vector n_n^{kl}, it is possible to calculate the top surface coordinate for each of the nodes t_n^{kl}. The t_n^{kl} will be a point on the tool surface since the sheet and the tool is in contact and displaced by the amount of thickness from the die side node position in the direction of its normal vector, which can be expressed as

$$
\begin{aligned}
t_n^{kl} &= d_n^{kl} + c_n^{kl} n_n^{kl} \\
\left| g^{kl} - t_n^{kl} \right| &= r
\end{aligned}
\tag{5.8}
$$

where the t_n^{kl} denotes the tool side nodal coordinate vector corresponding to d_n^{kl} and n_n^{kl}, with the constant for thickness c_n^{kl}. Finally, the matrices that denote the values of the strip and the whole part can be generated as shown in Equation (5.9)

$$T = \begin{bmatrix} T^{11} \\ \vdots \\ T^{KL} \end{bmatrix}, \; T^{kl} = \begin{bmatrix} t_1^{kl} \\ \vdots \\ t_N^{kl} \end{bmatrix}, \; C = \begin{bmatrix} C^{11} \\ \vdots \\ C^{KL} \end{bmatrix}, \; C^{kl} = \begin{bmatrix} c_1^{kl} \\ \vdots \\ c_N^{kl} \end{bmatrix} \tag{5.9}$$

where T^{kl}, C^{kl}, T, and C denote the tool side surface profile and thickness for kth strip lth scallop and the whole part, respectively.

5.3.3. Validation of the segmentation based analytical model

Prediction of scalloped profile

The segmentation-based analytical model was implemented as an in-house program using the Matlab environment. The Matlab program takes initial process parameters and geometrical information as inputs. Based on the algorithm described in Figure 5.9, the bottom profile, tool center point, projection of the tool surface, and finally, the top profile is calculated sequentially. The prediction of the geometry and thickness distribution is outputted as a result of the program. The validation of the model was conducted at three different levels. First is the validation of the generated individual scalloped profile by comparing them to the profilometer measurements. Two different heart shape cases, each with a different combination of the process parameters, were compared to test the model's capability to predict the scalloped profile. Next, the 2-D cross-sectional profile of the heart shape from a single segmented strip is compared with the laser scanner measurements to validate the model's ability to consider the geometric boundary conditions. Finally, a comparison between predicted and measured full 3-D geometry is conducted to show its prediction capacity.

The heart shape was formed with two different combinations of process parameters. The first combination had a step-down size of 0.5mm and an effective squeeze factor of 1.74%, while the second combination had a step-down size of 0.63mm and an effective squeeze factor of 1.21%.

The other process parameters were kept the same. These include a tool radius of 4mm, initial sheet thickness t_0 of 1.63mm, and the part geometry data. The experimental measurement of the surface profile was taken using an Olympus DSX510 profilometer in three consecutive heart regions that exhibit identical geometrical conditions. The measured data was centered to allow easy comparison, as shown in Figure 5.10.
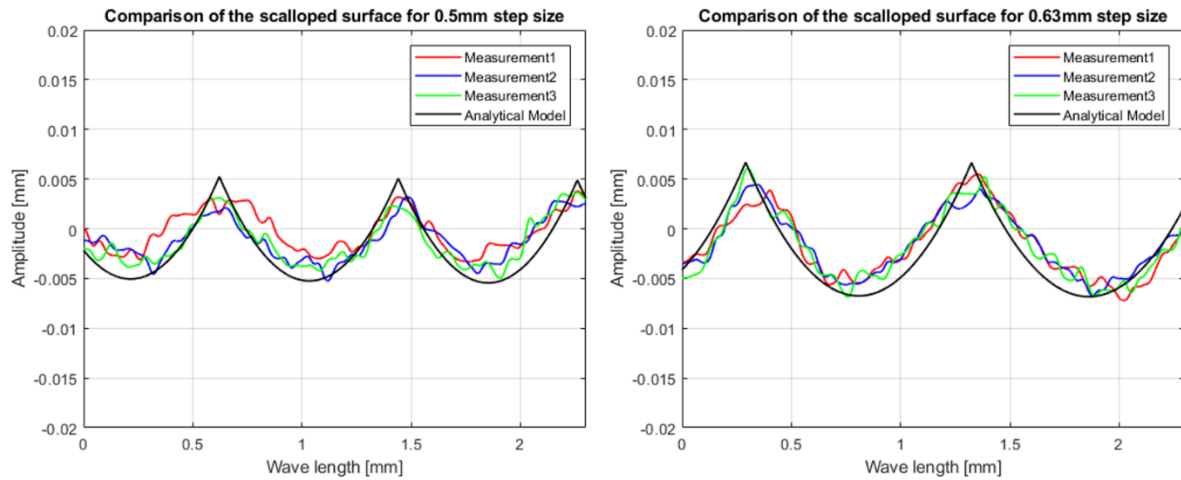
Figure 5.10 Comparison of the scallops between three measurements and the analytical model for Δz = 0.5mm, α=1.74% (left), and Δz = 0.63mm, α=1.21% (right)

Table 5.7 Comparison of the Peak to Peak and Peak to Valley values between the measurement and the model

	Δz = 0.5mm, α=1.74%		Δz = 0.63mm, α=1.21%	
	Wavelength (μm) (Peak-Peak)	Peak-Valley (μm)	Wavelength (μm) (Peak-Peak)	Peak-Valley (μm)
Measurement 1	814.8	7.34	955.1	12.66
Measurement 2	833.0	8.39	1019.9	10.67
Measurement 3	781.5	8.63	1085.3	10.07
Measurement Ave.	809.8	8.12	1020.1	11.13
Analytical Model	819.2	10.30	1033.4	13.40

The primary quantities that were analyzed were the overall shape of the scalloped surface profile, the peak to peak length (wavelength), and the peak to valley length (twice amplitude). The exact values for the measured and predicted values are described in Table 5.1. The overall shape of the modeled result's surface profile was in good accordance with the measured profile.

The average measured wavelength of the scallop in the case of step-down $\Delta z = 0.5$mm was 809.8 μm while step-down $\Delta z = 0.63$mm resulted in the value of 1020.1 μm. The corresponding modeled lengths were 819.2 μm and 1033.4 μm resulting in the prediction error of 1.15% and 1.29%. The scallop height is defined as the distance between the peak and the valley of the scallop, which is equal to twice the amplitude. The average height for the scallop for the step-down of $\Delta z = 0.5$mm was 8.12 μm while the step-down of $\Delta z = 0.63$mm resulted in 11.13 μm. The modeled values were 10.30 μm and 13.40 μm, resulting in the prediction error of 21.17% and 16.94%. The step-down of $\Delta z = 0.5$mm resulted in a higher error in predicting the scallop height because one of the measurement data had a considerably lower scallop height value than the other two. Considering two data with higher value while excluding the outlier led to the average scallop height of 8.51μm and the prediction error of 17.38%.

It was observed that the analytical model had a sharper peak compared to the experimental peak. The shaper peaks in the model are caused by the way the peaks are generated. The peaks are the intersecting point between the profile created by the movement of one tool and its subsequent tool path profile. The model considers the theoretical intersection of the profiles, which creates a peak with a sharper edge. In reality, the peaks get blunted by the inability of the material and the tool to behave perfectly. Similar prediction error in both cases suggests that this is the reason for the model's systemic error, which over predicts the peak height by around 17%. It can be concluded that the analytical model can reasonably predict the surface scallop profile for various process parameters.

2-D prediction of part geometry for heart shape using the analytical model

Based on the validation of the surface scallop profiles, it can be said that the analytical model can capture the scalloped profile created during the incremental forming process. Thus, a

subsequent validation is conducted for the 2-D cross-sectional profile to prove the model's ability

to scale up from individual scallops to a segmented strip. The profile in the flat region of the heart

is selected for comparison, which corresponds to section A-A of the heart in Figure 5.4.
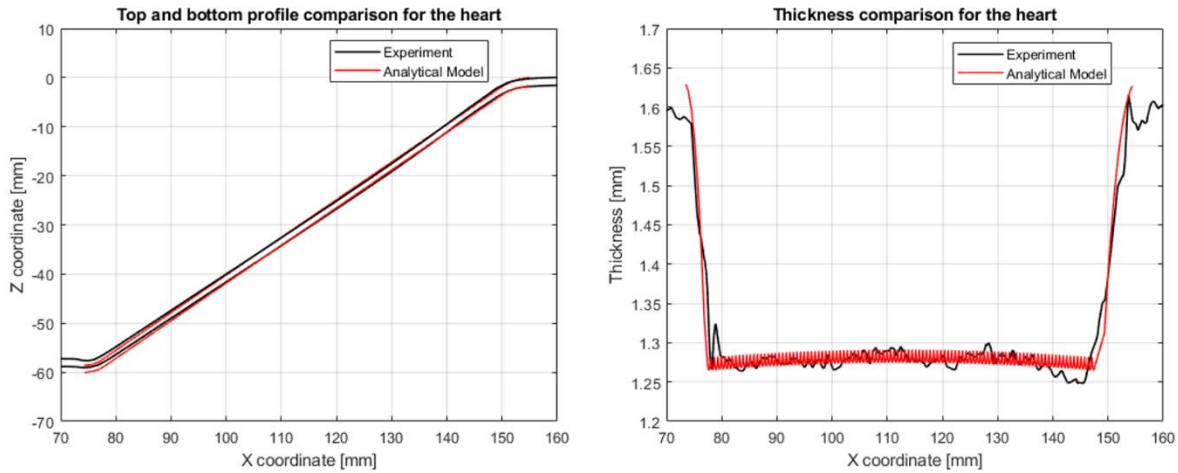
Figure 5.11 Top and bottom profile comparison (left) and thickness comparison (right) of the
heart between the experiment and model

Figure 5.11 shows the comparison of the profile and thickness between the experimental

measurement and the analytical model. It can be seen from the profile comparison that the

experimental and modeled top and bottom profiles are in good accordance with each other. The

one section that the modeled data deviates from the experiment is the fillet region at the bottom of

the heart. The experimental profile is slightly lifted at the bottom. This lift seems to be due to the

springback that occurs after the part was created. While the AA7075-O exhibits minimal

springback, it is noticeable, as shown in the graph, since the model does not consider springback.

As for the thickness distribution, the x-axis of the thickness plot coincides with that of the

geometric profile plot. It can be seen that the analytical model, which is built based on the scalloped

surface, is capable of expressing the fine scallop surface details, which are visible as fine waves in

the thickness plot. The experimental measurement cannot show the fine scallop because the laser

scanner's scanning resolution, which is 63μm, is not fine enough to detect the height difference of the scalloped surface. However, the general shape of the thickness distribution shows a good correlation.

Analysis of the accuracy and computational cost of the analytical model

The prediction errors were defined to analyze the accuracy of the prediction of the geometry and thickness. The errors were calculated based on the absolute average values to condense the error distributed throughout the part into a single representative value. The percent error for the geometry was calculated as the ratio of the absolute average deviation to the part's depth, representing how much the part would deviate from the target geometry. The percentage error for the thickness distribution is calculated as the ratio of the absolute average deviation to the maximum deformed thickness. This error would represent the upper limit of the thickness error that is induced by the forming process.

The error values for predicting the geometry and thickness of the heart shape are shown in Figure 5.12. The maximum value of deviation in the geometry occurred in the flange region, where the deviation was around 963 μm. The maximum deviation of geometry in the flat wall region was around 400 μm. It can be seen that a larger deviation occurs in the wall near the flange section of the part where the sheet is being clamped compared to the steady-state flat wall section. This large deviation in the fillet region is due to the springback and lack of support from the clamp. Near the bottom of the heart, the clamps that hold the sheet in place are too far to provide sufficient support, leading to deviation in geometry. The thickness distribution had near-zero deviation in most regions with around 100 μm deviation only at the flange region.
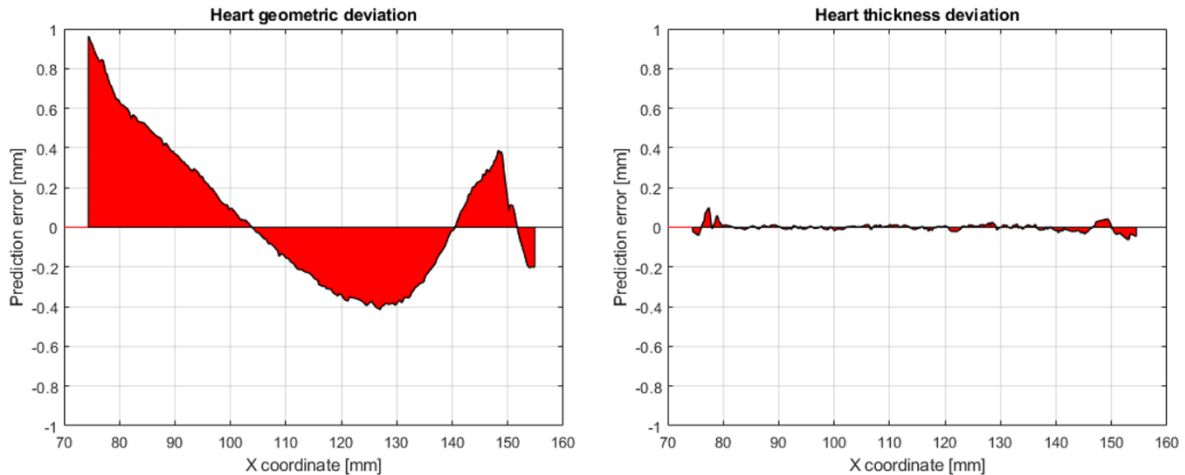
Figure 5.12 Deviation of the geometry (left) and the thickness (right) for the heart

It can be seen that around 1~2% error occurred for the geometry prediction. The error value seems to make logical sense considering the amount of deviation is less than 1mm. In thickness distribution, a percentage error of 6.10% was observed. While the heart is more complicated than a simple cone due to a mix of concave and convex geometry, it is still simple compared to commercial parts. Thus, a follow-up study with more complex geometry is in progress to provide expected deviations for complex commercial parts.

Based on the observations and calculations, the upper bound for the errors is established, which can serve as a guideline for model accuracy. The geometric prediction errors of less than 1mm are considered satisfactory. For the thickness prediction, an error of less than 200μm would be regarded as acceptable. It could be preferable to exclude the errors found in the flange section or the undeformed region that happens to be the region that contains the maximum prediction errors in many cases. Excluding the flange could result in a more accurate prediction since the flange section can contain errors from springback, which will be trimmed away in many cases.

Table 5.2 Statistical analysis of the deviation of the prediction

	Category	Maximum error (mm)	Average absolute error (mm)	Percentage Error (%)
Heart	Geometry	0.9631	0.3338	1.93%
	Thickness	0.0995	0.0140	6.10%

The computational cost of the analytical model was calculated to make a comparison with the numerical model. The baseline for the computational cost of the FEM model was set by conducting the calculation using 120 cores of 2.8 GHz Intel Zeon E5-2780v2 processors. It can be seen that the analytical model was able to predict geometry and thickness with reasonable accuracy, with less than 1% of the computational cost required for the FEM model, as shown in Table 5.3.

Table 5.3 Computational cost comparison between FEM model and analytical model

	Computation Cost	
	FEM Model (120cores)	Analytical Model
Heart (full)	43.51 hour	0.030 hour
Heart (Partial)	5.01 hour	0.001 hour

5.4. Principle of weighted summation for bulge prediction

In Chapter 4, a quantifiable explanation for the bulging phenomenon was established based on the material movement during incremental forming. If the formed geometry achieves the ideal geometry where it observes volume conservation, there would be no bulge. However, since incremental forming is an accumulation of deformation and each revolution of the tool achieves incremental deformation, it is difficult for the formed surface created during each revolution to observe the volume conservation. The difference between the formed geometry and ideal geometry is pushed forward during forming and accommodated in the undeformed section. The 2-D bulge was approximated to a beam buckling model and validated against the experiment based on material movement calculation.

The ability to predict bulge profiles in the undeformed region allows one to tune the process parameters to minimize the amount of bulge. However, this requires a reliable bulge prediction model which can consider different process parameters. The conventional approach to predicting the bulge relies on the finite element method (FEM). The bulge prediction accuracy depends on the model accuracy, which is greatly influenced by the element size. However, it is challenging to have a high-resolution model with a small element size while having an acceptable computation cost. Thus, a novel analytical model is proposed to predict the 3-D bulge profile based on a weighted summation method based on the material movement calculated by the segmentation-based analytical model. The effect of process parameters and part geometry will be consolidated by the segmentation-based analytical model into material movement at the boundary as the boundary condition. A shape function is introduced in the scheme, which remains uniform regardless of different squeeze factors for given geometry to serve as a baseline bulge profile. Based on the derived shape function, the 3-D bulge profile is calculated based on the weighted summation method. The final result is compared with the experiment and validated.

5.4.1. Shape function for weighed summation based analytical model

A shape function is introduced to account for the shape of the profile at an arbitrary location. This shape function provides a baseline function that will be scaled and translated based on the node's location that makes up the region of interest. Different analytical functions were introduced to find a fit between experimental shape functions. The investigated shape functions include the sine function, 2nd order polynomial function, and ellipsoidal function. The comparison was made between the experimental bulge profile and different shape functions by normalizing the bulge's height to 1 and the bulge's width to 2, with the origin at the middle, as shown in Figure 5.13 (a).

Among different convex functions that qualify for shape function, the polynomial function with varying degrees seems to be the most suitable candidate for the shape function. The varying degree of polynomial allows the shape function to accurately portray the experimental shape of the bulge while allowing easy integration for calculation of the length of the arc. The shape function plays a crucial role in calculating the bulge height based on the base length and the additional material being pushed in during the forming operation. Depending on what the shape function looks like, a different amount of additional material is required from that shape, as seen in Figure 5.13 (b). The ellipsoidal function with the base length of 100mm requires almost two times more additional material to achieve the same height of bulge than the 2nd order polynomial or sine function.

The normalized bulge shape function for TPIF cone 67° with 0% and 2.54% effective squeeze shows that they have the same shape function. It can be observed that the shape function depends on the part's geometry and not on the squeeze factor. The shape of the geometry, such as wall angle and tool shape, imposes a boundary condition on the edge of the undeformed section—any addition of material results in the bulge with a similar shape but scaled by a constant.
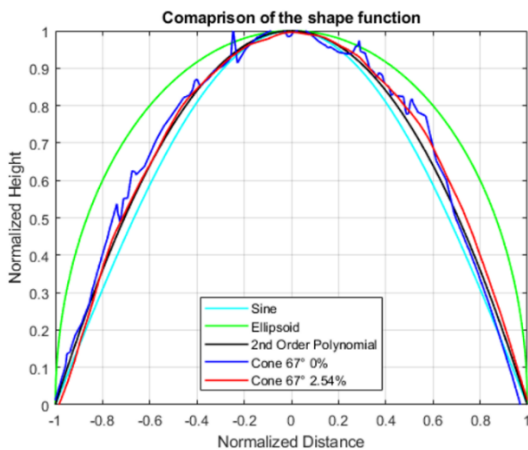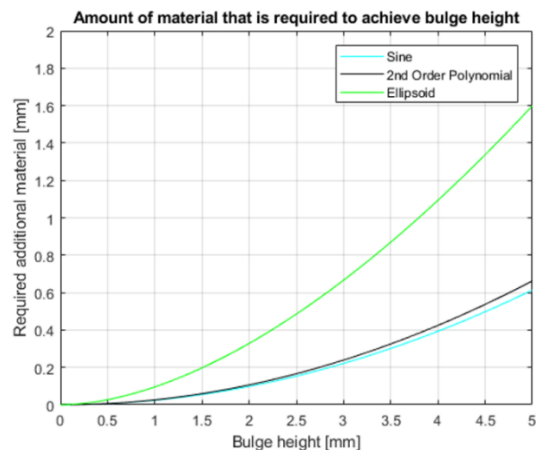
(a)   (b)

Figure 5.13 Various shape function for cone 67° (a) Comparison of various shape function versus cone 67° bulge profile, and (b) calculation of required material for achieving bulge height based on a base length of 100mm

5.4.2. Principle of weighted summation scheme for the calculation of bulge height

In the previous chapter, a bulge prediction method was presented based on approximation of the 2-D profile as beam buckling where the profile with the added material had to bend and buckle to fit the given geometric constraint. While this 2-D approximation method provided some understanding in predicting the 2-D bulge profile, it is difficult to expand to predicting the 3-D bulge profile. It was observed based on cross-section analysis that depending on where the node is located in the undeformed region, the shape of the calculated bulge can differ in the horizontal and vertical direction when applying the simple 2-D approximation. The prediction of a 3-D profile requires considering the effect of material movement in a continuum sense at all boundaries simultaneously between undeformed and deformed sections. Thus, a novel weighted summation method with the shape function is proposed to calculate the bulge height for each of the discretized nodes in the domain. The weighted summation method approximates the effect of the continuum while considering the different boundary conditions. The material accumulation is calculated using a separate algorithm and is not present in this work.

First, the undeformed region is represented by a finite number of nodes inside its boundaries. The n denotes the total number of nodes. For each node $N_i(x_i, y_i, 0)$ in the flat surface, has the corresponding $N_i'(x_i, y_i, h_i)$, the bulge profile. For each node, the vectors that are normal to the boundary are calculated where m denotes the total number of lines found to be normal to the boundary, as shown in Figure 5.14. For each jth vector, the corresponding line with the largest angle between the two lines is found. The sum of the two is inputted into the shape function as shown in Equation (5.10) to calculate the intermediate height h_j using the Equation (5.10)

$$h_j = f(l_j + l_k), \quad \arg \max g(\boldsymbol{l}_k) = \left\langle \boldsymbol{l}_k \middle| \boldsymbol{l}_j \cdot \boldsymbol{l}_k \right\rangle, \quad l_j = \left| \boldsymbol{l}_j \right| \tag{5.10}$$

where h_j denotes the intermediate height for jth pair, f the shape function, l_k the length of the vector $\boldsymbol{l}_k$ which pairs with $\boldsymbol{l}_j$ having the largest angle. To calculate the weights for the weighted summation method, the ratio of R_j is calculated for each jth line. This ratio allows the weights to emphasize the nodes that are closer to edges so that as the node approaches the edges, the height converges to zero. The ratio R_j is calculated using Equation (5.11)

$$R_j = \max(l_j, l_k) / (l_j + l_k) \tag{5.11}$$

where R_j is a ratio of the larger value of the pairs to the sum of the two. The final weight is calculated based on how much each of the ratios influences the intermediate height. Thus, weights w_j for each of the intermediate heights are calculated, as shown in Equation (5.12).

$$w_j = R_j / \sum_{j=1}^{m} R_j \tag{5.12}$$

Finally, the bulge height H_i is calculated as the weighted summation of the intermediate heights using the computed weights, as shown in Equation (5.13).

$$H_j = \sum_{j=1}^{m} w_j h_j \tag{5.13}$$
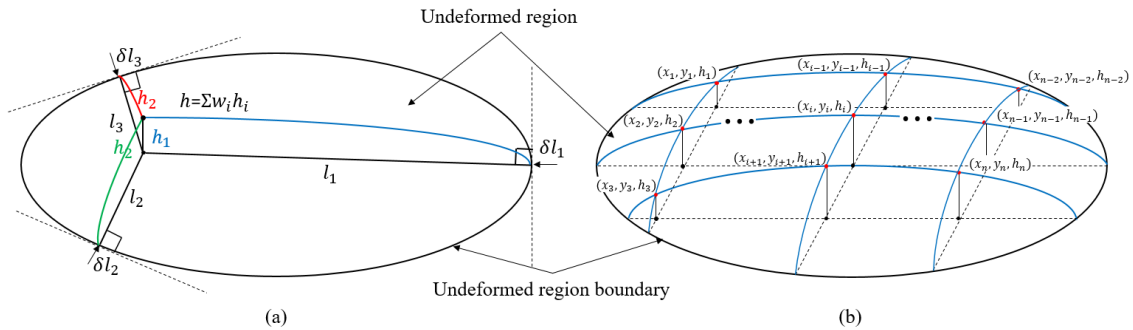
Figure 5.14 The diagram of the bulge calculated algorithm based on the weighted summation method (a) The weighted summation method based on the calculation of the intermediate height

values, and (b) discretization of the surface where the height at each node is calculated to obtain the full 3-D profile.
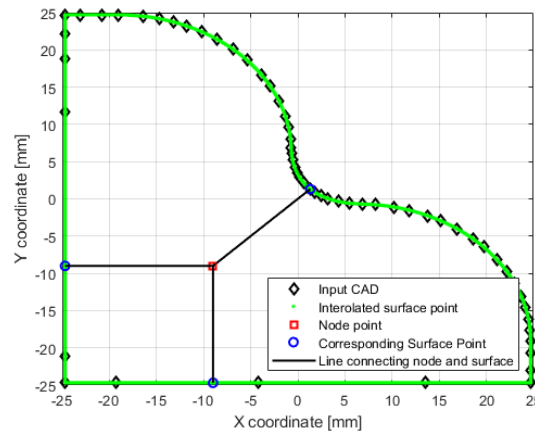
Figure 5.15 An example of the algorithm applied to heart shape

An example of how the algorithm is applied to the internal point in the heart is shown in Figure 5.15.

5.4.3. Validation of the weighted summation based analytical model for bulge prediction

Comparison of the modeled prediction and experimental measurements for Cone 67°

The predicted 3-D bulge profile of the analytical model is compared with that of the experimental measurement. Two cases for the 67° cone, one with 0% squeeze factor and the other with 2.54% effective squeeze, are investigated for model validation. The proposed algorithm is applied using the calculated normalized shape function. The node points within the undeformed region and its boundaries are calculated. The weighted summation method is then applied to calculate the local height at the corresponding location. Once the bulge height at each node is calculated, the 3-D surface is generated. Figures 5.16 and 5.17 show the comparison between the experimental 3-D profile and the modeled 3-D profile for 0% and 2.54%. The result shows that the predicted result is well matching with the experimental bulge profile.
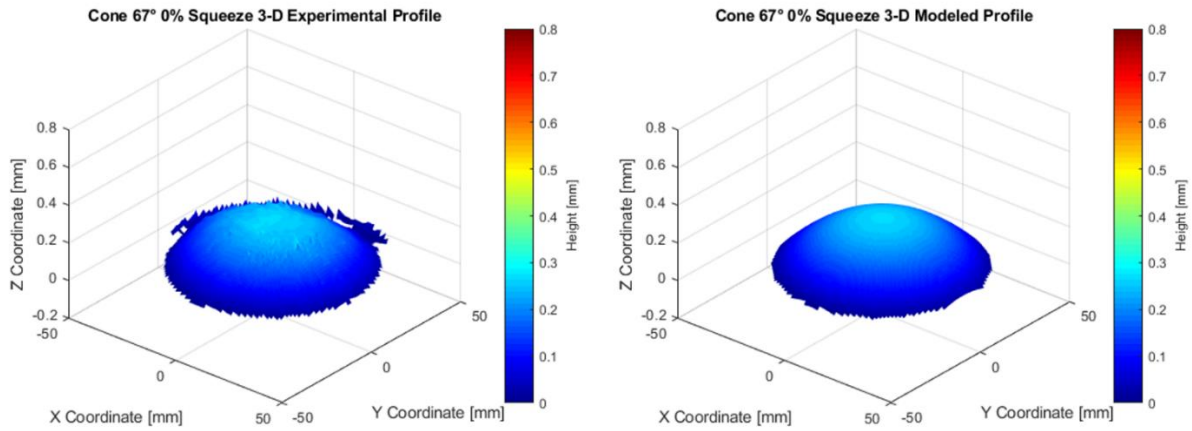
Figure 5.16 Comparison of the experimental and modeled 3-D profile for cone 67° 0% squeeze
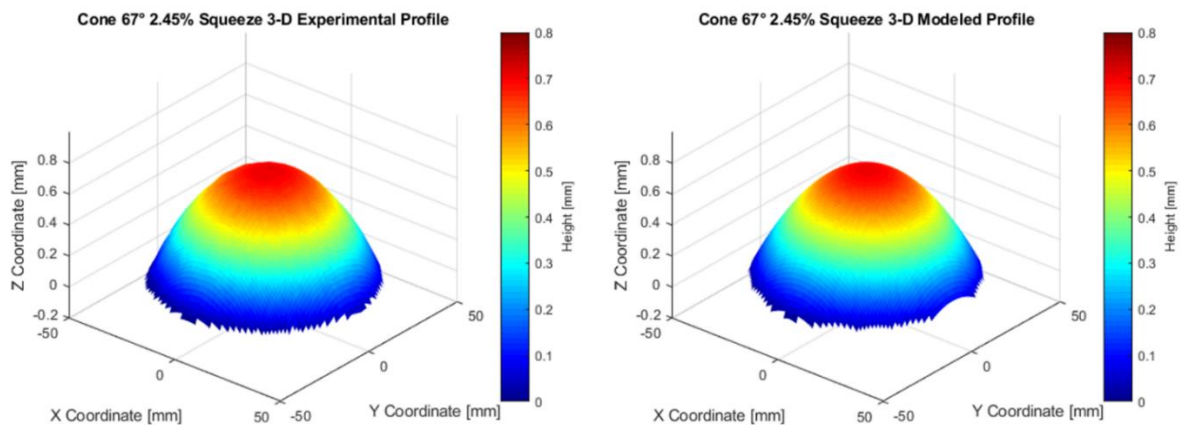
Figure 5.17 Comparison of the experimental and modeled 3-D profile for cone 67° 2.54% squeeze

To show a direct comparison between the experimental profile and predicted profile, the comparison is made between the cross-sectional profile of the surface represented by wireframes, as shown in Figure 5.18. The red lines represent the experiment, and the blue lines represent the predicted profile. The bulge profile spans from around -50mm to 50mm, and the exact end values differ due to preprocessing of the date where edges with fillets were trimmed off. The maximum height matches very well with the maximum height from the analytical prediction was 0.2626mm for the 0% squeeze and 0.7109mm for the 2.54% squeeze. The cone with the higher squeeze factor

of 2.54% resulted in a higher bulge because the higher squeeze factor resulted in more material movement at the boundaries.

Squared error (SE) values were calculated for each node point to check how much the modeled surface deviates from the experimental surface. The SE for 0% squeeze was 0.3860 while SE for 2.54% squeeze was 4.1015. Considering that a prediction that has the maximum height at peak point off by 0.1mm would result in the SE of around 20, and 0.05mm would result in the SE of approximately 10, the deviation in the predicted results can be considered minimal. The computational cost associated with the model was less than 5% of running the finite element model, where a typical finite element model of a cone would take around 20hours. In contrast, the analytical model finished within an hour. However, it is possible to increase the number of nodes within the undeformed region, resulting in a higher computational cost.
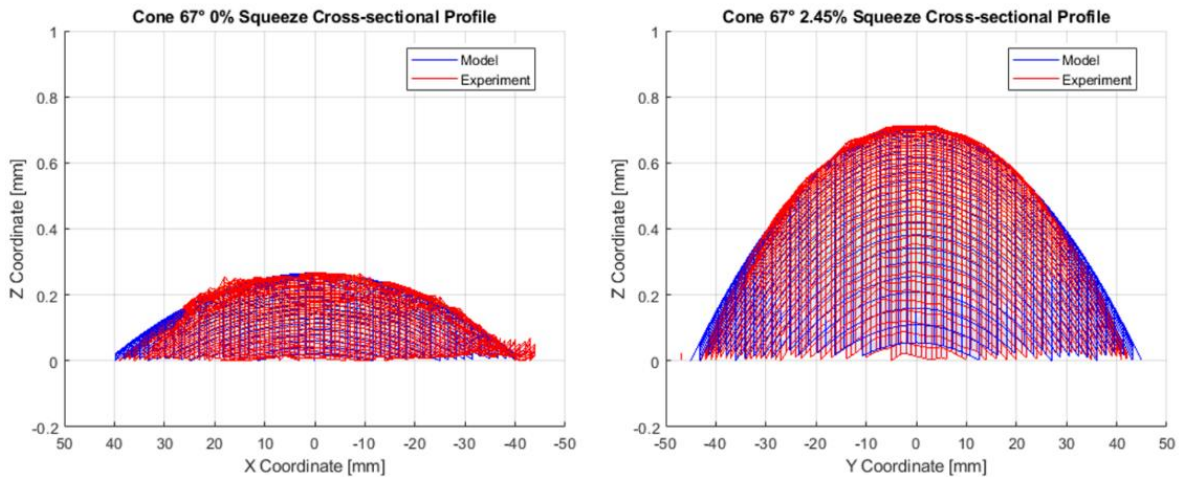
Figure 5.18 Comparison of the cross-sectional profile of the surface represented by wireframes where the blue color denotes the modeled surface and red denotes the experimental measurements

Comparison of the modeled prediction and experimental measurements for heart

The analytical heart bulge profile was compared to that of the experimental measurement to test the robustness of the analytical model. Four heart cases were investigated, combinations of

step-down size values of 0.5mm and 0.63mm, and programmed squeeze factor of 0% and 10%. The effective squeeze factor values for 0.5mm and 0.63mm are 1.74% and 1.21%, respectively. The amount of material being pushed into the undeformed region boundary is calculated from the segmentation-based analytical model. Each of the values for the predicted measured material movement is given in Table 5.4.

Table 5.4 Calculated material movement amount

	$\Delta z = 0.5$mm PSF = 0%	$\Delta z = 0.5$mm PSF = 10%	$\Delta z = 0.63$mm PSF = 0%	$\Delta z = 0.63$mm PSF = 10%
Experiment	0.0834mm	0.1253mm	0.0964mm	0.1189mm
Model	0.0855mm	0.1348mm	0.1073mm	0.1354mm

Using the calculated material movement amount, the weighted summation analytical model calculates the bulge profile in the undeformed section in the middle of the heart. The measured and predicted amount of material being pushed into the undeformed region seems to match well. The increase in the amount of material transfer amount was witnessed as an increase in the squeeze factor. The existence of material movement with 0% squeeze suggests some small amount of material being squeezed during the forming process, which induces a small deviation from the ideal sine law. The result of the cases with the step-down size = 0.5mm and step-down size = 0.63mm are given in Figure 5.19 and Figure 5.20, respectively. The maximum bulge height of each of the cases is shown in Table 5.5.
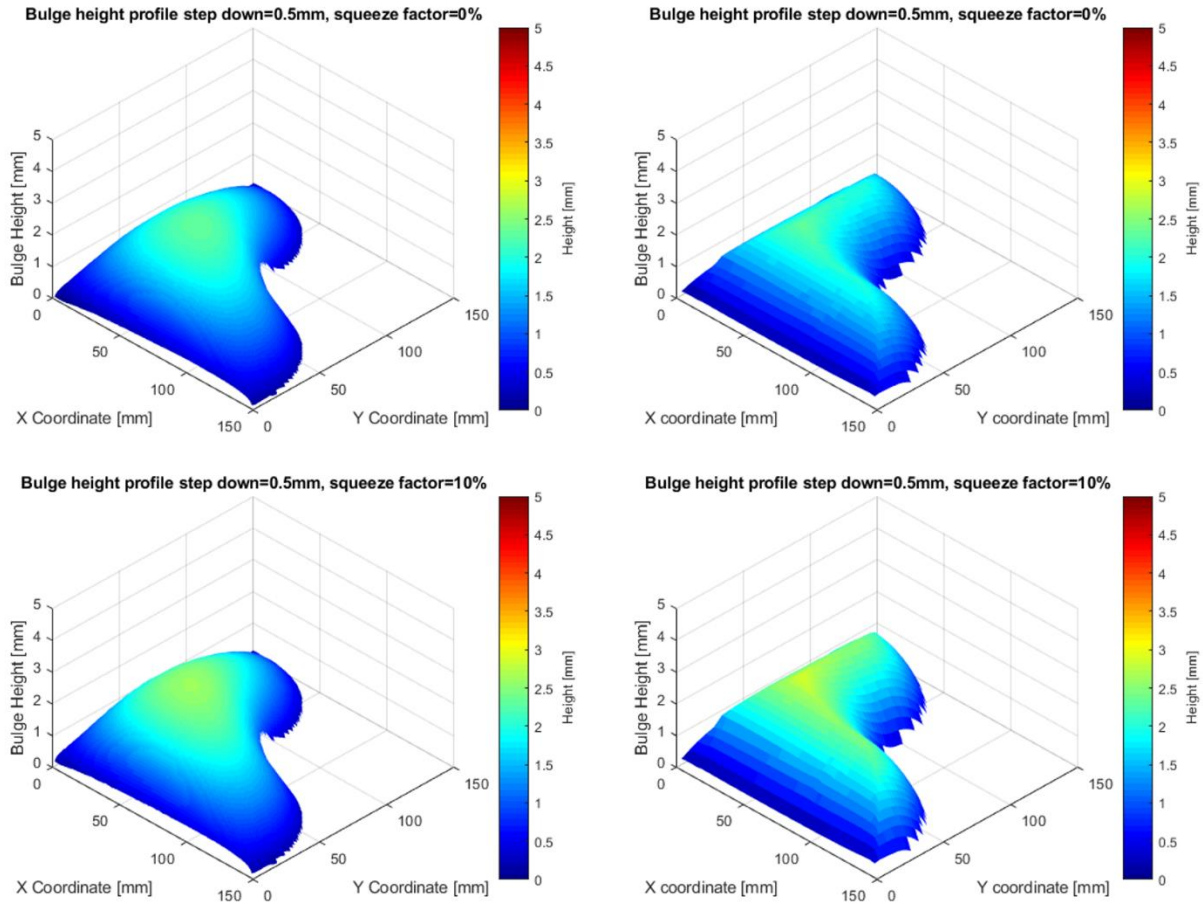
Figure 5.19 Comparison of the experimental bulge profile (left) and modeled bulge profile (right) for the step-down size = 0.5mm
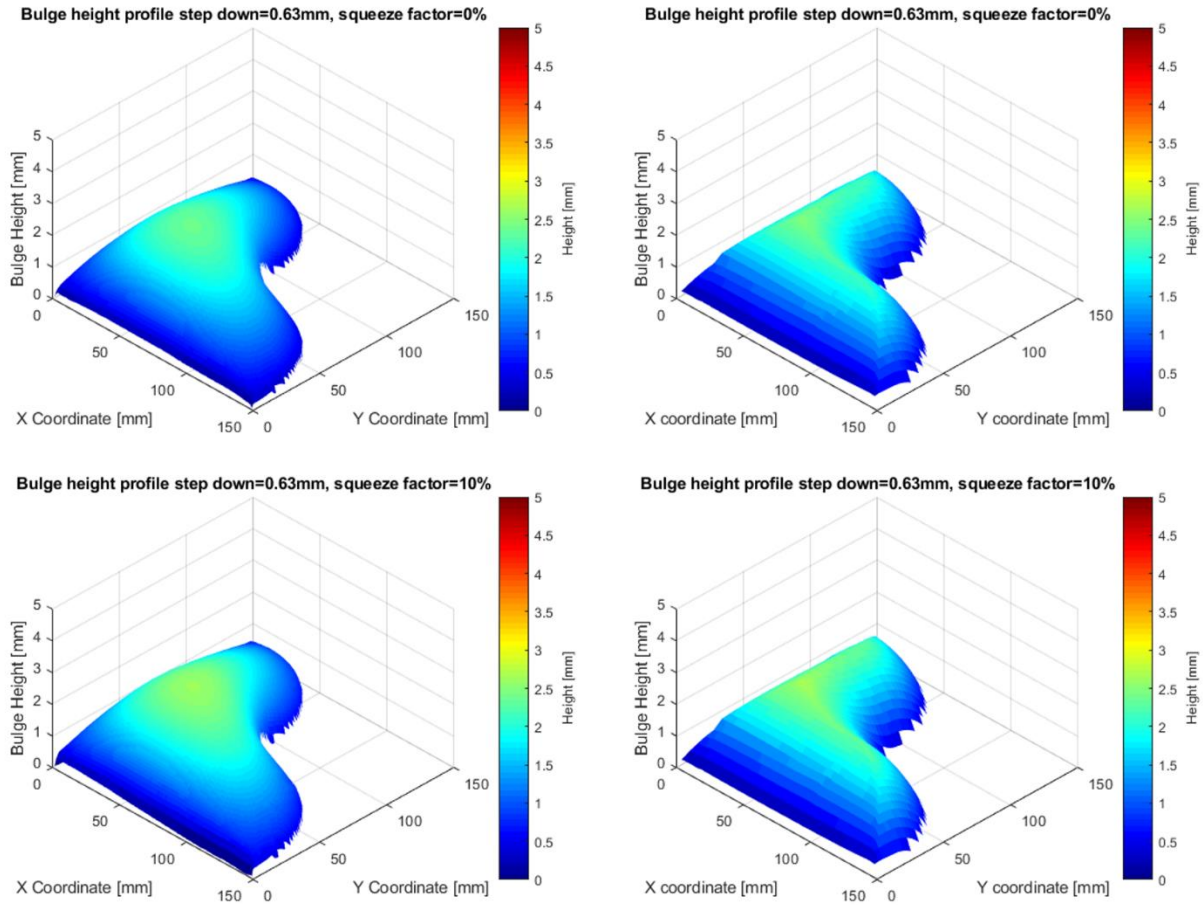
Figure 5.20 Comparison of the experimental bulge profile (left) and modeled bulge profile (right) for the step-down size= 0.63mm

It was seen that the weighted summation method was less successful in giving an accurate profile in the case of the heart compared to that of the cone. In the experiment, the profile exhibits a more centered surface towards the middle, while in the model, a plateau region develops, which is broader in area. The plateau's occurrence is due to the way the algorithm calculates the height of the bulge. The nodal points in the heart's protruding middle region are influenced by the material from both the curved surface and the flat surface. There may be a different amount of material transfer in the curved region. In this work, the current model is set to use a single material transfer value for the simplicity of the calculation. However, from comparing the maximum bulge height,

it can be seen that maximum bulge height is predicted accurately. Also, it was observed that the predicted location of the maximum bulge height matches that of the experiment. The matching result indicates that the amount of material transfer considered as the boundary condition at the maximum location matches the experimental condition. The difference in the bulge surface's overall profile may be less critical as long as the maximum bulge height is correctly predicted.

Table 5.5 Maximum bulge height comparison

	Δz= 0.5mm PSF = 0%	Δz= 0.5mm PSF = 10%	Δz= 0.63mm PSF = 0%	Δz= 0.63mm PSF = 10%
Experiment	2.3137mm	2.5856mm	2.3624mm	2.5640mm
Model	2.3018mm	2.7256mm	2.4758mm	2.6875mm
Error	0.51%	5.41%	4.80%	4.82%

5.5. 3-D prediction of part geometry for heart shape using the combined analytical model

For final validation, the method was extended to predict full 3-D heart shape. The experimental measurement is point cloud data that consists of 181560 points. The best fit surface was generated using the Matlab mesh function. The analytical model surface was created from 60 strip profiles situated around the heart shape at critical positions to provide geometry and thickness data to cover the entire part. As seen in Figure 5.21, both the heart and the bulge wall section for both experiment and model have a well-matching result.

While there may be some errors in the predicted result, the analytical model could give predictions that are close enough to provide the user indication as to whether the part may be formed within specification for a particular set of process parameters for a given geometry.
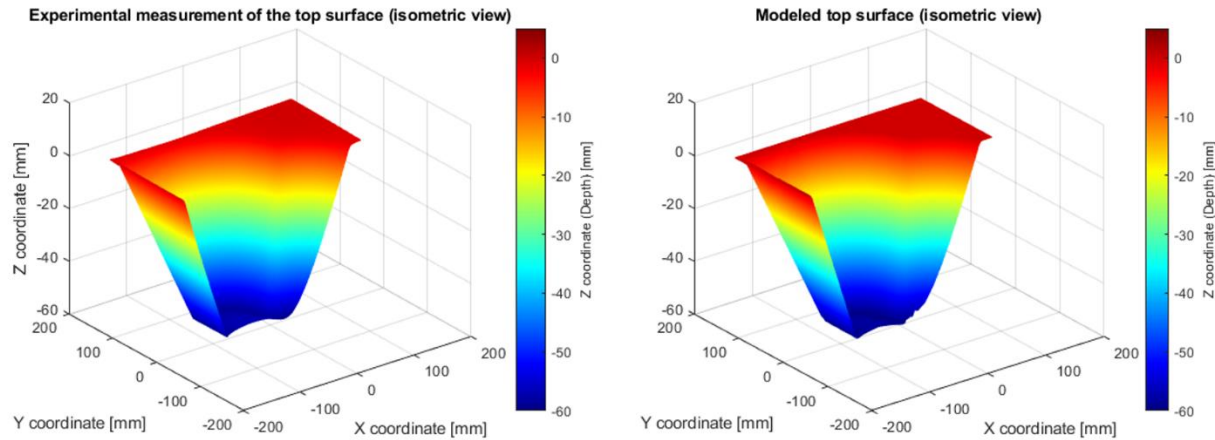
Figure 5.21 Comparison of the 3D tool side surface profile between the experiment (left) and the analytical model (right)

5.6. Summary and conclusions

Incremental forming provides the sheet metal forming technology to provide low volume production of sheet metal parts with reasonably complex geometry. The accurate model for predicting the formed part's geometry is crucial in expanding the use of incremental forming for various geometries and reducing the trial and error in determining the required process parameters. However, the complicated strain path due to the accumulation of localized deformation has proven to be an obstacle in connecting the process parameter with the geometric prediction. The conventional means of prediction, such as FEM models, have proven to yield accurate results but with high computational cost with little room for expansion in predicting large geometry. The analytical models based on sine law have provided a basic prediction of the shape but with limitations.

Two analytical models were developed, one for predicting the wall thickness and material transfer and the other for bulge prediction. The analytical model for wall thickness prediction called segmentation based analytical model is based on conducting segmentation in both lateral and longitudinal directions to create a unit volume element that incorporates one scallop profile

created by the tool's movement. In doing so, it was seen that the scalloped surface that forms during the process has a direct correlation with the step-down size, squeeze factor, tool radius, and sheet thickness. The analytical model for bulge prediction called weighted summation based analytical model is based on using the weighted summation based on predefined shape function to calculate bulge height. By expending the prediction of one scallop's surface profile to all scallops formed during forming and including the bulge prediction, the prediction can be expanded to full 3D geometry.

To demonstrate the segmentation-based analytical model's prediction capability, comparisons at three different levels were made. First, explicitly comparing the scalloped profile of the formed part measured experimentally using a profilometer. Next, using the benchmark heart shape with the proposed algorithm, the scallop profile prediction was expanded to an actual prediction of the 2D/3D geometry and thickness. The comparison of the scalloped surface profile showed that the scalloped surface predicted in the analytical model was a good match with that of the experiment. The model predicted the wavelength accurately and the amplitude with some errors resulting from the inability of the material and the CNC-tool to act perfectly. Comparing the heart shape's geometry and thickness showed a good correlation between the model and the experiment. The model provided predictions with more than 95% accurate for both thickness and geometry.

To demonstrate the capability of the weighted summation based analytical model for bulge prediction, validation was conducted for a 67° cone and a heart shape for a different combination of process parameters. The shape function was obtained by analyzing the bulge profile of the formed part. It was found that the shape function for the 0% squeeze and 2.54% squeeze had an analogous shape function where scaling by a scalar amount would result in the same shape. The

130

geometric constraints around the undeformed region seem to impact the shape function, and future work will be conducted further to prove the relation between shape function and geometric constraint.

The 3-D profile comparison of the modeled prediction and experimental measurement was well matching with minimal error for cones. The squared error analysis suggests that both predictions had less than 0.05mm difference in the bulge height. For the heart, the maximum bulge height and location were predicted accurately for all cases, while there were some differences in the predicted bulge profile. These differences may be due to the limitation that the current analytical model considers a fixed value for the amount of material transfer. However, comparing the 3-D profile of the overall part suggests that the analytical model can provide accurate predictions.

Finally, the computational cost comparison shows that the analytical model could predict the result with less than 1% of the cost required for the FEM model, which was computed using 120 cores. While the analytical model lacks understanding in various aspects such as stress and strain data that the FEM model provides, it would be suitable for providing quick prediction of geometry and thickness distribution to check the feasibility of the incremental forming for specific geometry.

Chapter 6 Summary and Future Work

6.1. Summary

The incremental forming process is investigated to understand the material behavior during forming utilizing an advanced modeling technique. Novel research has been conducted on modeling incremental forming processes to understand the influence of process parameters involved in incremental forming processes. The quantitative result provides a guideline on selecting an appropriate set of experimental process parameters with a minimum trial and error amount. The experimental process parameter selection is then translated to finite model process parameter guideline, which provides knowledge of how much errors one should expect utilizing a specific set of model parameters such as material models. The uncertainly of the experiment and model were evaluated. It was found that experimental uncertainties were much smaller than that of the model, and both experimental and model uncertainty values met the industry standard. Finally, cost-complexity-accuracy analysis was conducted to give a quantitative comparison of various numerical models.

A multiscale finite element model has been developed to understand the material behavior during incremental forming at the macro scale and the mesoscale. The model can predict defective phenomena, which can be detrimental in achieving precision in incremental forming. Three specific defective phenomena have been investigated, thinning, the bulge, and twisting. The mechanism of the defective phenomena has been identified. It was found that identified defects can detrimentally impact the formability of the material and precision of the manufacturing

process.

Based on the understanding found in multiscale models, it was observed that there is a material movement that can be calculated per rotation of the tool, contributing to the wall thickness and the formation of the bulge. The wall thickness at any region of the formed part can be analytically calculated based on the process parameters and the amount of material movement calculated. Two novel analytical models are proposed. The first model predicts the wall thickness and material movement based on the process parameters. The other predicts the bulge formation based on the calculated material movement and the shape of the undeformed region in the middle. Combining these two analytical models, it is possible to predict the full 3-D geometry of the target part.

The major findings of this dissertation can be summarized into three parts:

(1) Understanding of the influence of the process parameters based on the calibrated finite element model:

- Categorization of the process parameters to make connections between the experimental process parameters and the model process parameters.

- The development of the finite element model for simulating the incremental forming process.

- Sensitivity study of the crucial model parameters such as constitutive material model, element size selection, scaling factor, and contact/friction to understand its outcome on the accuracy of the prediction and computation cost.

- The experimental/prediction result can be categorized into three sections, the deformation in the region where the tool is in direct contact, the deformation in the region where the tool is not in direct contact, and the forming force during the forming

operation. The element size has the most impact on the thickness and geometry prediction. The material model that consists of the material yield function and material hardening law has the most impact on predicting the forming forces.

- The errors associated with using different values for the model process parameters are investigated to determine which values or which range of values should be used to achieve the optimum result.

- The range of experimental process parameter values that results in successful forming operation is given based on the experimental and modeled result. The guideline is given in generalized non-dimensional relative values to be robust.

- Uncertainty analysis for experiment and model were conducted. Also, a cost-complexity- accuracy comparison was made to provide a quantitative comparison of the model performance.

(2) Understanding of defective phenomena in the deformation region based on the established multiscale models:

- Defective phenomena of thinning, bulging, and twisting are investigated to understand their mechanism.

- The excess thinning occurring in the high wall angle results from the counteracting the radial forming force during forming, which results in a higher value of wall angle in the localized region. A higher wall angle results in a thinner wall thickness in that region. If the wall angle due to this increase exceeds the material's forming limit, a fracture can occur.

- The bulge defect in the undeformed region is due to the material movement that is created during forming. Especially in two point incremental forming where there could

be a positive squeeze factor value, the incremental material movement can occur based on the volume conservation. The access material is pushed into the undeformed region, and since more material is crammed into the region, a bulge occurs along with the compressive stress. If the bulge is excessive, a fracture can occur.

- Twisting in incremental forming is the twisting of the material during the forming operation. As the tool forms the material, shear stress develops due to the friction between the tool and the sheet. While this defect may be less important than thinning and bulge, it can lead to detrimental material property and poor esthetic look.

(3) Developing novel analytical models for prediction of formed geometry:

- The segmentation-based analytical model is proposed, which predicts the geometry in the wall region where the deformation occurs due to the direct contact with the tool. The model takes in the experimental process parameters and the target geometry as input and outputs the 3-D geometry with the micron resolution, which allows the calculation of the material movement.

- The weighted summation analytical model is proposed, which predicts the geometry of the bulge in the region where the deformation occurs from indirect contact with the tool. The model takes in the geometry of the undeformed region and input material movement at the boundaries and calculates the 3-D bulge profile.

- The combined result of the two analytical models allows predicting the full 3-D geometry of the formed part.

6.2. Future work

Finite element modeling of ISF processes is a tool to provide answers to stress-strain evolutions and predict the final geometry. However, it is insufficient to understand the

135

microstructure that develops during the process, which can provide valuable insights into the nature of the process and springback. One direction is proposed as a future work for which preliminary results are presented in the following section.

6.2.1. Prediction of the texture evolution in ISF

Utilizing the crystal plasticity finite element simulation makes it possible to bridge the mesoscale (grain level) a microscale (thickness level). The microstructure evolution provides understandings of the texture that develops during the forming. Preliminary work shows that CPFE can predict texture development for a Representative Volume Element (RVE) with the initial texture data gathered from an EBSD scan of rolled AA 7075-O sheet and velocity gradient of the element calculated from a continuum ISF FEM model.

6.2.2. Data-driven prediction of the microstructure evolution in ISF

The simulation of temporal texture evolution is computationally expensive and impossible to iterate for different process parameters. A data-driven computational approach for faster and tunable texture predictions, which involve FEM, the crystal plasticity model, and machine learning (ML), can solve this problem. First, the CPFE model simulating a deformation process of ISF is used to predict texture development throughout the forming process. A data mining method is then used to transform raw data to an appropriate form for the machine learning model input. The multivariate time series ML model to predict the texture evolution based on the input deformation gradient. The ML model can increase predictability in orders of magnitude faster than the conventional method, which allows experimentalists to quickly identify the tunable parameters that correspond to their desirable microstructure.

Bibliography

[1]   Giardini, C., Ceretti, E., & Attanasio, A. (2005). Innovative Sheet Forming Processes: Evaluation of the Economic Convenience of an Actual Case. In *AMST'05 Advanced Manufacturing Systems and Technology* (pp. 473-482). Springer, Vienna.

[2]   Ambrogio G, Di Lorenzo R, Micari F (2003) Analysis of the economical effectiveness of incremental forming processes: an industrial case study. Proceedings VI AITeM Conference, Gaeta, Italy

[3]   Allwood, J. M., King, G. P. F., & Duflou, J. (2005). A structured search for applications of the incremental sheet-forming process by product segmentation. *Proceedings of the Institution of Mechanical Engineers, Part B: Journal of Engineering Manufacture*, *219*(2), 239-244.

[4]   Jeswiet, J., Micari, F., Hirt, G., Bramley, A., Duflou, J., & Allwood, J. (2005). Asymmetric single point incremental forming of sheet metal. *CIRP annals*, *54*(2), 88-114.

[5]   Eyckens, P., He, S., Van Bael, A., Van Houtte, P., & Duflou, J. (2007, May). Forming limit predictions for the serrated strain paths in single point incremental sheet forming. In *AIP Conference Proceedings* (Vol. 908, No. 1, pp. 141-146). American Institute of Physics.

[6]   Flores, P., Duchene, L., Bouffioux, C., Lelotte, T., Henrard, C., Pernin, N., ... & Habraken, A. M. (2007). Model identification and FE simulations: effect of different yield loci and hardening laws in sheet forming. *International journal of plasticity*, *23*(3), 420-449.

[7]   Shim, M. S., & Park, J. J. (2001). The formability of aluminum sheet in incremental forming. *Journal of Materials Processing Technology*, *113*(1-3), 654-658.

[8]   Filice, L., Fratini, L., & Micari, F. (2002). Analysis of material formability in incremental forming. *CIRP Annals*, *51*(1), 199-202.

[9]   Fratini, L., Ambrogio, G., Di Lorenzo, R., Filice, L., & Micari, F. (2004). Influence of mechanical properties of the sheet material on formability in single point incremental forming. *CIRP Annals*, *53*(1), 207-210.

[10]   Emmens, W. C., & van den Boogaard, A. H. (2009). An overview of stabilizing deformation mechanisms in incremental sheet forming. *Journal of Materials Processing Technology*, *209*(8), 3688-3695.

[11]   Young, D., & Jeswiet, J. (2004). Wall thickness variations in single-point incremental forming. *Proceedings of the Institution of Mechanical Engineers, Part B: Journal of Engineering Manufacture*, *218*(11), 1453-1459.

[12]   Salem, E., Shin, J., Nath, M., Banu, M., & Taub, A. I. (2016). Investigation of thickness variation in single point incremental forming. *Procedia Manufacturing*, *5*, 828-837.

[13]   Hussain, G., & Gao, L. (2007). A novel method to test the thinning limits of sheet metals in negative incremental forming. *International Journal of Machine Tools and Manufacture*, *47*(3-4), 419-435.

[14] Hussain, G., Gao, L., Hayat, N., & Ziran, X. (2009). A new formability indicator in single point incremental forming. *Journal of Materials Processing Technology*, *209*(9), 4237-4242.

[15] Jackson, K., & Allwood, J. (2009). The mechanics of incremental sheet forming. *Journal of materials processing technology*, *209*(3), 1158-1174.

[16] Allwood, J. M., Shouler, D. R., & Tekkaya, A. E. (2007). The increased forming limits of incremental sheet forming processes. In *Key Engineering Materials* (Vol. 344, pp. 621-628). Trans Tech Publications.

[17] Bambach, M., Hirt, G., & Junk, S. (2003, April). Modelling and experimental evaluation of the incremental CNC sheet metal forming process. In *7th international conference on computational plasticity, Barcelona, Spain.*

[18] Huang, Y., Cao, J., Smith, K. S., Woody, B., Ziegert, J., & Li, M. (2008, October). Experimental and numerical investigation of forming limits in incremental forming of a conical cup. In *Transactions of the North American Manufacturing Research Institution of SME* (pp. 389-396).

[19] Silva, M. B., Skjødt, M., Martins, P. A., & Bay, N. (2008). Revisiting the fundamentals of single point incremental forming by means of membrane analysis. *International Journal of Machine Tools and Manufacture*, *48*(1), 73-83.

[20] Benedyk, J. C., Parikh, N. M., & Stawarz, D. (1971). A method for increasing elongation values for ferrous and nonferrous sheet metals(Ferrous and nonferrous sheet metals neck formation prevention for increasing elongation in tensile tests, using continuous plastic bending method). *Journal of Materials*, *6*, 16-29.

[21] Emmens, W. C., & van den Boogaard, A. H. (2008, June). Extended tensile testing with simultaneous bending. In *IDDRG 2008 International Conference, Olofström, Sweden.*

[22] Centeno, G., Bagudanch, I., Martínez-Donaire, A. J., Garcia-Romeu, M. L., & Vallellano, C. (2014). Critical analysis of necking and fracture limit strains and forming forces in single-point incremental forming. *Materials & Design*, *63*, 20-29.

[23] Sawada, T., Fukuhara, G., & Sakamoto, M. (2001). Deformation mechanism of sheet metal in stretch forming with computer numerical control machine tools. *JOURNAL-JAPAN SOCIETY FOR TECHNOLOGY OF PLASTICITY*, *42*(10; ISSU 489), 1067-1069.

[24] Maqbool, F., & Bambach, M. (2017). Revealing the Dominant Forming Mechanism of Single Point Incremental Forming (SPIF) by Splitting Plastic Energy Dissipation. *Procedia Engineering*, *183*, 188-193.

[25] Silva, M. B., Nielsen, P. S., Bay, N., & Martins, P. A. F. (2011). Failure mechanisms in single-point incremental forming of metals. *The International Journal of Advanced Manufacturing Technology*, *56*(9-12), 893-903.

[26] Seong, D. Y., Haque, M. Z., Kim, J. B., Stoughton, T. B., & Yoon, J. W. (2014). Suppression of necking in incremental sheet forming. *International Journal of Solids and Structures*, *51*(15-16), 2840-2849.

[27] Malhotra, R., Xue, L., Belytschko, T., & Cao, J. (2012). Mechanics of fracture in single point incremental forming. *Journal of Materials Processing Technology*, *212*(7), 1573-1590.

[28] Avitzur, B., & Yang, C. T. (1960). Analysis of power spinning of cones. *Journal of Engineering for Industry*, *82*(3), 231-244.

[29] Kalpakcioglu, S. (1961). A study of shear-spinnability of metals. *Journal of Engineering for Industry*, *83*(4), 478-483.

[30]   Bambach, M. (2010). A geometrical model of the kinematics of incremental sheet forming for the prediction of membrane strains and sheet thickness. *Journal of Materials Processing Technology*, *210*(12), 1562-1573.

[31]   Kim, T. J., & Yang, D. Y. (2000). Improvement of formability for the incremental sheet metal forming process. *International Journal of Mechanical Sciences*, *42*(7), 1271-1286.

[32]   He, S., Gu, J., Sol, H., Van Bael, A., Van Houtte, P., Tunckol, Y., & Duflou, J. R. (2007). Determination of strain in incremental sheet forming process. In *Key Engineering Materials* (Vol. 344, pp. 503-510). Trans Tech Publications.

[33]   Fang, Y., Lu, B., Chen, J., Xu, D. K., & Ou, H. (2014). Analytical and experimental investigations on deformation mechanism and fracture behavior in single point incremental forming. *Journal of Materials Processing Technology*, *214*(8), 1503-1515.

[34]   Chang, Z., Li, M., & Chen, J. (2019). Analytical modeling and experimental validation of the forming force in several typical incremental sheet forming processes. *International Journal of Machine Tools and Manufacture*, *140*, 62-76.

[35]   Ai, S., Lu, B., Chen, J., Long, H., & Ou, H. (2017). Evaluation of deformation stability and fracture mechanism in incremental sheet forming. *International Journal of Mechanical Sciences*, *124*, 174-184.

[36]   Li, Y., Daniel, W. J., & Meehan, P. A. (2017). Deformation analysis in single-point incremental forming through finite element simulation. *The International Journal of Advanced Manufacturing Technology*, *88*(1-4), 255-267.

[37]   Robert, C., Dal Santo, P., Delamézière, A., Potiron, A., & Batoz, J. L. (2008). On some computational aspects for incremental sheet metal forming simulations. *International Journal of Material Forming*, *1*(1), 1195-1198.

[38]   Henrard, C., Bouffioux, C., Eyckens, P., Sol, H., Duflou, J. R., Van Houtte, P., ... & Habraken, A. M. (2011). Forming forces in single point incremental forming: prediction by finite element simulations, validation and sensitivity. *Computational mechanics*, *47*(5), 573-590.

[39]   Eyckens, P., Belkassem, B., Henrard, C., Gu, J., Sol, H., Habraken, A. M., ... & Van Houtte, P. (2011). Strain evolution in the single point incremental forming process: digital image correlation measurement and finite element prediction. *International journal of material forming*, *4*(1), 55-71.

[40]   Bambach, M., & Hirt, G. (2005). Performance assessment of element formulations and constitutive laws for the simulation of incremental sheet forming (ISF). In *VIII International Conference on Computational Plasticity*.

[41]   Yue, Z. M., Chu, X. R., & Gao, J. (2017). Numerical simulation of incremental sheet forming with considering yield surface distortion. *The International Journal of Advanced Manufacturing Technology*, *92*(5-8), 1761-1768.

[42]   Esmaeilpour, R., Kim, H., Park, T., Pourboghrat, F., & Mohammed, B. (2017). Comparison of 3D yield functions for finite element simulation of single point incremental forming (SPIF) of aluminum 7075. *International Journal of Mechanical Sciences*, *133*, 544-554.

[43]   Leem, D., Moser, N., Ren, H., Mozaffar, M., Ehmann, K. F., & Cao, J. (2019). Improving the accuracy of double-sided incremental forming simulations by considering kinematic hardening and machine compliance. *Procedia Manufacturing*, *29*, 88-95.

[44]   Esmaeilpour, R., Kim, H., Park, T., Pourboghrat, F., Xu, Z., Mohammed, B., & Abu-Farha, F. (2018). Calibration of Barlat Yld2004-18P yield function using CPFEM and 3D RVE

for the simulation of single point incremental forming (SPIF) of 7075-O aluminum sheet. *International Journal of Mechanical Sciences*, *145*, 24-41.

[45] De Sena, J. I. V., Guzmán, C. F., Duchêne, L., Habraken, A. M., Behera, A. K., Duflou, J., ... & de Sousa, R. A. (2016). Simulation of a two-slope pyramid made by SPIF using an adaptive remeshing method with solid-shell finite element. *International Journal of Material Forming*, *9*(3), 383-394.

[46] Bouffioux, C., Lequesne, C., Vanhove, H., Duflou, J. R., Pouteau, P., Duchêne, L., & Habraken, A. M. (2011). Experimental and numerical study of an AlMgSc sheet formed by an incremental process. *Journal of Materials Processing Technology*, *211*(11), 1684-1693.

[47] Eyckens, P., Belkassem, B., Henrard, C., Gu, J., Sol, H., Habraken, A. M., ... & Van Houtte, P. (2011). Strain evolution in the single point incremental forming process: digital image correlation measurement and finite element prediction. *International journal of material forming*, *4*(1), 55-71.

[48] Malhotra, R., Huang, Y., Xue, L., Cao, J., & Belytschko, T. (2010, June). An investigation on the accuracy of numerical simulations for single point incremental forming with continuum elements. In *AIP Conference Proceedings* (Vol. 1252, No. 1, pp. 221-227). AIP.

[49] Hirt, G., Ames, J., Bambach, M., & Kopp, R. (2004). Forming strategies and process modelling for CNC incremental sheet forming. *CIRP Annals*, *53*(1), 203-206.

[50] Li, Y., Liu, Z., Daniel, W. J. T., & Meehan, P. A. (2014). Simulation and experimental observations of effect of different contact interfaces on the incremental sheet forming process. *Materials and Manufacturing Processes*, *29*(2), 121-128.

[51] Ayed, L. B., Robert, C., Delamézière, A., Nouari, M., & Batoz, J. L. (2014). Simplified numerical approach for incremental sheet metal forming process. *Engineering Structures*, *62*, 75-86.

[52] Duchêne, L., Guzmán, C. F., Behera, A. K., Duflou, J. R., & Habraken, A. M. (2013). Numerical simulation of a pyramid steel sheet formed by single point incremental forming using solid-shell finite elements. In *Key Engineering Materials* (Vol. 549, pp. 180-188). Trans Tech Publications.

[53] Boyer H (1987) Atlas of Stress-Strain Curves, ASM International, Metals Park, Ohio

[54] Abaqus 6.14 manual/18.2.2 Models for metals subjected to cyclic loading

[55] Abaqus 6.14 manual/8.2.6 Anisotropic yield/creep

[56] ASM International (1990). Properties of Wrought Aluminum and Aluminum Alloys, Properties and Selection: Nonferrous Alloys and SpecialPurpose Materials, Vol 2, ASM International, 62–122

[57] Eyckens, P., Duflou, J., Van Bael, A., & Van Houtte, P. (2010). The significance of friction in the single point incremental forming process. *International Journal of Material Forming*, *3*(1), 947-950.

[58] Ambrogio, G., Filice, L., De Napoli, L., & Muzzupappa, M. (2005). A simple approach for reducing profile diverting in a single point incremental forming process. *Proceedings of the Institution of Mechanical Engineers, Part B: Journal of Engineering Manufacture*, *219*(11), 823-830.

[59] Ambrogio, G., Cozza, V., Filice, L., & Micari, F. (2007). An analytical model for improving precision in single point incremental forming. *Journal of Materials Processing Technology*, *191*(1-3), 92-95.

[60] Hussain, G., Gao, L., & Hayat, N. (2011). Forming parameters and forming defects in incremental forming of an aluminum sheet: correlation, empirical modeling, and optimization: part A. *Materials and Manufacturing Processes*, *26*(12), 1546-1553.

[61] Hussain, G., Al-Ghamdi, K. A., Khalatbari, H., Iqbal, A., & Hashemipour, M. (2014). Forming parameters and forming defects in incremental forming process: Part B. *Materials and Manufacturing Processes*, *29*(4), 454-460.

[62] Al-Ghamdi, K. A., & Hussain, G. (2015). The pillowing tendency of materials in single-point incremental forming: experimental and finite element analyses. *Proceedings of the Institution of Mechanical Engineers, Part B: Journal of Engineering Manufacture*, *229*(5), 744-753.

[63] Isidore, B. L., Hussain, G., Shamchi, S. P., & Khan, W. A. (2016). Prediction and control of pillow defect in single point incremental forming using numerical simulations. *Journal of Mechanical Science and Technology*, *30*(5), 2151-2161.

[64] Mohammadi, A., Vanhove, H., Van Bael, A., & Duflou, J. R. (2016). Towards accuracy improvement in single point incremental forming of shallow parts formed under laser assisted conditions. *International Journal of Material Forming*, *9*(3), 339-351.

[65] Nath, M., Salem, E., Shin, J., Odykirk, T., Banu, M., & Taub, A. (2017). Microstructure and surface finish evolution during single point incremental forming. Paper presented at the *Materials Science and Technology Conference and Exhibition 2017, MS and T 2017, , 1* 177-184. doi:10.7449/2017/MST_2017_177_184

[66] Matsubara, S. (2001). A computer numerically controlled dieless incremental forming of a sheet metal. *Proceedings of the Institution of Mechanical Engineers, Part B: Journal of Engineering Manufacture*, 215(7), pp.959-966.

[67] Neto, D., Martins, J., Oliveira, M., Menezes, L. and Alves, J. (2015). Evaluation of strain and stress states in the single point incremental forming process. *The International Journal of Advanced Manufacturing Technology*, 85(1-4), pp.521-534.

[68] Duflou J, Vanhove H, Verbert J, Gu J, Vasilakos I, Eyckens P (2010) Twist revisited: Twist phenomena in single point incremental forming. *CIRP Annals* 59(1) 307-310.

[69] Asghar, J., Shibin, E., Bhattacharya, A. and Reddy, N. (2012). Twist in Single Point Incremental Forming. *ASME 2012 International Manufacturing Science and Engineering Conference*

[70] Al-Attaby, Q., Abaas, T. and Bedan, A. (2013). The Effect of Tool Path Strategy on Twist Behavior In Single Point Incremental Sheet Metal Forming. *Journal of Engineering*, 19(4).

[71] Suresh, K., Khan, A. and Regalla, S. (2013). Tool Path Definition for Numerical Simulation of Single Point Incremental Forming. *Procedia Engineering*, 64, pp.536-545.

[72] Liu, Z., Li, Y. and Meehan, P. (2014). Tool path strategies and deformation analysis in multi-pass incremental sheet forming process. *The International Journal of Advanced Manufacturing Technology*, 75(1-4), pp.395-409.

[73] He, S., Van Bael, A., Van Houtte, P., Duflou, J. R., Szekeres, A., Henrard, C., & Habraken, A. M. (2005). Finite element modeling of incremental forming of aluminum sheets. In *Advanced Materials Research* (Vol. 6, pp. 525-532). Trans Tech Publications Ltd.

[74] Minutolo, F. C., Durante, M., Formisano, A., & Langella, A. (2007). Evaluation of the maximum slope angle of simple geometries carried out by incremental forming process. *Journal of Materials Processing Technology*, *194*(1-3), 145-150.

[75] Skjødt, M., Bay, N., Endelt, B., & Ingarao, G. (2008). Multi stage strategies for single point incremental forming of a cup. *International Journal of Material Forming*, *1*(1), 1199-1202.

[76]   Barlat, F., Brem, J. C., Yoon, J. W., Chung, K., Dick, R. E., Lege, D. J., ... & Chu, E. (2003). Plane stress yield function for aluminum alloy sheets—part 1: theory. *International Journal of Plasticity*, *19*(9), 1297-1319.

[77]   Bambach, M., Araghi, B. T., & Hirt, G. (2009). Strategies to improve the geometric accuracy in asymmetric single point incremental forming. *Production Engineering*, *3*(2), 145-156.

[78]   Shin, J., Bansal, A., Nath, M., Cheng, R., Banu, M., Taub, A., & Martinek, B. (2018, July). Prediction of Negative Bulge in Two Point Incremental Forming of an Asymmetric Shape Part. In *Journal of Physics: Conference Series* (Vol. 1063, No. 1, p. 012057).

[79]   Mozaffar, M., Bostanabad, R., Chen, W., Ehmann, K., Cao, J., & Bessa, M. A. (2019). Deep learning predicts path-dependent plasticity. *Proceedings of the National Academy of Sciences*, *116*(52), 26414-26420.

[80]   Moser, N. Ph.D. Thesis, Deformation Mechanisms and Process Planning in Double-Sided Incremental Forming

[81]   Bhattacharya, A., Maneesh, K., Venkata Reddy, N., & Cao, J. (2011). Formability and surface finish studies in single point incremental forming. *Journal of manufacturing science and engineering*, *133*(6).

[82]   Duflou, J. R., Habraken, A. M., Cao, J., Malhotra, R., Bambach, M., Adams, D., ... & Jeswiet, J. (2018). Single point incremental forming: state-of-the-art and prospects. *International Journal of Material Forming*, *11*(6), 743-773.

[83]   Al-Ghamdi, K. A., & Hussain, G. (2015). Threshold tool-radius condition maximizing the formability in SPIF considering a variety of materials: experimental and FE investigations. *International Journal of Machine Tools and Manufacture*, *88*, 82-94.

[84]   Gatea, S., Ou, H., & McCartney, G. (2016). Review on the influence of process parameters in incremental sheet forming. *The International Journal of Advanced Manufacturing Technology*, *87*(1-4), 479-499.

[85]   Hagen, E., & Jeswiet, J., 2004. Analysis of surface roughness for parts formed by CNC incremental forming. *Proc. Inst. Mech. Eng., Part B*, *219*(B), 1-6.